Technical Physics Letters, Vol. 27, No. 5, 2001, pp. 351–353. Translated from Pis'ma v Zhurnal Tekhnicheskoĭ Fiziki, Vol. 27, No. 9, 2001, pp. 1–7.

A Mass-Spectrometric Study of the Behavior of Thermotropic Liquid-Crystalline Polymers on Heating

O. F. Pozdnyakov, B. P. Redkov, and E. A. Egorov

Ioffe Physicotechnical Institute, Russian Academy of Sciences, St. Petersburg, 194021 Russia

e-mail: ao.pozd@pop.ioffe.rssi.ru

Received October 31, 2000

Abstract—Physicochemical processes accompanying the thermal treatment of a liquid-crystalline aromatic copolyester Ultrax-4002 at temperatures in the vicinity of the thermotropic transition were studied by mass spectrometry in order to reveal possible features of the mechanism of polymer strengthening. It is shown that the thermal treatment leads to additional polycondensation in the material and the degradation of macromolecules with the accumulation of low-molecular-mass products in the polymer bulk. The energy parameters of the polycondensation, thermal degradation, and diffusion processes were determined. © *2001 MAIK "Nauka/Interperiodica".*

The unique combination of the thermal and mechanical properties of thermotropic liquid-crystalline (LC) polymers naturally attracts the attention of researchers. A high thermal stability of these LC polymers, together with good mechanical strength, makes these materials highly promising for various applications [1–5]. A unique feature of the LC polymers is a considerable (severalfold) increase in the tensile strength and elastic modulus upon a thermal treatment involving a long-time heating at temperatures close to the thermotropic transition temperature T_{tt}. However, the reasons for this strengthening are still not completely clear.

Some researchers believe that not only large-scale structural transformations but certain chemical changes in the polymer structure as well may account for a spontaneous increase in the mechanical properties observed upon the thermal treatment [5]. It should be emphasized that the thermal treatment is a necessary stage of the technological process imparting required properties to the LC material (fiber or film). The temperature interval employed for the thermal treatment of LC copolyesters extends up to 350–400°C. These temperatures are sufficiently high to feature intense diffusion and degradation processes in these polymers.

In order to obtain objective information about the chemical processes occurring in LC copolyesters treated in the vicinity of T_{tt}, we studied these materials by mass-spectrometric thermal analysis (MTA). Using MTA, it is possible to determine the detailed composition of the products liberated from the samples simultaneously with measuring the kinetics of the product formation in the course of a thermal treatment. The MTA was effected using a modified mass spectrometer of the MX-1320 type [6].

The experiments were performed on the fully aromatic random copolyester Ultrax-4002 (BASF, Germany). The molar fractions of the fragments of tere- and isophtalic acids and *p*,*p*-dioxybisphenol in macromolecules of this polymer [4] are 0.25, 0.25, and 0.5, respectively. The chemical formula of the polymer chain unit is as follows:

$$\underset{}{-}(CO\text{–}Ph\text{–}CO)_{0.25\ \text{tere-}}\text{–}(CO\text{–}Ph\text{–}CO)_{0.25\ \text{iso-}}\text{–}(O\text{–}Ph\text{–}Ph\text{–}O)_{0.5}\text{–}$$

where Ph is the phenyl group (C_6H_4).

The Ultrax-4002 samples were studied in the form of granules and oriented fibers. In order to minimize the effect of diffusion upon the gas evolution process, we also studied ultrathin (submicrogram) samples obtained by rubbing granules on the surface of a heated metal support provided with a thermocouple. Preliminary calibration measurements showed that a ~5-mm-long trace transferred about 0.04 μg of the polymer from the granule onto the substrate surface. A total of 60 nonoverlapping traces were sufficient to prepare an ultrathin sample. For MTA, the samples were placed into a vacuum chamber of the mass spectrometer and heated at a rate of 7 K/s.

The mass-spectrometric analysis of volatile products liberated from polymer granules during the first heating showed these substances to represent a mixture, the main components being (in the order of decreasing proportion) CO_2, CO, phenol, acetic acid, and molecules such as phenyl benzoate and/or dibenzoyl. The latter molecules represent large fragments of the polymer chain. During the repeated heating, the most significant qualitative change was observed for acetic acid, which ceased to evolve.

Attempts at measuring the temperature dependence of the kinetics of liberation of the volatile products of thermal degradation from a massive sample representing a part (~10 mg) of the polymer granule showed that

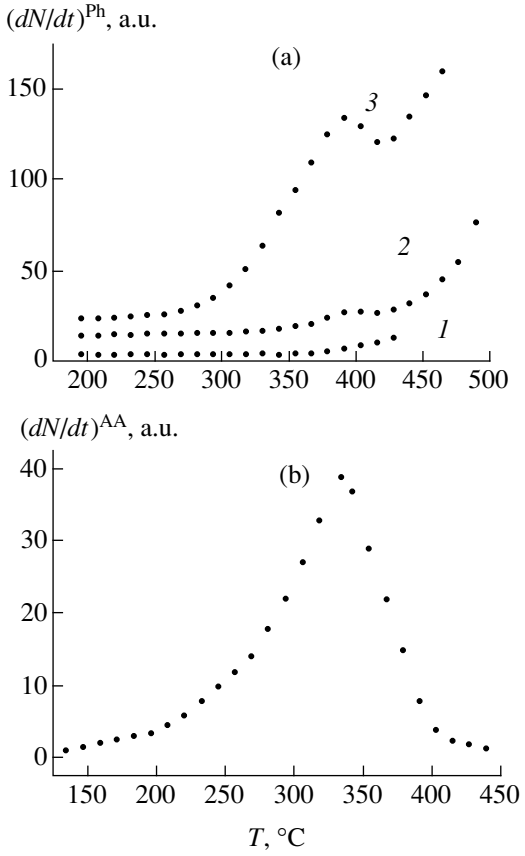

Fig. 1. Typical plots of the evolution rate of (a) phenol $(dN/dt)^{Ph}$ and (b) acetic acid $(dN/dt)^{AA}$ versus temperature measured during the thermal treatment of Ultrax-4002 copolyester. The evolution of phenol was measured during three sequential heating cycles *1–3* with intermediate cooling of the sample to room temperature; the formation of acetic acid was studied during the first heating of the sample.

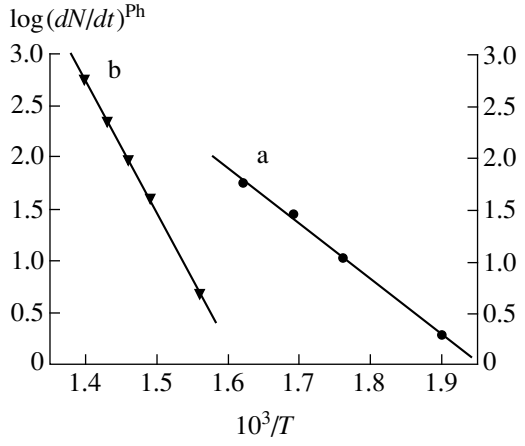

Fig. 2. The Arrhenius plots illustrating determination of the activation energies for (a) the phenol diffusion in a massive sample of Ultrax-4002 (E_{dif}^{Ph} = 97 kJ/mol) and (b) the thermal degradation of the polymer measured by the phenol evolution from submicrogram samples (E_{TD}^{Ph} = 240 kJ/mol). See the text for explanations.

the degradation products are accumulated in the sample volume upon cooling. Figure 1a shows typical plots of the phenol evolution rate versus temperature measured during three sequential heating cycles. As seen, the onset temperature of Ph evolution during the first heating is ~350°C, while during the second and third heating this product is observed at ~250°C. Judging by curve *2*, the amount of phenol accumulated in the sample upon the first heating is rather small (the sample was heated only to ~425°C). In curve *3*, the accumulation effect is much more pronounced because the second heating was continued up to 480°C.

The kinetics of the accumulated phenol evolution corresponds to the first-order reaction, since the reaction rate is directly proportional to the concentration. We have determined the activation energy E_{dif}^{Ph} for the Ph diffusion in copolyester Ultrax-4002 in the 240–340°C temperature range using curve *3* in Fig. 1a. The corresponding Arrhenius plot (Fig. 2a) gives $E_{dif}^{Ph} = 97 \pm 5$ kJ/mol, which qualitatively agrees with the usual level of the diffusion activation energies E_{dif} reported for diffusants of this type in crystalline polymers [7].

Subsequent measurements were conducted using submicrogram samples, where the degradation product accumulation effect was not observed and the diffusion activation energy significantly increased to reflect the chemical kinetics of the thermal degradation process. Here, the E_{TD}^{Ph} value determined from the temperature variation of the phenol evolution rate $(dN/dt)^{Ph}$ was 240 ± 10 kJ/mol for T_0 = 350°C and T_{max} = 470°C (Fig. 2b).

It is interesting to compare the latter value to the activation energy for mechanical fracture (220 kJ/mol) of the heat-treated fibers of an aromatic copolyester [2] with the composition close to that studied in our experiments. Note a good agreement between the activation energies for thermal degradation and the mechanical fracture of the LC polymers, which is evidence that we deal with the rupture of similar chemical bonds determining the process kinetics in the polymer chain in both cases.

Figure 1b shows the kinetics of acetic acid (AA) evolution during the first heating of the copolyester studied. This kinetic curve shows the following characteristic features: a significant increase in the $(dN/dt)^{AA}$ value begins at a temperature of about 230°C, the maximum evolution rate is observed at 320°C, and the activation energy for the AA formation is 36 kJ/mol (close to a value typical of the nonequilibrium polycondensation kinetics [8]). Note that, according to the NMR data, it is this temperature interval (250–300°C) where polymers of the Ultrax type exhibit a transition from "solid state" to anisotropic LC melt [9].

As is known, the polycondensation of diatomic phenol diesters (primarily diacetates) with dicarboxylic acids is usually conducted on heating to 300°C in the

melt or in the solid state, whereby the AA evolution taking place beginning with 210°C [10]. A comparison of these data to our results suggests that, with a high probability, the polycondensation process in Ultrax-4002 is incomplete. Therefore, the thermal treatment may be accompanied by an additional polycondensation of the material. Evidence for this conclusion is provided by the results of quantitative MTA. In particular, we determined the ratio of the amounts of phenol and AA liberated from massive and submicrogram samples to obtain approximately the same ratio $m_{Ph}/m_{AA} \sim 50$ in both cases. This result indicates that AA is absent in the initial polymer and appears during the additional polycondensation reaction. If AA were present as an impurity in the initial material, the long-time preliminary thermal treatment of submicrogram samples (with a thickness of ~10 nm) in vacuum would lead to a significant decrease in the AA fraction and an increase in the m_{Ph}/m_{AA} ratio above 50, which was not observed in the experiment.

Thus, the elevated temperatures used for the thermal treatment of our Ultrax-4002 samples account for the activation of some chemical processes on the background of increasing cooperative mobility of macromolecules. The additional polycondensation, leading to an increase in the length of macromolecules, can be considered as one of the main factors responsible for the improved mechanical properties of the polymer studied. Indeed, an increase in the oriented chain length leads to a decrease in the probability of slip during extension and to a redistribution of the applied load between strongest chemical bonds.

Another important factor is that the additional polycondensation induced by the thermal treatment takes place in an oriented melt rather than in the isotropic melt, and the elongated chains are more readily packed so as to form an ordered supermolecular structure. The process of thermal degradation accompanying the polycondensation reaction negatively affects the mechanical properties. Provided that the MTA conditions are properly selected, mass spectrometry can be used for the quantitative monitoring of chemical processes in materials of the Ultrax-4002 type.

Acknowledgments. This study was supported by the Russian Foundation for Basic Research, project nos. 00-03-33065.

REFERENCES

1. K.-U. Bühler, *Spezialplaste* (Akademie-Verlag, Berlin, 1978; Khimiya, Moscow, 1984).
2. A. V. Savitskii, A. Yu. Bilibin, and I. A. Gorshkova, Polym. Sci. **34** (8), 722 (1992).
3. W. Brostow, M. Hess, and B. L. Lopez, Macromolecules **27** (8), 2262 (1994).
4. E. M. Antipov, I. A. Volegova, Yu. K. Godovskiĭ, *et al.*, Vysokomol. Soedin., Ser. A **39** (11), 1791 (1997).
5. *Liquid-Crystal Polymers*, Ed. by N. A. Platé (Khimiya, Moscow, 1988; Plenum, New York, 1993).
6. O. F. Pozdnyakov, V. R. Regel', B. P. Redkov, and V. V. Shalimov, Vysokomol. Soedin., Ser. A **20** (11), 2494 (1978).
7. A. E. Chalykh, *Diffusion in Polymer Systems* (Khimiya, Moscow, 1987).
8. *Encyclopedia of Polymers* (Sovetskaya Éntsiklopediya, Moscow, 1974), Vol. 2, p. 862.
9. E. A. Egorov, V. V. Zhizhenkov, A. V. Savitskiĭ, and I. A. Gorshkova, in *Proceedings of the International Conference "Chemical Fibers-2000," Tver', 2000*, pp. 21–27.
10. K.-U. Bühler, *Spezialplaste* (Akademie-Verlag, Berlin, 1978; Khimiya, Moscow, 1984).

Translated by P. Pozdeev

Technical Physics Letters, Vol. 27, No. 5, 2001, pp. 354–355. Translated from Pis'ma v Zhurnal Tekhnicheskoĭ Fiziki, Vol. 27, No. 9, 2001, pp. 8–12.

Excited Nitrogen Molecule Formation in a DC-Glow-Discharge-Pumped Excimer Lamp

A. K. Shuaibov, L. L. Shimon, A. I. Dashchenko, and I. V. Shevera

Uzhgorod National University, Uzhgorod, Ukraine

e-mail: ishev@univ.uzhgorod.ua

Received November 17, 2000

Abstract—The plasma in an excimer lamp operating in the λ = 258 nm [Cl_2(D'–A')] and 175 nm [ArCl(B–X)] modes using an Ar–Cl_2 gas mixture excited with a longitudinal dc glow discharge was studied by the method of spectroscopic diagnostics. In the presence of small air admixtures ($P \le 30$ Pa) in the working medium, the plasma exhibits the formation of excited nitrogen molecules decaying with the emission of molecular bands in the 193–271 nm wavelength range. The emission intensities of both molecular and excimer bands were measured and the conditions were determined under which the excited nitrogen molecules most significantly affect the optical characteristics of the discharge. *© 2001 MAIK "Nauka/Interperiodica".*

Using the excimer lamps filled with krypton and xenon chlorides (λ = 222, 308 nm) pumped by dc glow discharge, it is possible to obtain an output radiation power of 10–20 W [1, 2]. A promising way to create radiation sources filled with a cheaper working medium and emitting shorter wavelength consists in using gas mixtures of the Ar–Cl_2 type operating at λ = 258 nm [Cl_2(D'–A')] and 175 nm [ArCl(B–X)]. Using these media provides for the excimer lamp operation in the gas flow regime. In most of the excimer emitters, the working gas mixtures are prepared and admitted into the lamp at a residual pressure of 10–30 Pa and, hence, contain small air admixtures. The influence of this gas mixture component on the excimer lamp operation is still insufficiently studied.

Below, we report on the results of a spectroscopic investigation of the longitudinal dc glow discharge plasma in Ar–air and Ar–Cl_2–air gas mixtures under the conditions close to those in low-pressure electric-discharge-pumped excimer lamps.

The glow discharge was generated in a quartz or sapphire tube with an internal diameter of 5 mm. The distance between cylindrical anode and cathode was 100 mm. In order to prevent from the cataphoresis development and provide for the replacement of a discharge-heated gas mixture, the tube edges were open and the whole tube was placed into a 10-liter buffer chamber. The chamber was connected to a 0.5-m-long vacuum monochromator via a CaF_2 window. The radiation detection system was analogous to that described elsewhere [3, 4]. The glow discharge was generated using a high-voltage rectifier ($U_{ch} \le 30$ kV, $I_{ch} \le 100$ mA). The working gas mixtures were prepared in a special mixer evacuated to a residual air pressure of 0.013 kPa.

Figure 1 shows a typical current–voltage (*I*–*U*) characteristic measured in a system filled with an Ar–air mixture and a plot of the power supplied to the discharge versus current. As the I_{ch} value increases from 1 to 10 mA, the voltage between electrodes of the discharge tube decreased from 2.0 to 1.0 kV (subnormal glow discharge regime [5]), and upon further increasing the current, the discharge operated in the normal mode. On adding chlorine to the Ar–air mixture (P = 0.1–0.6 kPa), the U_{ch} value (for I_{ch} 1–2 mA) increased to 3.5–5.0 kV. The region of existence of a subnormal discharge (with respect to current) decreased to 4–5 mA. In the normal discharge operation regime ($I_{ch} \ge 6$ mA), the U_{ch} value was 2.3–2.8 kV.

Figure 2 shows an emission spectrum of the glow discharge in argon containing a small air admixture. The spectrum is characterized by a set of narrow molecular emission bands with a width of ~1.5 nm (FWHM) slightly broadened on the shortwave side. Since the emission spectra of a glow discharge generated under similar conditions in pure Kr or Xe did not show such

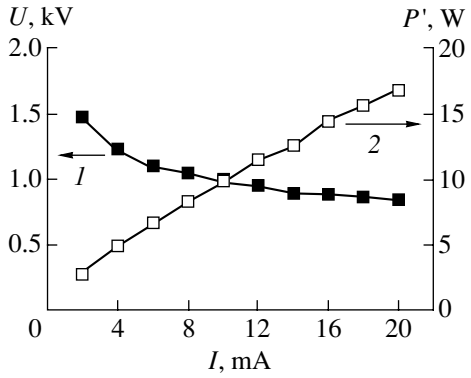

Fig. 1. Typical characteristics of a dc glow discharge in an Ar–air mixture (6.0/0.013 kPa): (*1*) current–voltage curve; (*2*) plot of the power supplied to the discharge versus current.

The intensity of molecular nitrogen bands emitted from an excimer lamp pumped with longitudinal dc glow discharge in an Ar–air mixture (4.0/0.013 kPa; I_{ch} = 5 mA)

λ, nm	193	204	214	227	235	247	258	273
J/k_λ, a.u.	0.05	0.16	0.28	0.34	0.45	0.32	0.17	0.09

components, we attribute the band spectrum to a small air admixture in argon. Interpretation of the observed emission spectrum based on the data taken from [6, 7] showed that the most intense bands in the region of 214–271 nm (see table) can be assigned to the third Kaplan system of $N_2(A^3\Sigma_u^+–E)$, while the bands at λ = 235 nm belong to the fourth positive system of nitrogen molecules $N_2(B^3\Pi_g–D^3\Sigma_u^+)$ and a weak band at λ = 258 nm is probably due to Cl_2(D'–A'). Chlorine could be supplied to the mixture as a result of desorption from the walls of the discharge chamber, where inert gas–chlorine mixtures were studied previously.

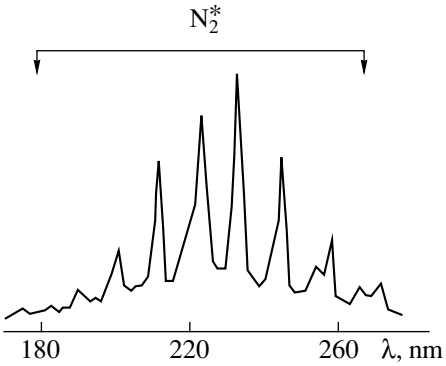

Fig. 2. A typical emission spectrum of the glow discharge in argon–air mixture (4.0/0.013 kPa; I_{ch} = 5 mA).

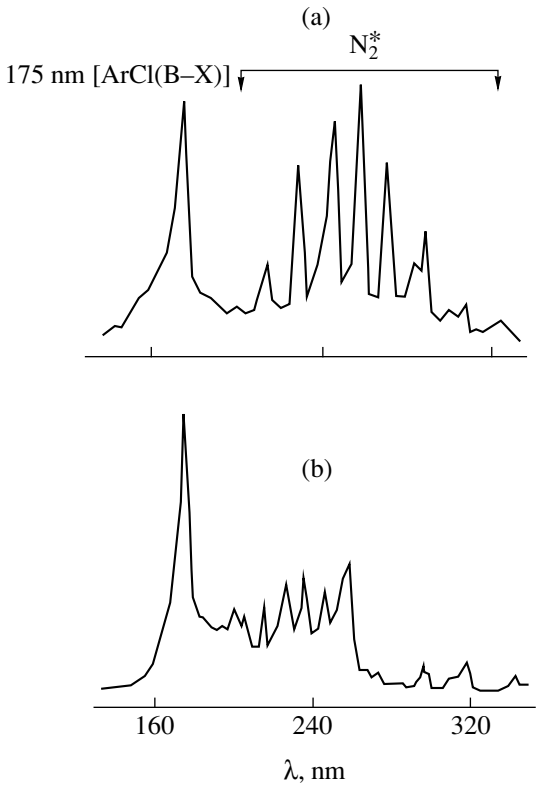

Fig. 3. The emission spectra of longitudinal dc glow discharge in various argon–chlorine air mixtures (I_{ch} = 5 mA): (a) 4.0/0.04/0.013 kPa; (b) 2.9/0.13/0.013 kPa.

The emission spectrum of a glow discharge observed from an Ar–Cl_2–air mixture with a low chlorine content ($P \le 0.04$ kPa) contains the bands at 258 nm [Cl_2(D'–A')] and 175 nm [ArCl(B–X)] together with the above molecular nitrogen bands (Fig. 3a). As the content of chlorine in the mixture grows ($P \ge 0.2$ kPa), the nitrogen bands decrease in intensity and increase in width (Fig. 3b). For an excimer lamp operated under optimum conditions for the 258/175 nm band emission (P_{Ar} = 2–4 kPa; P_{Cl_2} = 0.3–0.5 kPa; $I_{ch} \le 30$ mA), an average output power in the 170–270 nm wavelength interval was 0.7–1 W at an efficiency of 3–5%.

Thus, the effect of residual gases on the optical characteristics of excimer lamps operating at λ = 175/258 nm is most pronounced in devices using Ar–Cl_2 mixtures with small chlorine content ($P_{Cl_2} \le$ 0.04 kPa). The glow discharge in an Ar–Cl_2 mixture with P_{Ar} = 2–4 kPa and P_{Cl_2} = 0.3–0.5 kPa provides for an output radiation power of 0.7–1 W at an efficiency of 3–5%. The Ar–Cl_2–air mixtures can be used in excimer lamps operating in the gas flow regime which are intended for applications in photometry, high-energy chemistry, biophysics, and medicine.

REFERENCES

1. A. P. Golovitskiĭ and S. N. Kan, Opt. Spektrosk. **75** (3), 604 (1993) [Opt. Spectrosc. **75**, 357 (1993)].
2. A. P. Golovitskiĭ and S. V. Lebedev, Opt. Spektrosk. **82** (3), 251 (1997) [Opt. Spectrosc. **82**, 227 (1997)].
3. A. K. Shuaibov and A. I. Dashchenko, Kvantovaya Élektron. (Moscow) **30**, 279 (2000).
4. A. K. Shuaibov, Pis'ma Zh. Tekh. Fiz. **25** (9), 1 (2000) [Tech. Phys. Lett. **26**, 357 (2000)].
5. Yu. P. Raĭzer, *Gas Discharge Physics* (Nauka, Moscow, 1987; Springer-Verlag, Berlin, 1991).
6. L. Wallace, Astrophys. J., Suppl. Ser. **62**, 445 (1962).
7. R. W. B. Pears and A. G. Gaydon, *The Identification of Molecular Spectra* (Chapman and Hall, London, 1963).

Translated by P. Pozdeev

Technical Physics Letters, Vol. 27, No. 5, 2001, pp. 356–358. Translated from Pis'ma v Zhurnal Tekhnicheskoĭ Fiziki, Vol. 27, No. 9, 2001, pp. 13–19.

Optical Pulsating Discharge Plasma Dynamics in a Supersonic Jet: Experiment and an Analytical Model of the Quasistationary Flow Development

V. I. Yakovlev

Institute of Theoretical and Applied Mechanics, Siberian Division, Russian Academy of Sciences, Novosibirsk, Russia
e-mail: yakovlvi@itam.nsc.ru

Received December 1, 2000

Abstract—An analytical method for determining the wave structure and quasistationary flow parameters of an optical pulsating discharge plasma expanding in a supersonic flow is developed. The method is based on a physical model of the optical gas breakdown, a theory of the point explosion, the results of numerical modeling of the breakdown plasma dynamics along a laser beam, experimental data, and numerical estimates. © *2001 MAIK "Nauka/Interperiodica".*

Previously [1, 2], a considerable volume of numerical calculations and a large number of experiments were performed in order to reveal new possibilities of controlling supersonic flows and body streamlining by means of localized energy supply. In analyzing the results of experiments with optical pulsating discharge (OPD) [3, 4], we developed an approach that allowed us to determine the conditions for transition to the quasistationary flow and explain the wave structure configuration observed in the region of energy supply. Below, we will justify this approach using an analysis of the OPD plasma dynamics, which completes the development of a simplified (neglecting dissipative and nonstationary processes) analytical model capable of predicting the wave structure and parameters of a quasistationary flow during the pulsed laser action upon a supersonic flow.

According to the known mechanisms of the discharge propagation along a laser beam [5, 6], a sharply focused laser radiation is absorbed within a thin layer (with a diameter smaller than that of the laser beam) behind the laser-supported detonation wave (LSDW) front. The LSDW front propagation velocity V is determined by the following formula [5]: $V = [2(\gamma^2 - 1)W/s\rho_0]^{1/3}$, where γ is the effective adiabate exponent; W and s are the laser beam power and cross section, respectively; and ρ_0 is the initial gas density. In the experiment with CO_2 laser [2] with $W/s = 10^8$–10^9 W/cm^2, the V values fell within the supersonic range (several km/s). The flow parameters behind the wave front (indicated by subscript w) are given by the known relationships for a detonation wave (we use the conventional notations): $\rho_w/\rho_0 = (\gamma + 1)/\gamma$; $P_w/\rho_0 V^2 = 1/(1 + \gamma)$; $\varepsilon_w/V^2 = \gamma/(\gamma + 1)^2(\gamma - 1)$; $\beta = \gamma\varepsilon_w$; and $u_w = c_w = \gamma V/(\gamma + 1)$. For the experimental conditions studied in [2] with the laser pulse repetition rate $f = 100$ kHz, these formulas yield $V = 5.7$ km/s, $P_w = 340$ atm, and $\varepsilon_w = 40$ MJ/kg. The argon plasma temperature is ≈25000 K and the effective adiabate exponent is $\gamma \approx 1.2$. These parameters are obtained within a narrow LSDW region with a focused laser beam diameter not exceeding $r_0 = 0.10$–0.12 mm.

When the plasma expands, a thermal wake is formed in the main flow. According to the results of numerical modeling [7], the field of a stationary plasma flow corresponds to underexpanded efflux from a sonic nozzle (with a velocity c_w) into a cocurrent hypersonic flow (with a velocity V), with the medium being accelerated to high velocity over a distance equal to several hundred nozzle diameters (r_0). It was also demonstrated that the shock wave radius and the pressure distribution in the asymptotic region (at a distance $x \gg r_0$ from the wave front) are close to those calculated within the framework of the point explosion model, while the other parameters can be obtained by calculations assuming the isotropic flow because of a weak intensity of shock waves in the inner flow region.

In experiments on the visualization of a flow with OPD, the thermal wake was observed under quasistationary flow conditions [2, 3]: $l \cong u/f \cong V\tau$, where l is the breakdown plasma length, u is the supersonic flow velocity, and τ is the laser pulse duration. A large wake length (not shorter than $300r_0$) allows the dissipation processes (vortex formation and gas–plasma flow mixing) to be neglected in the initial stage of the thermal wake formation. In the vicinity of the discharge, a shock wave (SW) is formed (similar to that generated as a result of streamlining) representing a superposition of nonstationary SWs generated by every breakdown. The SW configuration $r(x)$ is close to that calculated within the framework of the point explosion model [8] with $x = ut$. The thermal wake radius also coincided

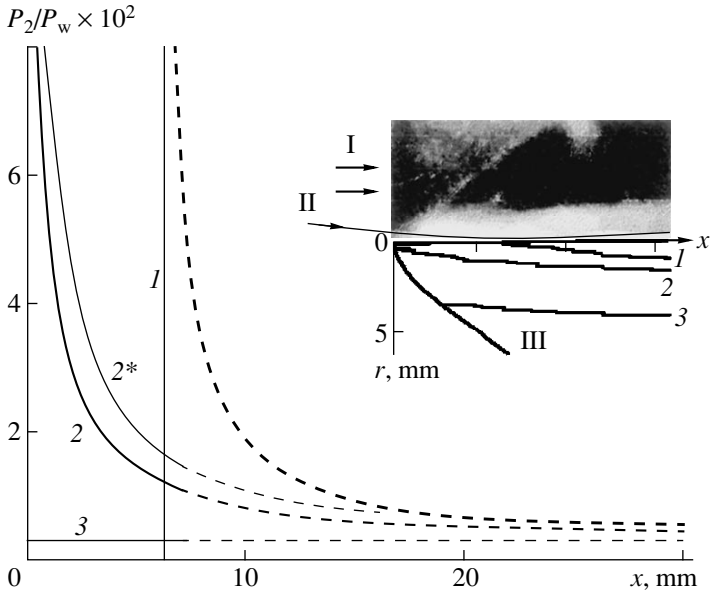

Fig. 1. Relative pressure profiles in the optical discharge region at various time instants after breakdown $t = 0$ (*1*), τ (*2*), and $1/f$ (*3*); curve *2** was calculated with an allowance for the radial plasma expansion. The inset shows a comparison of the calculated distributions with the photographic image of the visualized flow near the breakdown region: I, supersonic flow; II, laser beam; III, shock wave.

with the value calculated for a high ($V \gg u$) discharge propagation velocity [4]. Despite a considerable time interval between laser pulses ($1/f > \tau$), a quasistationary solution for the thermal wake is close to the stationary one for the same W/s ratio. This result is explained by the dynamics of pressure variation in the breakdown region.

Since the strong explosion (self-similarity) condition was not fulfilled in the experiment, we used an approximate solution of cylindrical symmetry ($r_0 \gg l$) with an allowance for the counter pressure [9]. Figure 1 shows the profiles of relative pressure $P_2(x)/P_w$ in the wave front calculated for various time moments, including the initial instant $t = 0$ of the laser pulse action (vertical line *1*, $P_2 = P_w$), laser pulse termination at $t = \tau = 1.1$ μs (curve *2*), and the next laser pulse arrival at $t = 10$ μs for $f = 100$ kHz (curve *3*). The x axis coincides with directions of the gas flow and the laser radiation propagation. The laser beam is focused at the point with $x = 6.3$ mm ($t = 0$). The LSDW propagates in the opposite direction and at $t = \tau$ occurs at $x = 0$. Dashed lines continue the solutions to the expanded x (or t) region to show the pressure profile (dynamics) in the case of unlimited duration of the laser action. Actually, the breakdown takes place within a limited interval of $x \cong 0$–6.3 mm ($=l = V\tau$), so that real pressure profiles have somewhat different shapes.

However, there is an important characteristic feature of the process studied: the pressure exhibits a very sharp drop at a distance of situated several beam diameters (~1 mm) behind the LSDW front. As a result, the pressures of plasma and gas flow become close even at a distance on the order of l irrespective of the LSDW front position. This implies that, behind the nonstationary optical breakdown region, there is a certain quasistationary (i.e., slowly varying with time) level of pressure and, accordingly, of the other parameters. Repeating laser pulses maintain the established flow regime. The level of pressure in this established regime is determined by comparing the results of visualization, the intrinsic wake emission, and the values of $r(x)$ calculated for various time instants after the beginning of the laser pulse action. The inset in Fig. 1 shows these solutions (curves *1*–*3*) on a common scale with half of the flow image (photograph) near the breakdown region. The results of calculation (*2*) and experiment are close for $t = \tau$, where a maximum amount of gas is involved in the motion.

For this reason, the pressure profile at the moment of termination of the laser pulse is used for calculating the other parameters of flow in the wake. The pressure at the flow center (after explosion) is determined using the condition of self-similarity between the pressure profile and the pressure ("plateau") level βP_2 [8], where $\beta = 0.43$ for $\gamma = 1.2$. This condition is also valid (albeit within a limited range of parameters) for relatively weak waves, which must be taken into account at large $r(x)$ by appropriately changing the β value. Using a parameter $p = \beta P_2/P_w$ to describe the degree of plasma pressure reduction in the isentropic flow [7], we obtain the following relationships: $b/b_w = p^n$ and $\rho/\rho_0 = p^{(1-n)}(1+\gamma)/\gamma$, where $n = (\gamma - 1)/\gamma$. Expressions for the plasma flow velocity u_p and the Mach number (in the thermal wake) are determined in a similar manner:

$$u_p/V = [1 + 2(1 - p^n)/(\gamma - 1)]^{1/2}\gamma/(1 + \gamma),$$

$$M_p = (u_p/V - 1)(1 + \gamma)/\gamma p^{n/2}.$$

Figure 2 shows the results of calculations of (a) the enthalpy distribution and (b) the relative decelerating

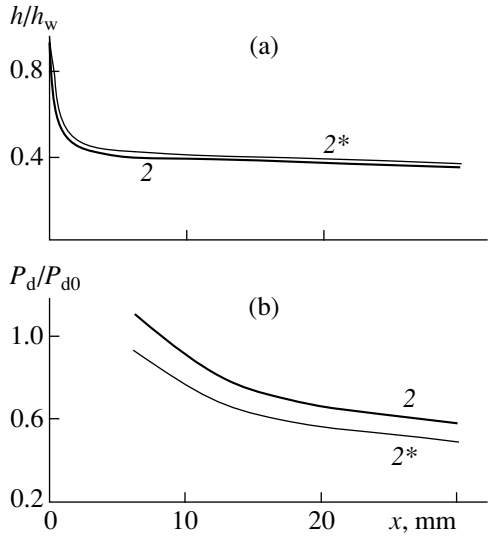

Fig. 2. Profiles of (a) relative enthalpy h/h_w and (b) relative decelerating pressure P_d/P_{d0} in the region behind the optical pulsating discharge in a supersonic ($M = 2$) argon flow. See the text for explanations.

pressure P_d/P_{d0} (with respect to the major flow pressure P_{d0} in the absence of plasma) behind the OPD (f = 100 kHz) in a supersonic ($M = 2$) argon flow. We used the same adiabate exponent as above ($\gamma = 1.2$), which was justified by numerical estimates. Upon going to the quasistationary region, a decrease in the enthalpy corresponds to a decrease in the temperature to 12500 K. The gas density in the thermal wake also significantly decreases (by two orders of magnitude). The Mach number is relatively low ($M_p \approx 1.4$) despite a high flow velocity (>2.6 km/s in the laboratory frame), which is explained by a high local sound velocity. Owing to the radiant energy supply, the retarding pressure decreases by a factor of 1.5–2 in the near wake region (x = 10–20 mm). This behavior correlates with the results of measurements [2, 4] that show a decrease of up to 50% in the aerodynamic resistance of streamlined bodies under similar conditions. Thus, a high-temperature rarefied supersonic flow (thermal wake) is formed at a distance on the order of $l \approx V\tau$ behind the optical breakdown region. An additional indirect evidence is provided by the character of emission: a high brightness of the breakdown plasma sharply changes to a relatively weak emission from regions downward the flow.

Using the proposed model, we may evaluate the effect of a non-one-dimensional flow character related to the radial expansion and the role of radiative losses in the breakdown plasma region. The former effect is evaluated by introducing an additional parameter [5] $\delta = 1/(1 + 2c_w\Delta x/Vr_0)$ and using the effective value $\delta(W/s)$ instead of W/s. Since $c_w/V = \gamma(\gamma + 1) \approx 0.5$, the path of the light quantum is $\Delta x \sim 2r_0$ (LSDW existence condition), which yields a minimum estimate of $\delta \approx 0.5$. Because the laser power density used in the experiments only slightly exceeded the threshold, we performed calculations using this estimate. The results are presented in Figs. 1 and 2 (curves *2**). A relatively small change in the flow parameters is explained by weak dependence of V on the power ($V \sim W^{1/3}$) and by a small decrease in P_w.

The radiation losses are estimated by a limiting value of the integral radiant flux $S_r(x) = 4\pi\int\varepsilon_s(T, n_E, n_I)dx$ from the breakdown plasma region of length x behind the LSDW front. We used an approximate expression for the spectral integral of the radiating capacity ε_s of a high-density argon plasma (derived in [10] for a continuous optical discharge) and the calculated distributions of parameters behind the LSDW front. The role of radiant energy losses in the total energy balance is evaluated by a comparison of the radiant flux to the mass energy flux $S_m \approx \rho_0 V b_w$. Under the experimental conditions studied, $S_m \approx 6.3 \times 10^7$ W/cm^2, which correlates with the laser radiant flux density $W/s \approx (0.5–1) \times 10^8$ W/cm^2 ensuring the gas heating and transport in the optical breakdown region. The calculated distribution of the integral radiating capacity of the argon plasma behind the LSDW front exhibits a sharp drop (by three orders of magnitude) at a distance of about the transverse beam size (not exceeding 0.2 mm). This very region produces the dominating contribution (2.2×10^6 W/cm^2) to the total radiant flux density $S_r = 2.24 \times 10^6$ W/cm^2 over the entire length (6.3 mm) of the breakdown region. Thus, $S_r/S_m = 0.036 \ll 1$, which indicates that the role of radiative energy losses is insignificant.

REFERENCES

1. V. M. Fomin, P. K. Tretyakov, and V. I. Yakovlev, in *Proceedings of the International Conference on the Methods of Aerophysical Research, Novosibirsk, 1996*, Part 2, p. 210.
2. P. K. Tret'yakov, A. F. Garanin, *et al.*, Dokl. Akad. Nauk **351** (3), 339 (1996) [Phys. Dokl. **41**, 566 (1996)].
3. P. K. Tret'yakov and V. I. Yakovlev, Pis'ma Zh. Tekh. Fiz. **24** (6), 8 (1998) [Tech. Phys. Lett. **24**, 626 (1998)].
4. P. K. Tret'yakov and V. I. Yakovlev, Dokl. Akad. Nauk **365** (1), 58 (1999) [Dokl. Phys. **44**, 178 (1999)].
5. Yu. P. Raizer, *Gas Discharge Physics* (Nauka, Moscow, 1987; Springer-Verlag, Berlin, 1991).
6. V. I. Fisher, Zh. Tekh. Fiz. **53** (11), 2143 (1983) [Sov. Phys. Tech. Phys. **28**, 1312 (1983)].
7. P. D. Thomas, AIAA J. **15** (10), 1405 (1977).
8. L. I. Sedov, *Similarity and Dimensional Methods in Mechanics* (GITTL, Moscow, 1957; Academic, New York, 1959).
9. V. P. Korobeĭnikov, *Problems of the Theory of Point Explosion* (Nauka, Moscow, 1985).
10. G. I. Kozlov, V. A. Kuznetsov, and V. A. Masyukov, Zh. Éksp. Teor. Fiz. **66** (3), 954 (1974) [Sov. Phys. JETP **39**, 463 (1974)].

Translated by P. Pozdeev

Technical Physics Letters, Vol. 27, No. 5, 2001, pp. 359–361. Translated from Pis'ma v Zhurnal Tekhnicheskoĭ Fiziki, Vol. 27, No. 9, 2001, pp. 20–24.

Measuring the Thickness of Thin Liquid Films on Solid Surfaces Using the Laser-Induced Thermocapillary Response

B. A. Bezuglyĭ and A. A. Fedorets

Tyumen State University, Tyumen, Russia

e-mail: bezuglyi@tsu.tmn.ru

Received October 25, 2000

Abstract—A contactless method based on the laser-beam-induced thermocapillary effect is proposed for measuring the thickness of a thin liquid film on a flat solid surface. The method can be also used to measure the films with inhomogeneous thicknesses formed on a nonhorizontal substrate. © *2001 MAIK "Nauka/Interperiodica".*

There are many processes in the evaporation–condensation systems [1], lacquer and paint industry [2], and some chemical film technologies that require monitoring of the thickness of liquid layers on solid substrates. Most of the well-known methods used for the film thickness determination (ultrasonic, capacitive, inductive, etc.) were developed predominantly for measuring solid films. These methods frequently imply mechanical contact of a probing transducer with the object and cannot be used in practice for high-precision determination of the thickness of thin (below 1 mm) liquid layers. Application of the contactless interference techniques is limited by the relatively high cost and complexity of the measuring equipment and by the usual presence of hardly avoidable vibrations of the free liquid surface, which usually hinder the interference measurements.

We propose determining the thicknesses of liquid layers on solid surfaces using a method based on the photoinduced thermocapillary convection (PTCC) effect. The method employs a strong dependence of the steady-state laser-induced thermocapillary (TC) response[1] on the thickness of a liquid layer [3]. The shape and size of the TC response pattern are determined by the properties of the liquid (viscosity, surface tension, temperature coefficient of the surface tension, optical absorption coefficient), film geometry (thickness and its inhomogeneity, static curvature of the free liquid surface), probing laser beam parameters (power, diameter, divergence), and substrate properties (thermal conductivity, optical absorption coefficient).

A relationship between the TC response pattern diameter D and the thickness h of a plane-parallel layer[2] was established [4, 5] for absorbing liquid films with thicknesses 190–1000 μm and viscosities $\mu = (0.81–68) \times 10^{-3}$ Pa s probed at a laser beam power P = 2.6–8 mW. The case of a transparent liquid film on absorbing substrate was also studied in [4], where parameters of the TC response were studied as functions of the substrate thermal conductivity and optical absorption coefficient. Previously, Da Costa and Calatroni [6] showed that the PTCC can be induced in liquids with a viscosity of up to 1 Pa s; however, the effect of the liquid layer thickness on the TC response was not studied. According to [4, 5], the relationship between D and h can be used for determining the film thickness variations Δh with a resolution of 1 μm. An increase in the thermal conductivity of the substrate and/or in the viscosity of the liquid decreases the TC response pattern size D and reduces the sensitivity.

In view of the relative complexity of the PTCC phenomenon, it is necessary to develop a simple but effective method of obtaining the calibration curves for each particular liquid–substrate system. Previously [4, 5], the h values were monitored by measuring the volume of liquid in a vessel of known shape or by placing special calibration wires with known thicknesses onto the substrate [4]. However, these procedures are rather intricate and sufficient accuracy can be achieved only by a highly skilled experimenter.

It was found that the TC response pattern from a wedge-shaped liquid layer formed on an oblique substrate can be characterized by two mutually perpendicular diameters. One of these coordinates (Fig. 1, D_α) increases with the dihedral wedge angle α, while the other (Fig. 1, D_h) is a constant value determined by the thickness h of a liquid layer in the cross section passing

[1] TC response represents an interference pattern observed on a screen placed in the caustic cross section of a part of the convection-inducing laser beam reflected from a TC-vortex deformed (concave) free liquid surface.

[2] For a homogeneous layer with constant thickness, the response pattern has a circular shape.

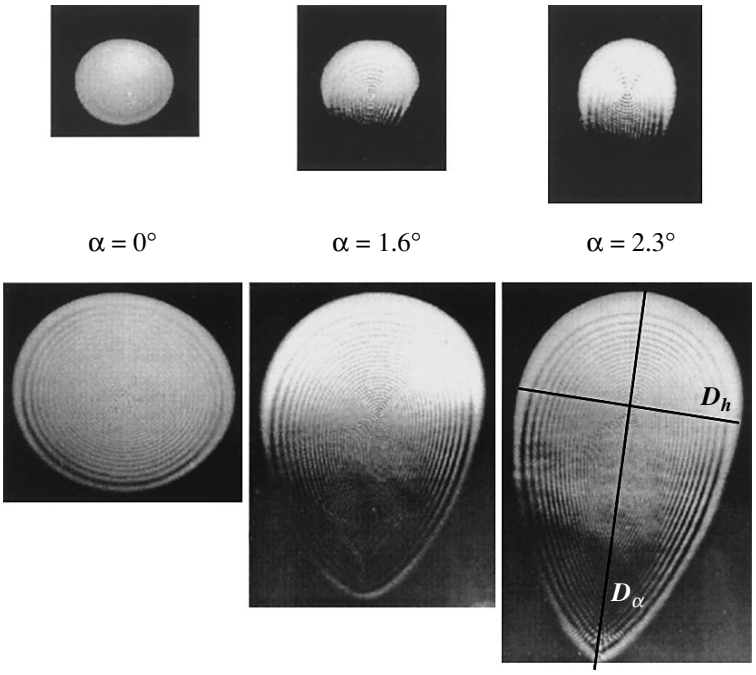

Fig. 1. Photographs of the TC response patterns from homogeneous (horizontal substrate, α = 0) and inhomogeneous (inclined substrates, α = 1.6° and 2.3°) octane layers on hard rubber substrates. The α angle was varied by rotating a substrate around the horizontal axis crossing the beam axis. The film thickness on the beam axis is 260 μm (top row) and 200 μm (bottom row).

through the beam center and perpendicular to the thickness gradient. Exact calibration curves are obtained by scanning over the liquid layers with preset α values (Fig. 2).

Figure 2 shows the plots of D_h versus h for various liquids normalized to the beam diameter d which would be observed on the screen for the beam reflected from a flat free liquid surface. A preset laser beam power determines the optimum interval of thicknesses to be measured. On the side of thin layers, this interval is bounded by the condition of broken layer continuity [7], and on the side of thick layers, by a decrease in the local response sensitivity (the latter can be defined as $[\Delta(D_h d^{-1})/\Delta h] \times 100\%$, where Δh corresponds to a portion of the plot that can be approximated by straight line). As the laser beam power increases, the optimum interval of measurements shifts toward greater thickness. At a fixed power, the interval of measurements is broader and the TC response sensitivity is higher for the liquids of lower viscosity. For example (Fig. 2), the TC response sensitivity in the film thickness range 300–320 μm increases in the series of liquids from Vaseline oil to octane, 1-butanol, and benzyl alcohol (viscosities at 20°C: 27, 5.22, 3.64, and 0.77 cSt), amounting to ~3.4, 4.5, 6.3, and 8.5% of d per μm layer thickness, respectively. The time required for stabilization of the TC response pattern typically varies from a few seconds to several tens of seconds.

The proposed method is simple, highly sensitive, requires no expensive equipment, and ensures contactless determination of the local thickness of a wedgelike liquid layer. This method can be used both for monitoring modern technological processes and for studying various systems of liquid layers on solid substrates.

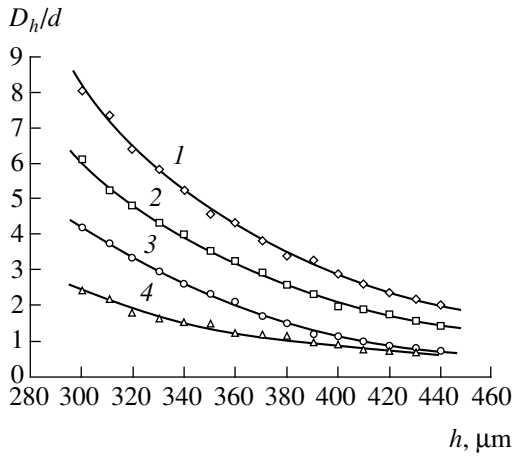

Fig. 2. Normalized calibration curves of the TC response pattern diameter D versus liquid film thickness h for (*1*) octane, (*2*) 1-butanol, (*3*) benzyl alcohol, and (*4*) Vaseline oil layers on a hard rubber substrate with a diameter of 30 mm and a thickness of 3 mm inclined at α = 2.25°. Probing conditions: He–Ne laser (LGN-207a); λ = 663 μm; P = 1.2 mW; beam divergence, 1.85 mrad; optical path of beam from laser to screen, 370 cm.

Acknowledgments. This study was partly supported by the Fundamental Natural Sciences Program of the Ministry of Education of the Russian Federation (project no. 97-0-8.1-60).

REFERENCES

1. O. A. Kabov, Doctoral Dissertation (Inst. Teplofiziki, Sib. Otd. Ross. Akad. Nauk, Novosibirsk, 1999).
2. A. D. Yakovlev, *Chemistry and Technology of Lacquer and Paint Coatings* (Khimiya, Leningrad, 1981).
3. B. A. Bezuglyĭ, O. A. Tarasov, A. A. Fedorets, *et al.*, RF Patent No. 98114578, Byull. Izobret., No. 14 (2000).
4. B. A. Bezuglyĭ, Candidate's Dissertation (Mosk. Gos. Univ., Moscow, 1983).
5. V. V. Nizovtsev, Inzh.-Fiz. Zh. **55** (1), 85 (1988).
6. G. Da Costa and J. Calatroni, J. Appl. Opt. **18** (2), 233 (1979).
7. B. A. Bezuglyĭ and A. A. Fedorets, in *Proceedings of the 3rd International Aerospace Congress, IAC'2000* (SIR RIA, Moscow, 2000).

Translated by P. Pozdeev

Technical Physics Letters, Vol. 27, No. 5, 2001, pp. 362–364. Translated from Pis'ma v Zhurnal Tekhnicheskoĭ Fiziki, Vol. 27, No. 9, 2001, pp. 25–30.

Special Features of the Distributed Feedback Lasers Based on Gyrotropic Cubic Crystals

G. V. Kulak

Mozyr State Pedagogical Institute, Mozyr, Gomel oblast, Belarus

e-mail: mozinst@mail.ru

Received October 26, 2000

Abstract—The oscillation conditions were determined for the distributed feedback lasers based on gyrotropic cubic crystals. The frequencies of clockwise (counterclockwise) polarized longitudinal eigenmodes decrease (increase) by $\omega_\rho = \rho c/n$ (ρ is the specific optical rotation of the crystal, n is the index of refraction, c is the speed of light in vacuum) relative to the Bragg frequency $\omega_0 = \pi c/\Lambda n$ (Λ is the phase grating period). The gain threshold is higher for the clockwise than for the counterclockwise polarized waves. © *2001 MAIK "Nauka/Interperiodica".*

Gyrotropic cubic crystals of the sillenite type ($Bi_{12}SiO_{20}$, $Bi_{12}GeO_{20}$, $Bi_{12}TiO_{20}$, etc.) exhibiting a considerable photorefractive (PR) effect find application in the devices for data processing, interferometry, and holographic memory [1, 2]. Kaminskiĭ *et al.* [3] reported on a continuous surface lasing from $Bi_{12}SiO_{20}$:Nd^{3+} crystals in a cavity pumped with a Ti^{3+}:Al_2O_3 laser tuned to $\lambda_p = 0.814$ μm for the [100] crystallographic direction. The feedback in the surface-emitting laser was provided by high-reflectance mirrors; the threshold pumping power necessary for the $\lambda_{sc} = 1.0716$ μm emission was about 18 mW.

Distributed feedback (DFB) lasers are widely used in various fields of science and technology [4, 5]. The reflection phase grating in a PR crystal, which is the main element of DFB lasers, is formed by coherent light waves at large conversion angles of the interfering beams [1, 6]. The features of light diffraction in the Bragg backscattering geometry in gyrotropic cubic crystals were studied in [6, 7]. It was established that there are two diffraction regimes [7] in which the diffraction efficiency either monotonically increases with the coupling constant χ or oscillates, depending on whether the specific optical rotation ρ of the crystal is small ($\rho^2 \le \chi^2$) or large ($\rho^2 > \chi^2$), respectively. In uniaxial and biaxial crystals, the gyrotropic properties are manifested only in the directions of light propagation close to the optical axes. In cubic crystals, this property has to be taken into account for any direction of the light wave propagation [8].

Consider a phase grating situated in the region of a laser medium between planes $z = 0$ and $z = 1$. The incident light wave is linearly polarized and can be represented as a sum of clockwise and counterclockwise polarized waves $\mathbf{A} = A_{01}\mathbf{e}_+ + A_{02}\mathbf{e}_-$, where A_{01} and A_{02} are the amplitudes of the circularly polarized components and $\mathbf{e}_\pm = (\mathbf{e}_1 \pm i\mathbf{e}_2)/\sqrt{2}$ are the unit circular vectors ($\mathbf{e}_1 \| 0x$, $\mathbf{e}_2 \| 0y$).

As is known, the main parameters of DFB lasers (lasing threshold, longitudinal mode frequency, etc.) can be determined within the framework of a phenomenological theory based on solving a system of Maxwell equations and material equations for a gyrotropic medium [8, 9]. A wave equation for the light field strength $\mathbf{E}$ in a DFB laser medium is as follows:

$$\nabla^2\mathbf{E} - \frac{\varepsilon}{c^2}\frac{\partial^2\mathbf{E}}{\partial t^2} - \frac{2\alpha}{c^2}\frac{\partial^2}{\partial t^2}\mathrm{rot}\mathbf{E} = \frac{1}{2c^2}\frac{\partial^2}{\partial t^2}(\Delta\varepsilon^{\phi *}\mathbf{E} + \Delta\varepsilon^{\phi}\mathbf{E}), \quad (1)$$

where $\varepsilon = \varepsilon' + i\varepsilon''$ is the complex dielectric permittivity of the laser crystal ($\varepsilon'' < 0$); α is the optical activity parameter; c is the light speed in vacuum; $\Delta\varepsilon^{\phi} = \Delta\varepsilon_0^{\phi}\exp(iKz)$, $\Delta\varepsilon_0^{\phi}$ being the PR grating amplitude, $K = 2\pi/\Lambda$, and Λ the grating period; and the asterisk denotes a complex conjugate.

A solution to the wave equation (1) can be found in the form of a sum of two coupled waves $\mathbf{E}_0(z)$ and $\mathbf{E}_1(z)$ with slowly varying complex amplitudes:

$$\mathbf{E} = [\mathbf{E}_0(z)e^{ik_0 z} + \mathbf{E}_1(z)e^{-ik_0 z}]e^{-i\omega t}, \quad (2)$$

where $k_0 = \left(\frac{\omega}{c}\right)n$, $n = \sqrt{\varepsilon'}$ being the refractive index of the medium. Substituting expression (2) into Eq. (1),

we obtain a set of equations for the coupled waves:

$$\frac{d\mathbf{E}_0}{dz} = i\hat{\chi}\mathbf{E}_1 e^{i\frac{1}{2}\Delta k} + \frac{1}{2}g\mathbf{E}_0 + \rho[\mathbf{n}_0, \mathbf{E}_0],$$
$$\frac{d\mathbf{E}_1}{dz} = -i\hat{\chi}^*\mathbf{E}_0 e^{i\frac{1}{2}\Delta k} - \frac{1}{2}g\mathbf{E}_1 + \rho[\mathbf{n}_1, \mathbf{E}_1], \quad (3)$$

where $\hat{\chi} = (\pi/2\lambda_0 n)\Delta\hat{\varepsilon}_0^{\phi}$ is the tensor coupling constant of the diffracted waves, $g = (2\pi|\varepsilon''|/\lambda_0 n)$ is the gain factor [9], $\rho = (\omega/c)^2\alpha$ is the specific rotation of the crystal [8], $\Delta k = (2k - K)$ is the detuning from the phase-lock condition, and $\mathbf{n}_{0,1}$ are the unit vectors in the directions of diffracted waves in the zero and first order of diffraction, respectively.

The set of equations for the coupled waves is solved with the boundary conditions $\mathbf{E}_0(0) = \mathbf{A}$ and $\mathbf{E}_1(l) = 0$. For the light waves propagating along the second-order crystallographic axes (see [2]), we must take $\chi_{xx} = \chi_{yy} = \chi$. A solution to set (3) was obtained in the following form:

$$\mathbf{E}_0(z) = \mathbf{e}_+A_1e^{-a_1z} + \mathbf{e}_+A_2e^{a_1z} + \mathbf{e}_-A_3e^{-a_2z} + \mathbf{e}_-A_4e^{a_2z},$$
$$\mathbf{E}_1(z) = \mathbf{e}_+B_1e^{-a_1z} + \mathbf{e}_+B_2e^{a_1z} + \mathbf{e}_-B_3e^{-a_2z} + \mathbf{e}_-B_4e^{a_2z}, \quad (4)$$

where

$$a_{1,2} = \sqrt{(\gamma^2 + |\chi|^2 - \rho^2) \pm \sqrt{(\gamma^2 + |\chi|^2 - \rho^2)^2 - [\gamma^4 + 2\gamma^2(|\chi|^2 + \rho^2) + (|\chi|^2 - \rho^2)^2]}}$$

and $\gamma = \frac{1}{2}(g - i\Delta k)$. The coefficients A_i, B_i ($i = 1$–4) were determined using the boundary conditions and the obvious relationships $(\mathbf{e}_\pm\mathbf{e}_\pm^*) = 1$, $(\mathbf{e}_\pm\mathbf{e}_\pm) = 0$. The final expressions for the vector amplitudes of diffracted waves are

$$\mathbf{E}_0 = e^{-i\frac{1}{2}\Delta kz}\left\{\mathbf{e}_+A_{01}\frac{\left[a_1\cosh[a_1(l-z)] - \frac{1}{2}(g - i\Delta k_+)\sinh[a_1(l-z)]\right]}{\left[a_1\cosh(a_1l) - \frac{1}{2}(g - i\Delta k_+)\sinh(a_1l)\right]}\right.$$
$$\left. + \mathbf{e}_-A_{02}\frac{\left[a_2\cosh[a_2(l-z)] - \frac{1}{2}(g - i\Delta k_-)\sinh[a_2(l-z)]\right]}{\left[a_2\cosh(a_2l) - \frac{1}{2}(g - i\Delta k_-)\sinh(a_2l)\right]}\right\}, \quad (5a)$$

$$\mathbf{E}_1 = -ie^{i\frac{1}{2}\Delta kz}\left\{\mathbf{e}_+A_{01}\frac{\chi^*\sinh[a_1(l-z)]}{\left[a_1\cosh(a_1l) - \frac{1}{2}(g - i\Delta k_+)\sinh(a_1l)\right]}\right.$$
$$\left. + \mathbf{e}_-A_{02}\frac{\chi^*\sinh[a_2(l-z)]}{\left[a_2\cosh(a_2l) - \frac{1}{2}(g - i\Delta k_-)\sinh(a_2l)\right]}\right\}, \quad (5b)$$

where $\Delta k_\pm = \Delta k \pm 2\rho$. In the absence of gain ($g = 0$), the characteristic constants of set (3) obey the relationship $a_1 = a_2 = \sqrt{|\chi|^2 - \rho^2}$ and the complex amplitudes (5) coincide with the values obtained in [7]; the neglect of gyrotropic properties leads to the well-known expressions for complex amplitudes of the diffracted waves [9].

Expressions (5) indicate that the clockwise and counterclockwise polarized waves in the gyrotropic laser crystal are generated under different conditions. By analogy with [9], these conditions can be written in the following form:

$$a_{1,2} - \frac{1}{2}(g - i\Delta k_\pm)\tanh(a_{1,2}l) = 0. \quad (6)$$

For a large gain ($g \gg |\chi|$), we obtain $a_{1,2} \approx$

$\sqrt{|\chi|^2 - \frac{1}{4}(\Delta k_\pm + ig)^2}$. In this case, expressions (6) lead to the following phase and energy conditions of lasing:

$$-2\arctan\left(\frac{\Delta k_\pm}{g_m}\right) + \Delta k_\pm l - \frac{2|\chi|^2 \Delta k_\pm l}{[g_m^2 + (\Delta k_\pm)^2]} = (2m+1)\pi, \quad (7a)$$

$$\frac{|\chi|^2 e^{g_m l}}{[g_m^2 + (\Delta k_\pm)^2]} = 1, \quad (7b)$$

where $m = 0, \pm 1, \pm 2, \ldots$ is the mode number.

In the vicinity of the Bragg frequency $\omega_0 = \pi c/n\Lambda$ (where $\Delta k_\pm \ll g$), Eq. (7a) yields an expression for the frequencies of clockwise and counterclockwise polarized longitudinal modes:

$$\omega_m = \omega_0 \mp \omega_\rho + \left(m + \frac{1}{2}\right)\frac{\pi c}{nl},$$

where $\omega_\rho = \rho c/n$ is the frequency shift caused by the crystal gyrotropy. Thus, the frequencies of the clockwise polarized modes decrease, while those of the counterclockwise polarized modes increase, by ω_ρ relative to the same mode frequencies in a nongyrotropic crystal. This physical effect is explained by a relative change in the phase velocities of light waves polarized in the opposite sense in the gyrotropic medium.

According to Eq. (7b), the lasing threshold is higher for the modes with counterclockwise than with clockwise polarization. In contrast to the well-known results for a nongyrotropic medium [9], the lasing in gyrotropic crystals is possible at the Bragg frequency ω_0, provided that $\pm\omega_\rho = (m + 1/2)(\pi c/nl)$. For example, for the clockwise polarized zero mode ($m = 0$) with $\lambda_{sc} = 1.0716$ μm in a $Bi_{12}SiO_{20}$ crystal (see [10]), this regime is possible for an active layer thickness of $l = 1.3$ cm.

Recently, Vallet *et al.* [11] theoretically and experimentally studied the frequency beating between the phase-locked laser modes coupled to the two circular polarized laser eigenmodes in an external magnetic field. An analogous beating should be observed in a gyrotropic medium as well. For $\lambda_{sc} = 1.0716$ μm, the polarized beating frequency in a $Bi_{12}SiO_{20}$ crystal is $2\omega_\rho = 28.6$ GHz.

REFERENCES

1. M. P. Petrov, S. I. Stepanov, and A. V. Khomenko, *Photorefractive Crystals in Coherent Optics* (Nauka, St. Petersburg, 1992).
2. L. Solymar and D. J. Cooke, *Volume Holography and Volume Gratings* (Academic, London, 1981).
3. A. A. Kaminskiĭ, S. N. Bagaev, and J. Garcia-Sole, Kvantovaya Élektron. (Moscow) **26** (2), 6 (1999).
4. G. A. Lyakhov, Yu. P. Svirko, and N. V. Suz'ko, Kvantovaya Élektron. (Moscow) **20** (10), 941 (1993).
5. A. A. Afanas'ev, V. M. Volkov, A. N. Rubinov, *et al.*, Kvantovaya Élektron. (Moscow) **29** (2), 123 (1999).
6. J. P. Huignard, J. P. Herrian, G. Rivet, *et al.*, Opt. Lett. **5**, 102 (1980).
7. E. M. Khramovich and V. V. Shepelevich, Izv. Akad. Nauk Belarusi, Ser. Fiz.-Mat. Nauk, No. 2, 106 (1987).
8. F. I. Fedorov, *Theory of Gyrotropy* (Nauka i Tekhnika, Minsk, 1976).
9. A. Yariv and P. Yeh, *Optical Waves in Crystals: Propagation and Control of Laser Radiation* (Wiley, New York, 1984; Mir, Moscow, 1987).
10. V. A. Kizel' and V. I. Burkov, *Gyrotropy of Crystals* (Nauka, Moscow, 1980).
11. M. Vallet, M. Brunel, F. Bretenaker, *et al.*, Appl. Phys. Lett. **74** (22), 3266 (1999).

Translated by P. Pozdeev

Technical Physics Letters, Vol. 27, No. 5, 2001, pp. 365–366. Translated from Pis'ma v Zhurnal Tekhnicheskoĭ Fiziki, Vol. 27, No. 9, 2001, pp. 31–35.

Electron Energy Loss Spectra of NTCDA Organic Films

S. A. Komolov, N. B. Gerasimova, A. G. Sidorenko, Yu. G. Alyaev, and V. A. Novolodskiĭ

Institute of Physics, St. Petersburg State University, St. Petersburg, Russia

Received July 21, 2000; in final form, December 9, 2000

Abstract—The electron energy loss (EEL) spectra of thin NTCDA films on the ZnO(0001) surface were measured. In the low-energy range (<60 eV), the EEL spectra (displaying the characteristic loss peaks at E_{loss} = 4.0, 5.6, 12.5, and 14.5 eV) reflect the structure of transitions between the valence and conduction bands. As the primary electron energy increases, the dominating energy losses are due to the excitation of plasma oscillations at $\hbar\omega_1$ = 6.5 eV (π plasmon) and $\hbar\omega_2$ = 25 eV (π– σ plasmon). © *2001 MAIK "Nauka/Interperiodica".*

In recent years, macromolecular films have drawn the attention of researchers due to some advantageous properties offering good prospects for applications in nano-, micro- and optoelectronic technologies. In particular, thin films of 1,4,5,8-naphthalenetetracarboxylic dianhydride (NTCDA) proved to be capable of acquiring an ordered structure and were studied on various semiconductor [1, 2] and metal [3–5] substrates under ultrahigh vacuum (UHV) conditions. An important problem now is the electron structure formation in NTCDA layers adsorbed on solid surfaces. These films can be used, due to their interesting photoelectron and structural properties [2, 6], in electrical engineering and microelectronics. The process of NTCDA film deposition in vacuum onto ZnO(0001) crystal surface was studied by the number of the secondary-electron techniques including the total electron-beam induced current spectroscopy (TCS), Auger electron spectroscopy (AES), and electron energy loss spectroscopy (EELS). Below, we report some new results obtained by EELS for thin NTCDA layers on the ZnO(0001) surface.

Experimental. The experiments were performed in an UHV setup equipped with a quasispherical four-grid energy analyzer, which can be used for the solid surface characterization by a combination of secondary electron-spectroscopic techniques. The setup also provides for the possibility of depositing the sample films *in situ* and measuring the EELS spectra in the course of the film preparation. In addition, the vacuum chamber was equipped with a sample heating facility and an ion gun for the sputter-cleaning of the sample surface. The heater design allowed the sample temperature to be varied in a controlled manner up to 1000 K, with the temperature monitored by a chromel–alumel thermocouple. The initial NTCDA powder was placed into a Knudsen cell, outgassed by low-temperature annealing for a sufficiently prolonged time, and then evaporated at 450 K for the film preparation.

Prior to the film deposition, a ZnO substrate was cleaned by high-temperature annealing (~1000 K) in vacuum, with the surface cleanness monitored by AES. The ratio of the Auger peak intensities of zinc (59 eV), oxygen (503 eV), and carbon (272 eV) observed in the spectra was 100 : 50 : 1, which indicated a sufficiently clean surface slightly enriched with zinc. The NTCDA films were deposited onto substrates kept at room temperature and monitored by TCS so as to provide for the continuous surface coating. The NTCDA layer thickness (expressed in monolayers of the deposit) was monitored in the course of the film deposition. A monolayer coverage formation was determined by a change in the electron work function of the film. When a desired film was obtained, the sample was characterized by EELS; the spectra were recorded in the form of the electron energy distribution $N(E)$ for various energies E_p of the primary electron beam normally incident on the sample surface. The probing beam current density did not exceed 10^{-5} A/cm^2.

Results and discussion. Figure 1 shows a series of EEL spectra measured at various primary beam energies from 44 to 155 eV. The dashed lines with letters indicate the spectral features of interest. Curves *1* and *2* were measured at a primary beam energy that was relatively low from the standpoint of the energy analyzer, In order to better reveal the spectral features, these spectra were mathematically processed so as to subtract the structureless background determined by the elastically scattered and true secondary electrons. The results of this processing are presented in Fig. 2. This treatment ensured a more precise determination of the characteristic electron energy losses in the low-energy range: A (4.0 eV), B (5.6 eV), C (12.5 eV), and D (14.5 eV).

As is known, the EEL spectra contain information both on the interband transitions from the density of state (DOS) maxima of the conduction band and on the collective electron excitations (plasmons) [7]. The spectra recorded at low excitation energies (Fig. 2) reveal primarily the interband transitions. According to the NEXAFS data [3, 5] the energy band diagram of the NTCDA films contains four maxima of the density of

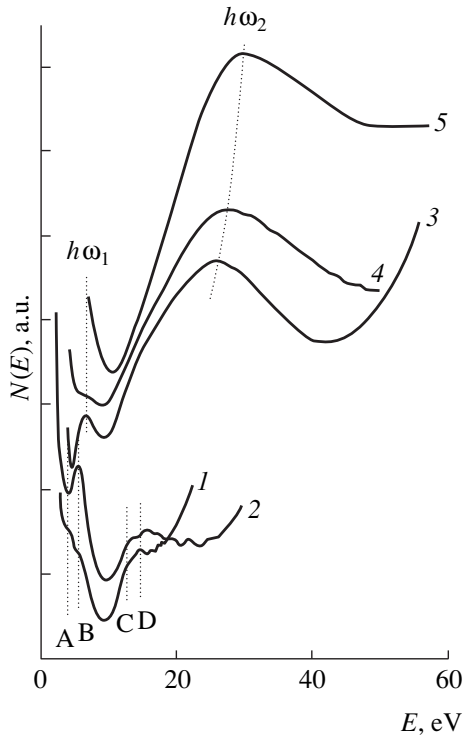

Fig. 1. The EEL spectra of an NTCDA film measured at various primary electron energies E_p = 44 (*1*); 56 (*2*); 85 (*3*); 125 (*4*); 155 eV (*5*). Dashed lies indicate the characteristic energy features A–D.

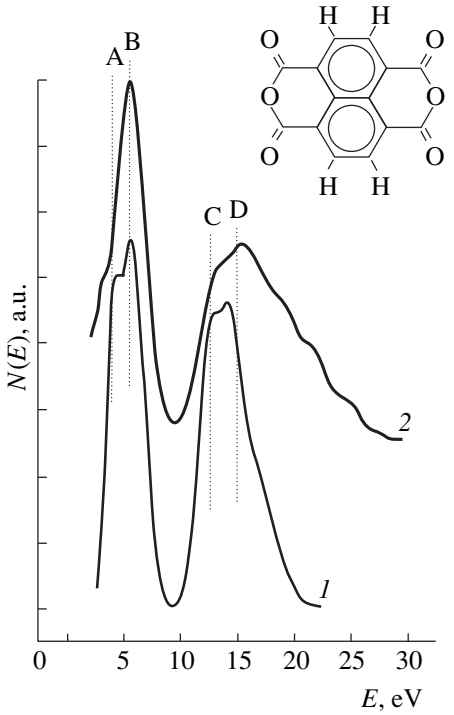

Fig. 2. The EEL spectra of an NTCDA film measured at the primary electron energies E_p = 44 (*1*) and 56 eV (*2*) and mathematically processed so as to reveal the characteristic energy features A–D. The inset shows a structure of the NTCDA molecule.

vacant states π_1^*, π_2^*, π_3^*, and π_4^* (at a distance of 0.5, 2.0, 4.5, and 5.5 eV from the band edge, respectively) and at least three maxima of the density of σ^* states (by our estimates, at a distance of 11, 19, and 30 eV the band edge, respectively). The photoemission data of Gabor *et al.* [3] showed that the valence band of NTCDA contains DOS maxima at 0.5, 1.8, 2.4, 3.8, 5.0, 6.2, 7.3, and 9.7 eV from the valence band edge. According to [2, 8], the bandgap width E_g of NTCDA films is close to 3.1 eV, which coincides with the value obtained from our data on the photoabsorption of NTCDA films deposited onto glass in vacuum. Thus, the loss peak A (4 eV) can be attributed to the interband transitions between π_1 and π_1^* states and peak B (5.6 eV) is assigned to the transitions between π_1 and π_2^* and, probably, between π_2 and π_1^* states. The C(12.5 eV) and D(14.5 eV) can be due to a series of energetically possible interband transitions.

When the primary electron energy increases to 85 eV and above, the EEL spectrum reveals two new features: a narrow peak at $\hbar\omega_1$ = 6.5 eV and a broad maximum at $\hbar\omega_2$ = 25–28 eV these peaks are characteristic of carbon and related compounds. It is highly probable that the former peak reflects the excitation of a bulk plasmon of the carbon π-shell, while the latter is due to excitation of the plasma oscillations of the π and σ bound electrons of carbon.

Acknowledgments. The authors are grateful to Prof. D.R.T. Zahn (Technical University of Chemnitz) for kindly providing NTCDA samples for investigation.

The work was supported by the Russian Foundation for Basic Research (project no. 99-03-33427) and by the Federal Program "Surface Atomic Structures" (project no. 4.3.99).

REFERENCES

1. N. Karl and Ch. Guenther, Cryst. Res. Technol. **34** (2), 243 (1999).
2. R. Strohmaier, C. Ludvig, J. Petersen, *et al.*, Surf. Sci. **351**, 292 (1996).
3. D. Gador, C. Buchberger, R. Fink, and E. Umbach, J. Electron Spectrosc. Relat. Phenom. **96**, 11 (1998).
4. D. Gador, Y. Zou, C. Buchberger, *et al.*, J. Electron Spectrosc. Relat. Phenom. **101**–**103**, 523 (1999).
5. D. Gador, C. Buchenberger, R. Fink, and E. Umbach, Europhys. Lett. **41** (2), 231 (1998).
6. S. R. Forrest, Chem. Rev. **97** (6), 1793 (1997).
7. *Electron Spectroscopy for Surface Analysis*, Ed. by H. Ibach (Springer-Verlag, New York, 1977; Zinatne, Riga, 1980).
8. A. Jayraman, M. I. Kaplan, and P. H. Schmidt, J. Chem. Phys. **82** (4), 1682 (1985).

Translated by P. Pozdeev

Technical Physics Letters, Vol. 27, No. 5, 2001, pp. 367–369. Translated from Pis'ma v Zhurnal Tekhnicheskoĭ Fiziki, Vol. 27, No. 9, 2001, pp. 36–40.

New Scenarios of the Nonlinear Dynamic Transformation of Domain Walls in Uniaxial Magnetic Films with Planar Anisotropy

B. N. Filippov and L. G. Korzunin

Institute of Metal Physics, Ural Division, Russian Academy of Sciences, Yekaterinburg, Russia

Received November 29, 2000

Abstract—The Landau–Lifshits equation was solved by a direct numerical procedure within the framework of a two-dimensional model of the magnetization distribution in a film with the easy magnetization axis parallel to the surface. In a magnetic field with a strength above the critical value, new types of the nonlinear dynamic transformation of the domain walls were found in films with various thicknesses. © *2001 MAIK "Nauka/Interperiodica".*

As is known, magnetic films with the easy axis parallel to the surface exhibit the formation of asymmetric Bloch domain walls with a vortex internal structure within a certain interval of film thicknesses (for permalloy films, $b \in 0.05$–0.20 μm) [1]. The nonlinear dynamics of these domain walls was originally studied by Yuan and Bertram [2]. It was established that the moving wall structure exhibits transformations when the films are exposed to the magnetic fields with a strength above the critical level H_c. According to the rearrangement scenario described in [2], the initial asymmetric Bloch wall transforms into an asymmetric Néel wall and vice versa, with the corresponding change in the wall chirality.

Upon studying the nonlinear wall dynamics in magnetic films of various thicknesses exposed to the fields with a strength H close to H_c [$(H - H_c)/H_c \ll 1$], we have established new possible scenarios of the nonlinear wall transformations. Below, we describe these types of wall transformations and their genesis.

We have studied magnetic films of the permalloy type with a saturation magnetization of $M_s = 0.08$ Wb/m^2, anisotropy constant $K = 10^2$ J/m^3, and exchange parameter $A = 10^{-11}$ J/m. In the interval of film thicknesses from 0.05 to 0.15 μm, the system exhibits a usual [1] equilibrium asymmetric Bloch wall (Fig. 1a) separating two domains magnetized along the film surface in the z axis directions. On the central dashed line, the Mz changes sign. Between two other equilevel lines Mz = const, the **M** vector rotates by 60°. The temporal evolution of the wall structure upon switching the field **H** directed along the $\pm z$ axis was described by numerically solving the Landau–Lifshits equation written in the following form:

$$\frac{\partial \mathbf{M}}{\partial t} = -|\gamma|[\mathbf{M}, \mathbf{H}_{\text{eff}}] - |\gamma|(\alpha/M_s^2)[\mathbf{M}, [\mathbf{M}, \mathbf{H}_{\text{eff}}]], \quad (1)$$

where

$$\mathbf{H}_{\text{eff}} = (2A/M_s^2)\Delta\mathbf{M} + (2K/M_s^2)(\mathbf{Mc})\mathbf{c} + \mathbf{H}^{(m)} + \mathbf{H}, \quad (2)$$

t is the current time, γ is the gyromagnetic ratio, α is the damping parameter (in our calculations, $\alpha = 0.1$), $\mathbf{H}^{(m)}$ is the magnetostatic field, Δ is the Laplace operator in the xy plane, and **c** is the unit vector in the z axis. The method used for numerically solving Eq. (1) is described in [2–4].

The results of the numerical calculations gave instantaneous configurations of the magnetization **M**. Figure 1 shows a sequence of such patterns illustrating one of the new mechanisms of the nonlinear dynamic transformation of the domain walls.

In the first stage, an intrawall vortex shifts toward the bottom film surface (Fig. 1b) as in the classical case described in [2]. Then (in contrast to [2] where the first stage is followed by the formation of an asymmetric Néel wall) another vortex appears at the top surface on the same side of the central line; the second vortex has a chirality inverse to that of the first vortex, and eventually the wall acquires a structure depicted in Fig. 1c. Both vortices move downward and the first vortex disappears, while the second keeps moving to bring the situation depicted in Fig. 1d. This configuration, differing only by the chirality from the pattern presented in Fig. 1a, completes the first half-period of the wall transformation. The second half-period is generally repeats the first one and leads eventually to the wall structure fully identical (including the chirality type) to that presented in Fig. 1a.

This scenario takes place in the films with $b \in 0.065$–0.080 μm. In thicker films ($b > 0.080$ μm), we have observed another possible type of the dynamic transformation of the wall structure. In this case, the vortex also shifts toward the bottom film surface to

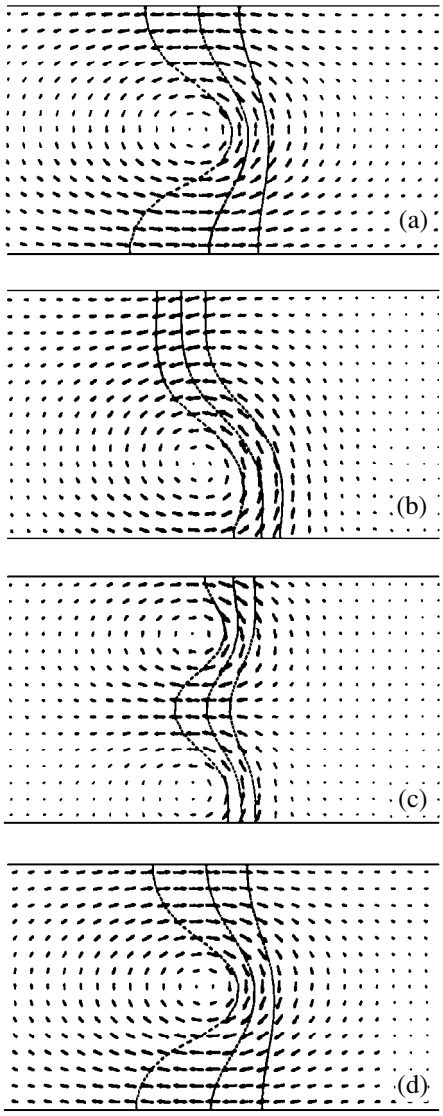

Fig. 1. A sequence of instantaneous domain wall configurations in a film with the thickness 0.07 μm.

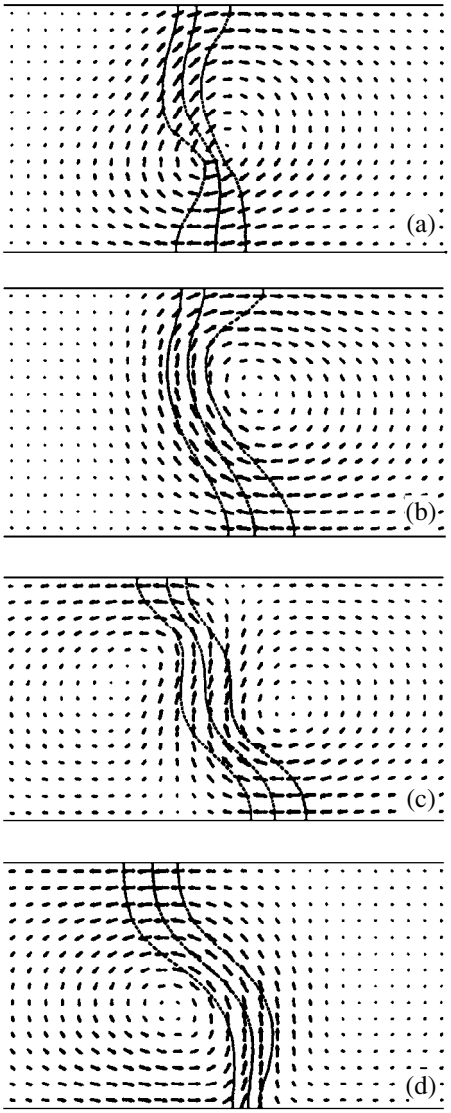

Fig. 2. A sequence of instantaneous domain wall configurations in a film with the thickness 0.10 μm.

yield a structure analogous to that depicted in Fig. 1b. Consider this as the initial configuration. Then the vortex strongly deforms and penetrates (as if tunneling) left to right through the central wall line (Figs. 2a and 2b). The vortex appearing on the right side moves downward. At the same time, a new vortex with the opposite chirality arises at the top surface and we observe an asymmetric structure with two vortices (Fig. 2c). Then both vortices move downward and the right-hand one disappears (Fig. 2d). The remaining vortex keeps moving downward and the system arrives at a configuration analogous to the initial one but with the opposite chirality. The second period repeats the first and eventually the wall structure and vortex chirality return to the initial state.

The results of our calculations showed that the main reason for the above dynamic wall transformations was a significant decrease in the magnetostatic fields caused by the pole scattering on the side wall surface. This factor facilitates precession of the **M** vector about the easy axis, which always arises in the fields $H \geq H_c$ [5]. In order to explain this, let us recall the wall transformation scenario described in [2], where the vortex shifting to the bottom surface transformed the wall from the asymmetric Bloch to the asymmetric Néel type, after which the wall converted into a nearly classical Néel wall. The one-dimensional Néel wall implies large magnetostatic field strengths. In the new wall transformation scenarios described above, the stage of the one-dimensional Néel wall formation is missing. Instead, the stages depicted in Figs. 1b and 2a appear, in which the magnetization **M** distribution in the wall plane is such that favors the pole scattering.

Thus, the nonlinear domain wall dynamics is highly sensitive to variations in the film parameters. The results of this analysis indicate that we may expect a nonmonotonic dependence of the bifurcation field strength H_c on the film thickness.

Acknowledgments. This study was partly supported by the Russian Foundation for Basic Research, project no. 99-02-16279.

REFERENCES

1. A. E. LaBonte, J. Appl. Phys. **40**, 2450 (1969).
2. S. V. Yuan and H. N. Bertram, Phys. Rev. B **44**, 12395 (1991).
3. B. N. Filippov and L. G. Korzunin, Fiz. Tverd. Tela (St. Petersburg) **38**, 2442 (1996) [Phys. Solid State **38**, 1343 (1996)].
4. B. N. Filippov and L. C. Korzunin, Phys. Rev. B (in press).
5. N. E. Schryer and L. B. Walker, J. Appl. Phys. **45**, 5406 (1974).

Translated by P. Pozdeev

Technical Physics Letters, Vol. 27, No. 5, 2001, pp. 370–372. Translated from Pis'ma v Zhurnal Tekhnicheskoĭ Fiziki, Vol. 27, No. 9, 2001, pp. 41–46.

Numerical Modeling of the Electrohydrodynamic and Thermal Instability of a Conducting Liquid Surface in a Strong Electric Field

S. A. Barengol'ts, E. A. Litvinov, V. G. Suvorov, and I. V. Uĭmanov

Institute of Electrophysics, Ural Division, Russian Academy of Sciences, Yekaterinburg, Russia

e-mail: suvorov@etel.ru

Received November 28, 2000

Abstract—The electrohydrodynamic and thermal instability development on a conducting liquid surface exposed to a strong electric field was studied by methods of two-dimensional numerical modeling. The Navier–Stokes equation was solved and the surface cone heating by the field emission current was described. It is demonstrated that the free surface evolution in this system leads to an avalanche-like growth in the cone tip temperature and the resulting explosion-like field electron emission. A considerable contribution to the liquid heating is due to a surface energy source (the Nottingham effect). The proposed computational method, based on the domain transformation to a canonical form, can be used to develop dynamic models of the liquid-metal ion source operation and to analyze the interaction of a gas plasma with a liquid metal surface in the cathode spot of a vacuum arc. © *2001 MAIK "Nauka/Interperiodica".*

The behavior of a conducting liquid surface exposed to a strong electric field plays a considerable role in many physical phenomena, such as the formation of field emission centers, ectons [1], and cathode spots in a vacuum arc, the development of oscillations and current interruptions in liquid-metal ion sources [2], etc. Modeling these phenomena usually requires simultaneously solving several mutually related problems and involving calculations of the free liquid surface dynamics, the surface electric field (with an allowance for the charged particle emission), and the liquid heating by the current and surface heat sources. A special feature of these problems is the strong feedback between the surface shape and pressure (including both the electrostatic pressure and surface tension). This circumstance hinders effective application of the traditional mark-and-cell (MAC) method to modeling the electrohydrodynamic phenomena in the systems indicated above and stimulates the search for and testing of more convenient approaches. In the context of the general problem of describing evolution of a liquid metal surface exposed to an electric field, an interesting analytical approach was developed by Zubarev [3, 4].

Recently [5, 6], the flow of a conducting liquid surface in an electric field was successfully calculated by the method of domain transformation to a canonical form [7]. Below, we describe a generalization of this method taking into account heating of the surface cone by the field emission current. This implies that, simultaneously with calculating the liquid motion, we will use the same computational procedure to solve the two-dimensional thermal conductivity problem.

The problem geometry possessing an axial symmetry (z axis) is depicted in Fig. 1. In the first stage, we modeled the evolution of a small perturbation on the surface of liquid gallium in the electric field with a strength slightly above the critical value (Fig. 2). The method of calculation is described in detail elsewhere [6]. Beginning with a time instant when the field strength at the cone apex reaches a value sufficient to cause the field emission (~6 V/nm), the electrohydrodynamic calculations are supplemented with solving the equation of thermal conductivity in the moving liquid:

$$\begin{aligned} C\frac{\partial T}{\partial t} + (\mathbf{c}\nabla T) &= \chi\Delta T + \sigma^{-1}j^2; \\ \left.\frac{\partial T}{\partial r}\right|_{r=0,\, r=a} &= 0; \quad \chi\left.\frac{\partial T}{\partial n}\right|_{z=\eta(r)} = Q_N; \\ \left.\frac{\partial T}{\partial z}\right|_{z=-b} &= 0; \quad T(r, t=0) = T_0, \end{aligned} \tag{1}$$

where C is the specific heat capacity, T is the temperature, $\mathbf{c} = (u, v)$ is the velocity field, χ is the thermal conductivity, σ is the electric conductivity, and j is the electric current density in the liquid. This equation describes heating of a moving liquid by the field emission current. The heat is supplied from two sources represented by the terms $\sigma^{-1}j^2$ (the volume Joule effect) and Q_N (the surface Nottingham effect [8] considered as the boundary condition). In order to determine the thermophysical characteristics of the cathode (C, χ, σ) as functions of the temperature, we used the tabulated data [9]. It was assumed that the surface tension coefficient is independent of the temperature. The field emis-

sion current density and the Nottingham heat flux on the surface were calculated using the generalized Murphy–Hood approximation (extended to the high-temperature region) [10].

The current density distribution inside the cathode (descried with neglect of the Thompson effect) is determined by the relationship $\mathbf{j} = -\sigma\nabla\varphi$, where φ is the potential in the region under consideration. Using the condition of continuity for the current density ($\nabla\mathbf{j} = 0$), we obtain

$$\nabla[\sigma(T)\nabla\varphi] = 0. \quad (2)$$

The boundary condition on the free liquid surface (**n** is the normal to this surface) is

$$\sigma(T)\left.\frac{\partial\varphi}{\partial n}\right|_{z=\eta} = j_{em}(T, E)\big|_{z=\eta}. \quad (3)$$

The other domain boundaries obey the simplest conditions:

$$\left.\frac{\partial\varphi}{\partial r}\right|_{r=0,\, r=a} = 0; \quad \varphi|_{z=-b} = 0. \quad (4)$$

According to the method adopted, the contour of the domain is transformed by changing the variables

$$r = r, \quad \xi(r, t) = \frac{z + B}{\eta(r, t) + B} \quad (5)$$

into a new rectangular domain ($r = 0$, $r = a$, $\xi = 0$, $\xi = 1$) in the (r, ξ) plane. The set of Eqs. (1)–(4) is written, together with the Navier–Stokes equations, in the variables (r, ξ) and solved by the traditional MAC method on a staggered grid [7], with the pressure, temperature, and electric potential inside the liquid determined at the same points of the grid.

Glazanov *et al.* [11] solved the problem (1)–(4) in a two-dimensional case for a solid-state "stationary" emitter heated by the field emission current. It was demonstrated that, depending on the initial current density, the system either features a regime of current and temperature stabilization or exhibits a thermal instability development (whereby the emission current and emitter temperature increase in an avalanche-like manner with time). In the latter case, the Nottingham effect results in that a maximum temperature is achieved inside the emitter.

The electrohydrodynamic instability development leads to a continuous decrease in the cone apex radius and the surface field strength at this point [5, 6], which accounts for the avalanche-like temperature growth (Fig. 3). At a time instant corresponding to a tenfold increase in the temperature, the cone apex curvature radius is 3 nm, the maximum current density is 2.5×10^{13} A/m^2, and the total current from the surface is 15 mA. The experimental thermal instability development (followed by the explosion-like electron emission) was most thoroughly studied in [12], where a crit-

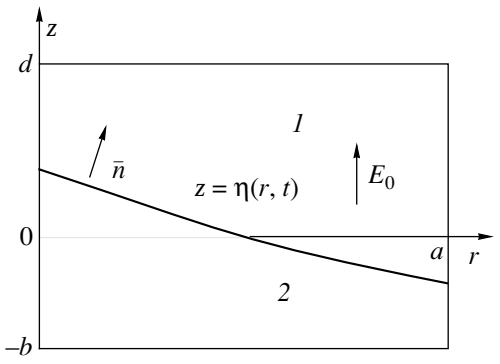

Fig. 1. A schematic diagram of the problem geometry: (*1*) vacuum; (*2*) liquid metal.

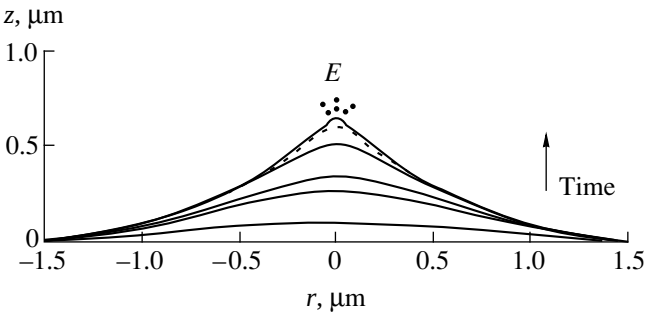

Fig. 2. The results of model calculations showing evolution of the liquid gallium surface profile in an external electric field ($E_0 = 4.8 \times 10^8$ V/m) at various sequential time instants (ns): 0 (abscissa axis), 92.9, 104.5, 116.8, 120.2, and 120.4. Dashed profile corresponds to the time instant after which the thermal problem is solved simultaneously with the Navier–Stokes problem (*E* is the explosion-like electron emission).

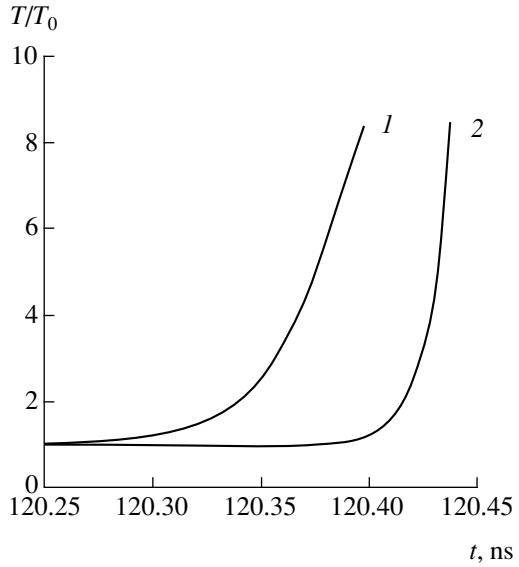

Fig. 3. Dynamics of the relative temperature variation calculated (*1*) with and (*2*) without an allowance for the Nottingham effect.

ical current for the explosion-like electron emission was evaluated at 30 mA.

The relationship between the surface temperature and the electric field strength at this surface during the cone apex evolution is such that the surface energy source (Nottingham effect) is always positive (i.e., heats the surface). This circumstance presents essential difference from the case of solid emitter heating, when the Nottingham effect changes the sign from positive (in the initial heating stage) to negative (whereby the point of maximum temperature shifts inward the cathode). Figure 3 shows comparative data on the dynamics of temperature variation calculated with (curve *1*) and without (curve *2*) an allowance for the Nottingham effect. As seen, the thermal instability in the latter case develops more rapidly.

In concluding, it should be noted that the approach described above can be further generalized to apply to the analysis of effects accompanying the interaction of a plasma with a liquid metal surface in the cathode spot of a vacuum arc.

Acknowledgments. The work was supported by the Russian Foundation for Basic Research (RFBR) (project nos. 99-02-18234 and 00-02-17428) and by the joint INTAS–RFBR program (project no. IR-97-663).

REFERENCES

1. G. A. Mesyats, *Ectons in Vacuum Discharge: Breakdown, Spark, Arc* (Nauka, Moscow, 2000).
2. G. L. R. Mair, J. Phys. D **21**, 1654 (1988).
3. N. M. Zubarev, Zh. Éksp. Teor. Fiz. **114**, 2043 (1998) [JETP **87**, 1110 (1998)].
4. N. M. Zubarev, Zh. Éksp. Teor. Fiz. **116**, 1990 (1999) [JETP **89**, 1078 (1999)].
5. V. G. Suvorov, Pis'ma Zh. Tekh. Fiz. **26** (1), 66 (2000) [Tech. Phys. Lett. **26**, 33 (2000)].
6. V. G. Suvorov and E. A. Litvinov, J. Phys. D **33**, 1245 (2000).
7. O. M. Belotserkovskiĭ, V. A. Gushchin, and V. M. Kon'shchin, Zh. Vychisl. Mat. Mat. Fiz. **27**, 594 (1987).
8. W. B. Nottingham, Phys. Rev. **59** (11), 907 (1941).
9. V. E. Zinov'ev, *Thermophysical Properties of Metals at High Temperatures* (Metallurgiya, Moscow, 1989).
10. E. A. Litvinov, G. A. Mesyats, and D. I. Proskurovskiĭ, Usp. Fiz. Nauk **139** (2), 265 (1983) [Sov. Phys. Usp. **26**, 138 (1983)].
11. D. V. Glazanov, L. M. Baskin, and G. N. Furseĭ, Zh. Tekh. Fiz. **59** (5), 60 (1989) [Sov. Phys. Tech. Phys. **34**, 534 (1989)].
12. L. W. Swanson and G. A. Schwind, J. Appl. Phys. **49**, 5655 (1987).

Translated by P. Pozdeev

Technical Physics Letters, Vol. 27, No. 5, 2001, pp. 373–377. Translated from Pis'ma v Zhurnal Tekhnicheskoĭ Fiziki, Vol. 27, No. 9, 2001, pp. 47–56.

Diffusive Decay of a Low-Pressure Electronegative Plasma

E. A. Bogdanov*, A. A. Kudryavtsev*, and L. D. Tsendin**

** St. Petersburg State University, St. Petersburg, Russia*

e-mail: akud@ak2138.spb.edu

*** St. Petersburg State Technical University, St. Petersburg, Russia*

Received December 8, 2000

Abstract—The diffusion decay of a pulsed low-pressure discharge plasma in an electronegative gas is theoretically studied assuming the absence of plasmachemical processes. According to the previously established mechanisms, evolution of the plasma parameters involves two stages in which the variation of both density and energy of electrons is controlled by the transport processes. In the first stage, the flux of negative ions to the wall is absent and the electron density decays sharply with time, whereby almost all electrons escape within a finite time from the discharge volume where an ion–ion (electron-free) plasma is formed. In the second stage, this plasma decays by an ion–ion ambipolar diffusion mechanism. © *2001 MAIK "Nauka/Interperiodica".*

The presence of negative ions in a discharge significantly affects the transport processes for various plasma components. Under stationary conditions, a considerable growth in the electron temperature ($T_e \gg T$) leads to the plasma separation phenomenon, whereby an ion–ion plasma in formed in the central discharge region and an electron–ion plasma, at the periphery [1, 2]. In turn, the formation of these spatial discharge zones gives rise to two stages in the diffusion decay: electron–ion (first) and ion–ion (second) [1, 2]. A sharp change in the plasma afterglow mode, which agrees with this pattern, was experimentally observed long ago [3, 4] under conditions where the initially small density of negative ions n_n increased in the first stage by the attachment mechanism.

Gutsev *et al.* [5] demonstrated that a transition to the ion–ion plasma has a sharp character, whereby almost all electrons escape from the discharge volume within a finite time t_0 determined primarily by the initial density ratio n_n/n_e. The subsequent analysis [6, 7] of the spatial and temporal evolution of the afterglow plasma density with neglect of the electron temperature variation (i.e., assuming $T_e(t) = \text{const}$) confirmed the main conclusions made in [5] concerning the two limiting cases of small and large T_e values. Under real conditions, we must take into account that $T_e(t)$ unavoidably varies in the afterglow stage because the balance of charged particle densities and the electron energy balance are closely interrelated and the ambipolar field strongly affecting the diffusion of charged particles is determined by T_e as well.

Consider a plane-parallel geometry with cold absorbing walls situated at $x = \pm L$. After switching off the discharge, the system of equations describing plasma in this system has the following form [6, 7]:

$$\partial n_j/\partial t = -\Gamma_j' = (D_j n_j' \pm b_j n_j E)', \qquad (1)$$

where primes denote the derivatives with respect to coordinate (d/dx); indices $j = e, n, p$ refer to electrons, negative ions, and positive ions, respectively; and D and b are the diffusion coefficients and mobilities of the plasma components, respectively. In the diffusion regime under consideration, Eqs. (1) are supplemented by the zero boundary conditions for particle densities at the walls and for the density gradients at the center. When the conditions $n_j(L, t) = 0$ led to negative values of $\Gamma_n(L, t)$ (which implies a total flux directed outward from the wall), the boundary conditions were taken in the form $\Gamma_j(L, t) = C_0 n_j(L, t)$; $j = e, n, p$; $C_0 \gg 1$ (for detail, see [6, 7]).

A self-consistent (ambipolar) field has the following form:

$$E = (D_p n_p' - D_n n_n' - D_e n_e')/(b_p n_p + b_n n_n + b_e n_e). \quad (2)$$

In a stationary low-pressure discharge plasma, the central region ($x \le x_0$) is characterized by the Boltzmann distributions for both electrons and ions [1, 2]. For this reason, the initial conditions for $x < x_0$ were set by a parabolic profile for $n_n(x, 0)$ and by a flat profile for $n_e(x, 0)$. In the outer region ($x > x_0$), where the negative ions are absent, the initial profiles are $n_p(x, 0) \sim n_e(x, 0) \sim \sin[\sqrt{z + \alpha}\,(L - x)]$, where z and α are the frequencies of ionization and attachment in units of the characteristic diffusion time f the negative ions $\tau_n = L^2/D_n$ [1, 2].

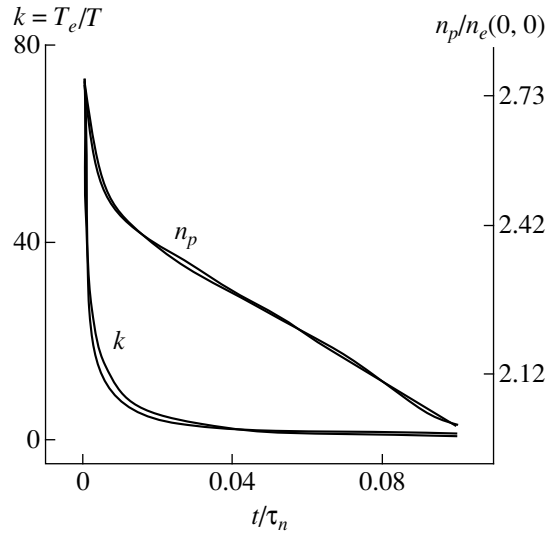

Fig. 1. Evolution of $k = T_e/T$ and $\bar{n}_p/n_e(0, 0)$ (for $b_p/b_n = 1/\sqrt{2}$ and $b_e/b_p = 250$) with time according to the results of numerical calculations and approximated formulas (7)–(11).

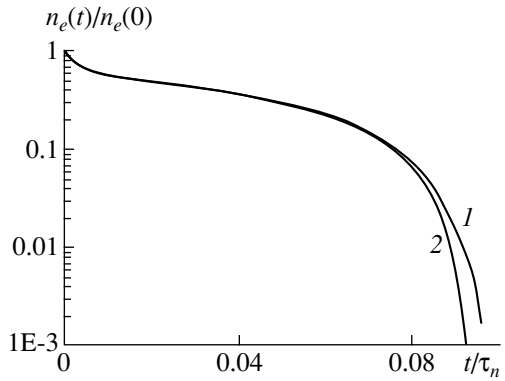

Fig. 2. Time variation of $\bar{n}_e$ (for $b_p/b_n = 1/\sqrt{2}$ and $b_e/b_p = 250$): (*1*) according to approximated formulas (10) and (11); (*2*) according to the results of numerical calculations.

For a purely diffusion decay, when the transport processes dominate over the bulk chemical reactions, the main factor responsible for the electron cooling is the diffusion cooling [2]. In this case, $T_e(x)$ = const (because thermal conductivity is fast) and the electron energy balance is described by the equation

$$(3/2)\bar{n}_e dT_e/dt = -e\varphi_w\Gamma_e(L, t) - \delta_\varepsilon\nu_\varepsilon\bar{n}_e(T_e - T) + \bar{n}_e\varepsilon_h\nu_h. \quad (3)$$

Here, the first term $e\varphi_w = e\varphi_a + e\varphi_h$ is the wall potential relative to the center equal to a sum of the ambipolar potential drop and the wall jump, which usually amounts to several T_e ($e\varphi_w = C_1T_e$). For the Maxwell electron distribution function (EDF), $e\varphi_a \approx T_e\ln(\Lambda/\lambda_i)$ and $e\varphi_h \approx T_e\ln(\sqrt{M/m})$ [2]. When the electron escaping from the central region strongly distorts the fast part of EDF, the $e\varphi_w$ value decreases as compared to that calculated for the Maxwell EDF [8]. In order to take this effect into account without detailed analysis of the EDF formation, we may vary the coefficient from minimum $C_1 = 2$ ($e\varphi_h \sim T_e$) [8] to maximum $C_1 = 5$ ($e\varphi_h \sim T_e\ln(\sqrt{M/m})$). The second term in the right-hand part of Eq. (3) describes the energy exchange between electrons and neutrals, ν_ε and δ_ε being the corresponding frequency and energy factor. The third term reflects the electron heating upon collisions with the effective frequency ν_h, whereby the electrons acquire the energy ε_h (superelastic collisions, detachment, etc.).

Figures 1–4 present the results of jointly solving Eqs. (1)–(3), which confirm the previous conclusions [5–7]. The plots are constructed using a dimensionless coordinate (in L units) and dimensionless time (in $\tau_n = L^2/D_n$ units). As is seen from these data, both spatial and temporal evolution of the density of charged particles exhibits two stages (Figs. 1 and 2). In the first stage, corresponding to the electron–ion decay ($t < t_0$), the plasma loses electrons and positive ions, so that the particle density profile variation proceeds at a virtually constant density of negative ions. Therefore, the cross-section-averaged densities $\bar{n}_j(t)$ ($j = e, n, p$) obey two important relationships [5]:

$$\bar{n}_n(t) = \text{const} = \bar{n}_n(0), \quad (4)$$

which implies that

$$\bar{n}_p(t) - \bar{n}_p(0) = \bar{n}_e(t) - \bar{n}_e(0).$$

A typical curve of $T_e(t)$ shows a region of sharp decay at small times ($t < t_1$) and a region of slowly attaining a quasistationary T_{es} level

$$T_{es} = T + 2\varepsilon_h\nu_h/3\delta_\varepsilon\nu_\varepsilon. \quad (5)$$

This behavior of $T_e(t)$ results in that the plots of both $\bar{n}_p(t)$ and $\bar{n}_e(t)$ in the first plasma decay stage can be separated into two regions. In the region corresponding to the sharp drop in $T_e(t)$, where the first right-hand term dominates in Eq. (3), expressions (1) and (3) yield the following approximate relationship:

$$C_1 d\bar{n}_e/dt = dT_e/dt. \quad (6)$$

In this case, the $T_e(t)$ variation is well approximated by the function

$$T_e(t) = (T_{e0} - T_{es})[\bar{n}_e(t)/\bar{n}_e(0)]^{C_1} + T_{es}. \quad (7)$$

As was demonstrated in [2, 3] for large values of the parameter $k = T_e/T$, the $n_e(x)$ profiles in the central region ($x \le x_0(t)$) are virtually flat. As a result, the decay

of $\bar{n}_e(t)$ for $t < t_1$ (such that $k(t_1) \approx 5$) is well described by the formula

$$d\bar{n}_e/dt = -16\bar{n}_e/(\pi^2\tau_{ap}), \quad (8)$$

where $\tau_{ap} = 4L^2/(\pi^2 D_p(k+1))$ is a characteristic time of the usual electron–ion ambipolar diffusion.

Finally, Eqs. (6)–(8) yield the following relationships valid for $t < t_1$ (such that $k(t_1) \approx 5$):

$$k(t) = k_0/[(1 + 4C_1 b_p(k_0 + 1)t], \quad (9)$$

$$\bar{n}_e(t) = \bar{n}_{e0}/[(1 + 4C_1 b_p(k_0 + 1)t]^{1/C_1},$$
$$\bar{n}_p(t) = \bar{n}_n(0) + n_{e0}/[(1 + 4C_1 b_p(k_0 + 1)t]^{1/C_1}. \quad (10)$$

Dependence of the plasma parameters on the wall potential is well illustrated by Eqs. (9) and (10); the results of calculations considered below were obtained for a typical value f $C_1 = 4$.

In the second portion of the first decay stage, where $t > t_1$ and T_e is close to T_{es}, both spatial and temporal evolution of the ion density are determined by their relative mobilities. As was demonstrated in [6, 7], the effective diffusion coefficient of positive ions $D_p^{\text{eff}}(x) = -\Gamma_p(x)/\partial n_p/\partial x$ in region 0 is close to the ion–ion ambipolar diffusion coefficient $D_n = 2D_pD_n/(D_p + D_n)$, and in region 1, to the electron–ion ambipolar diffusion coefficient $D_{ap} = D_p(1 + k)$ (see Fig. 3; for more detail, see [2, 3]). For $b_n > b_p$ and $k \sim 1$, $D_p^{\text{eff}}(x)$ becomes virtually constant over the cross section and is approximately equal to D_{ii} (Fig. 3). Therefore, $\bar{n}_p$ in the second region ($t > t_1$) decays with a characteristic time of the ion–ion diffusion τ_{ii}:

$$\bar{n}_p(t) = \bar{n}_p(t_1)\exp(-t/\tau_{ii}), \quad (11)$$

where $\tau_{ii} = 4L^2/\pi^2 D_{ii}$.

It should be emphasized that the self-consistent field in the central region ($x < x_0$) is determined by the ion–ion ambipolar diffusion, while the existing Boltzmann electron equilibrium always "adjusts" to this field by forming the corresponding electron density profiles [2, 3]. For the positive ions possessing a higher mobility ($b_p > b_n$), the ion–ion ambipolar field in region 0 is directed inward, that is, oppositely to the electron–ion ambipolar field in region 1 (always directed outward). The field accelerating negative ions in region 0 would accelerate electrons as well. Electrons (possessing a higher mobility in the plasma) must always be "held"; for $b_p > b_n$, this leads to an interesting phenomenon of nonmonotonic field strength and electron density $n_e(x)$ profiles in the afterglow stage. The latter density increases in region 0 and decreases near walls in region 1 (see Fig. 4; for more detail, see [2, 3]).

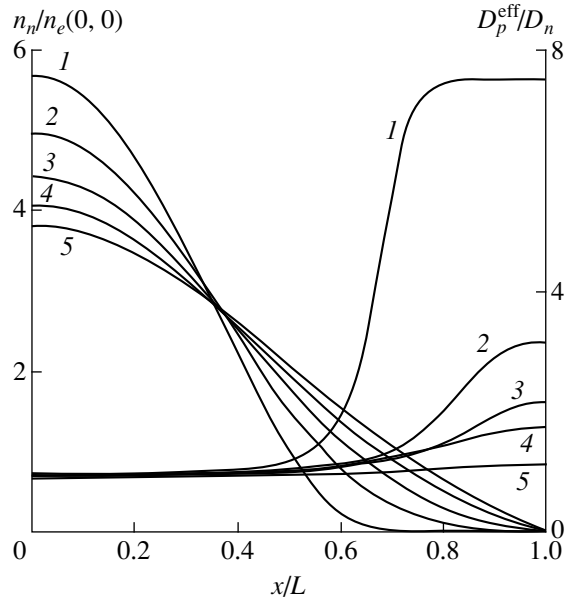

Fig. 3. Spatial profiles of $n_n(x)$ and $D_p^{\text{eff}} = -\Gamma_p/(\partial n_p/\partial x)$ (for $b_p/b_n = 1/\sqrt{2}$ and $b_e/b_p = 250$). Curves *1*–*5* correspond to time instants from $t = 0.01\tau_n$ to $t = 0.09\tau_n$ at a step of $0.02\tau_n$ ($n_n(L) = 0$ in all cases).

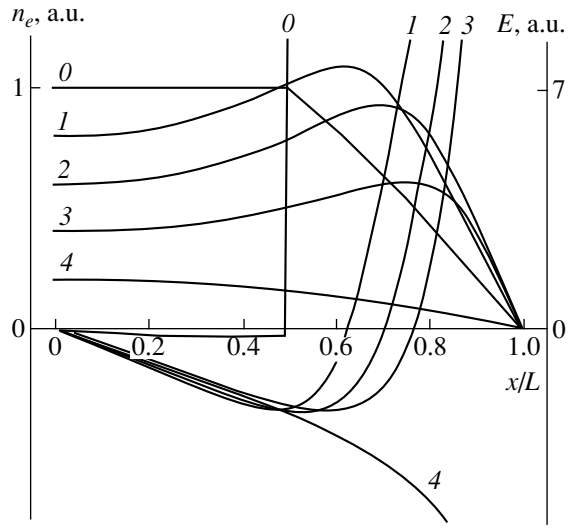

Fig. 4. Spatial profiles of $\bar{n}_e$ the electric field strength E (for $b_p/b_n = 5$ and $b_e/b_n = 250$). Curves *0*–*4* correspond to time instants from $t = 0$ to $t = 0.025\tau_n$ at a step of $0.0625\tau_n$ ($n_e(L) = 0$ in all cases). The scale in ordinate axis for $n_e(x)$ is distorted so as to reveal the profile structure.

The $n_e(x)$ profiles retain their initial trapezoidal shape for a long time and relationship (8) is valid up to

$k(t) \approx 2$. Even when $k(t)$ drops down to such low values, the coefficient D_p^{eff} (in contrast to the case of $b_n > b_p$) does not become uniform in the cross section: $D_p^{\text{eff}}(0, t) \sim 2b_nT < 2b_pT \sim D_p^{\text{eff}}(1, t)$. For this reason, relationship (11) is not as adequate to the real situation for $b_p > b_n$ and $t_1 < t < t_0$. Since $\bar{n}_n(t) = \text{const} = \bar{n}_n(0)$ and $\bar{n}_p(t)$ drops, their difference $\bar{n}_e(t) = \bar{n}_p(t) - \bar{n}_n(0)$ becomes sharper with time [5]. At $t = t_0$, when $\bar{n}_p(t_0) \approx \bar{n}_n(0)$, the electron density exhibits a sharp drop and only positive and negative ions are retained in the volume. As noted in [5], the escape of electrons from the volume for $\bar{n}_n(0)/\bar{n}_e(0) > 1$ is accompanied by a relatively small change in the ion densities ($t_0 = \tau_p \ln[\bar{n}_p(0)/\bar{n}_n(0)]$).

A physical reason for the sharp decay in the electron density with time is related to the fact [5] that negative ions in the first stage are confined in the volume and their flux to the wall is zero. The equality of positive and negative particle fluxes to the boundaries is provided by electrons and positive ions, which implies the relationship

$$\bar{n}_p/\tau_p = \bar{n}_e/\tau_e, \tag{12}$$

where τ_p and τ_e are the characteristic diffusion times of positive ions and electrons, respectively. Since $\bar{n}_p = \bar{n}_n + \bar{n}_e$ is always greater than $\bar{n}_e$, relationship (12) leads to inequality $\tau_p > \tau_e$, which implies a relatively faster escape of electrons compared to ions. The smaller the $\bar{n}_e$ value relative to $\bar{n}_p$, the higher the escape rate of electrons to the wall. As a result, the process sharpens with time and proceeds faster than exponential. This behavior is typical of a regime with strong positive feedback [9]. An analysis performed in [9] showed that such regimes frequently give rise to a wave propagating at a constant velocity. In application to a plasma with negative ions, this concept was developed in [10].

The results of calculations using relationships (9)–(11) agree well with the rigorous solution to system (1)–(3) (Figs. 1 and 2). In the second stage ($t > t_0$), the decay of the ion–ion (electron-free) plasma with $n_p(x, t) = n_n(x, t)$ is determined by the ion–ion ambipolar diffusion as described by Eq. (11). Initially, the major diffusion mode is established during the time $\sim\tau_{ii}$ and then the decay proceeds according to the usual law in this mode [6, 7].

In concluding, it should be noted that, since the electron escape sharpening is the most rapid process of the purely diffusion decay, the pattern will remain qualitatively the same if electrons would exhibit an additional bulk loss by attachment. In the simplest variant, a solution to the initial system (with ν_a being the attachment frequency) [11]

$$d\bar{n}_p/dt = -\bar{n}_p/\tau_p, \quad d\bar{n}_n/dt = \nu_a\bar{n}_e \tag{13}$$

has the following form:

$$\begin{aligned} \bar{n}_p(t) &= \bar{n}_p(0)\exp(-t/\tau_p), \\ \bar{n}_e(t) &= \bar{n}_p(t)/(1-a) \\ &- [(\bar{n}_n(0) - a\bar{n}_e(0))\exp(-\nu_a t)]/(1-a). \end{aligned} \tag{14}$$

Depending on the value of the parameter $a = \nu_a\tau_p$, the characteristic sharpening time (for $\bar{n}_e(t_0) = 0$) is $t_0 = \tau_p \ln[\bar{n}_p(0)/\bar{n}_n(0)]$ in the absence of attachment ($a = 0$ [5]) and $t_0 = (\tau_p \ln a)/(a - 1)$ (for $\bar{n}_n(0) = 0$) in experiments on the attachment probability determination [11].

Thus, we have analyzed the diffusion decay of a pulsed low-pressure discharge plasma in an electronegative gas with a self-consistent balance of particle densities and electron energies. The pattern of the temporal evolution of the charged particle density profiles confirms the previously developed model [5–7], showing a sharper decay of the electron density in the first stage, leading to the formation of ion–ion (electron-free) plasma decaying in the second stage. Taking into account the attachment probability does not qualitatively change the physical pattern, only decreasing the first stage duration t_0. At the same time, the process of detachment may dramatically alter this scenario [12, 13] and lead to another limiting case whereby the system asymptotically evolve to a usual electron–ion (negative-ion-free) plasma. Therefore, the description of plasma decay with an allowance of detachment requires separate special analysis.

Acknowledgments. This study was supported by the Russian Foundation for Basic Research, project nos. 98-02-17778 and 98-02-16000.

REFERENCES

1. L. D. Tsendin, Zh. Tekh. Fiz. **55** (12), 2318 (1985) [Sov. Phys. Tech. Phys. **30**, 1377 (1985)]; Zh. Tekh. Fiz. **59** (1), 21 (1989) [Sov. Phys. Tech. Phys. **34**, 11 (1989)].
2. A. Rozhansky and L. Tsendin, *Transport Processes in Partially Ionized Plasmas* (Énergoatomizdat, Moscow, 1988; Gordon and Breach, New York, 2001).
3. L. J. Puckett, M. D. Kregel, and M. W. Teague, Phys. Rev. A **4** (4), 1659 (1971).
4. D. Smith, A. G. Dean, and N. G. Adams, J. Phys. D **7**, 1944 (1974).
5. S. A. Gutsev, A. A. Kudryavtsev, and V. A. Romanenko, Zh. Tekh. Fiz. **65** (11), 77 (1995) [Tech. Phys. **40**, 1131 (1995)].
6. E. A. Bogdanov, A. A. Kudryavtsev, and L. D. Tsendin, in *Contributed Papers of the 3rd International Conference "Plasma Physics and Plasma Technology PPPT-3," Minsk, 2000*, Vol. 1, p. 118.

7. E. A. Bogdanov, A. A. Kudryavtsev, and L. D. Tsendin, Zh. Tekh. Fiz. **71** (4), 40 (2001) [Tech. Phys. **46**, 404 (2001)].
8. A. P. Zhilinskiĭ, I. F. Liventsova, and L. D. Tsendin, Zh. Tekh. Fiz. **47**, 304 (1977) [Sov. Phys. Tech. Phys. **22**, 177 (1977)].
9. *Sharpening Modes. Evolution of Idea*, Ed. by I. M. Makarov (Nauka, Moscow, 1999); T. S. Akhromeeva, S. P. Kurdyumov, and G. G. Malinetskii, Phys. Rep. **76** (5/6), 179 (1989).
10. I. D. Kaganovich, D. Economou, B. Ramamurthi, and V. Midha, Phys. Rev. Lett. **84** (9), 1918 (2000).
11. A. A. Kudryavtsev, in *Proceedings of the Conference on Low Temperature Plasma Physics "Plasma: XXth Century," 1998* (Petrozavodskiĭ Univ., Petrozavodsk, 1998), Part 1, p. 618.
12. I. D. Kaganovich, B. N. Ramaputhri, and D. J. Economou, Appl. Phys. Lett. **76** (20), 2844 (2000).
13. A. A. Kudryavtsev, A. L. Kuranov, V. G. Mishakov, *et al.*, Zh. Tekh. Fiz. **71** (3), 29 (2001) [Tech. Phys. **46**, 299 (2001)].

Translated by P. Pozdeev

Technical Physics Letters, Vol. 27, No. 5, 2001, pp. 378–380. Translated from Pis'ma v Zhurnal Tekhnicheskoĭ Fiziki, Vol. 27, No. 9, 2001, pp. 57–63.

Vanadium Oxide Films with Improved Characteristics for IR Microbolometric Matrices

V. Yu. Zerov*, Yu. V. Kulikov*, V. G. Malyarov*, I. A. Khrebtov*, I. I. Shaganov, and E. B. Shadrin****

** Vavilov Optical Institute, State Scientific Center of the Russian Federation, St. Petersburg, 190164 Russia*

*** Ioffe Physicotechnical Institute, Russian Academy of Sciences, St. Petersburg, 194021 Russia*

Received November 13, 2000

Abstract—Vanadium oxide (VO_x) films intended for use in uncooled IR microbolometric matrices were deposited by reactive magnetron sputtering on silicon substrates. Optimum deposition conditions were determined, which provide for the obtaining of films possessing a current $1/f$ noise level 3–10 times lower, extended dynamic range, and increased working temperature interval. It was found that the $1/f$ noise level of the VO_x films depends on the VO_2 phase content and grain size. It is suggested that the observed $1/f$ noise is caused by the martensite transformation characteristic of the semiconductor–metal phase transition in VO_2. © *2001 MAIK "Nauka/Interperiodica".*

In the past years, considerable progress has been achieved in the development of IR imaging systems for various applications, based on uncooled microbolometric matrices (MBMs) [1, 2]. A thermosensitive layer in the planar detector elements of MBMs frequently represents a film of mixed vanadium oxides (VO_x). Thin (0.1–0.2 μm) VO_x films possess a room-temperature resistivity convenient for matching bolometers to the readout electronics and a temperature coefficient of resistance [3] ensuring a high sensitivity of these microbolometers (MBs).

As is known, the threshold sensitivity of MBs is limited by the thermal and Johnson's noises; moreover, the low-frequency sensitivity depends on the current $1/f$ noise of a thermosensitive layer, which is an additional noise component for the bolometer. Use of the VO_x films in MBMs poses certain requirements with respect to adhesion, surface homogeneity, and deposition temperature (below 500°C) to provide for the matching with planar readout electronic devices.

The purpose of this study was to determine optimum reactive magnetron sputtering conditions in order to obtain VO_x films with improved bolometric characteristics for use in uncooled MBMs.

We performed a series of deposition cycles on a Z-400 reactive magnetron sputtering system and obtained VO_x films on 350-μm-thick single crystal ⟨100⟩-oriented silicon wafers (KDB-10 grade) with a 0.25-μm-thick Si_3N_4 underlayer. Using experience gained in the previous experiments [3, 4], the deposition conditions were selected as follows: substrate temperature, 450°C; total pressure of an oxygen–argon mixture in the deposition chamber, 2.4 μbar; magnetron power, ~110 W; deposition time, 24 min. The working parameters variable within small limits were the partial oxygen pressure (around 0.12 μbar), magnetron voltage, and the sample cooling time. The sample films were deposited through replaceable copper–nickel masks so as to obtain separate VO_x-coated areas. This ensured a reduced level of mechanical stresses caused by a difference in the thermal linear expansion coefficients of the film and substrate.

The film samples were compared by measuring the temperature coefficient of resistance (TCR) and the room-temperature noise spectrum using a conventional four-point-probe technique. The working VO_x film area in the samples varied from 1.6×0.8 to 1.6×1.2 mm (the latter size refers to the distance between potentiometric contacts).

The sample resistance was measured in a temperature interval from 20 to 95°C. The measurements were conducted in both heating and cooling modes in order to determine the hysteresis related to a phase transition in vanadium dioxide (VO_2) entering into the film composition. An analysis of the hysteresis loop parameters provided information about the sample composition and structure perfection as well as of the possible working temperature interval of MBMs based on these films. The plots of resistance versus temperature for various samples are presented in Fig. 1.

The noise spectra were measured in a frequency range from 10 to 1000 Hz at various values of the bias current up to 250 μA (this is a typical interval of supply currents used in MBMs). The current noise component

1063-7850/01/2705-0378$21.00 © 2001 MAIK "Nauka/Interperiodica"

separated in all samples satisfactorily obeyed the empirical relationship

$$U_I^2 = K\frac{I^2R^2}{Vf^n}, \quad (1)$$

where U_I^2 is the mean square voltage of the current noise in the $\Delta f = 1$ Hz frequency band; K is the noise parameter characterizing each particular sample; I is the current passing through the sample; R and V are the resistance and volume of the working region of the film, respectively; and n is the frequency exponent. This expression differs from the well-known law [5] in that we use the parameter K instead of the Hooge's dimensionless parameter because no experimental data on the charge carrier concentrations were available.

The electrical and noise parameters of some samples are listed in the table.

When the partial oxygen pressure in the gas phase was varied only within 10–20%, the samples exhibited a large scatter in the ratio of resistances R_s/R_m corresponding to the low- and high-temperature merge points of the hysteresis loop (Fig. 1). This behavior was observed even in the samples showing no clearly pronounced phase transition and retaining semiconductor conductivity in the entire temperature interval studied, with only a slight inflection in the $R_\square(T)$ curve at 60°C (sample 26C). Among the variety of vanadium oxides, only VO_2 exhibits a structural transformation in the temperature interval studied; therefore, the absence of the semiconductor–metal transition was indicative of a very small content of VO_2 microdomains in these films. In contrast, the conductivity of sample 27C possessing a maximum value of the R_s/R_m ratio exhibited a metal character at temperatures above 80°C, in agreement with predominantly VO_2 composition of these films.

An analysis of the $R_\square(T)$ curves presented in Fig. 1 showed the following trends. The value of the room-temperature noise parameter K decreases together with the R_s/R_m ratio (i.e., with the VO_2 phase content), which is also illustrated by data in the table (cf. samples 27C, 24C, and 26C). On the other hand, the K value of sample 06C is smaller than that of sample 26C, although the former film contains a greater amount of VO_2 (judging by the R_s/R_m ratio). A comparative examination of the state of the sample surface with the aid of a scanning-electron microscope (SEM) showed that a lower noise level in this case was observed for the sample with smaller grain size (Fig. 2). Thus, the noise intensity in the films studied is determined by two principal parameters: vanadium dioxide content and grain size.

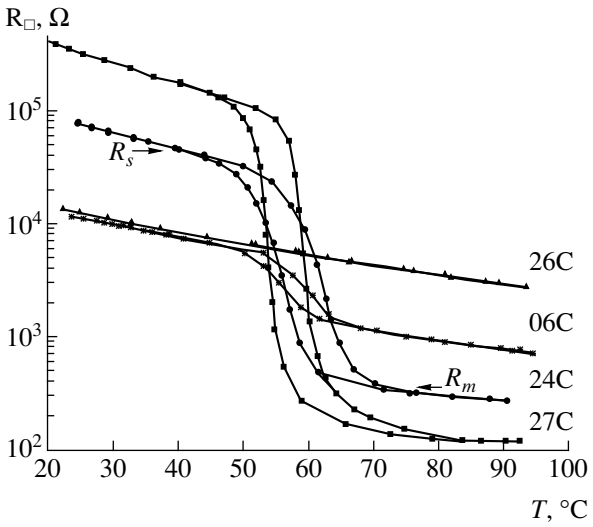

Fig. 1. Temperature variation of the resistance per unit sample area $R_\square$ in some VO_x film samples (indicated by figures at the curves, see table for the sample parameters); R_s and R_m are the sample resistances corresponding to the low- and high-temperature merge points of the hysteresis loop.

A factor giving rise to the current noise in the films studied is probably the martensite transformation characteristic of the semiconductor–metal phase transition in VO_2 [6]. The phase transition in the film, beginning with the formation of a new phase nucleus in the bulk of the existing phase, leads to a change in the VO_2 unit crystal cell volume and eventually to the development of mechanical stresses and accompanying dislocations in the crystal grains [7]. In small-size grains, these

Electrical and noise characteristics of VO_x film samples

Sample no.	$R_{\square S}$, kΩ	TCR, %/K	K, cm^3	n	ΔT_L, °C	T_T, °C	ΔT_T, °C	R_s/R_m
27C	327	4.6	3.2×10^{-18}	1.0	5.3	57	39.4	1200
24C	74	3.3	1.2×10^{-19}	1.1	5.9	59	31	125
26C	12	2.6	3.4×10^{-21}	1.2	No clear phase transition and hysteresis loop			
06C	11	2.7	2.4×10^{-22}	0.6	3.9	58	19	5.1

Note: $R_{\square S}$ and TCR are the resistance per unit sample area and the temperature coefficient of resistance at 25 °C, respectively; K and n are the noise parameter and frequency exponent for the $2/f$ noise according to formula (1); ΔT_L is the hysteresis loop width; T_T is the phase transition temperature; ΔT_T is the phase transition length (measured between the hysteresis loop merge points); R_s/R_m is the ratio of resistances corresponding to the low- and high-temperature merge points of the hysteresis loop.

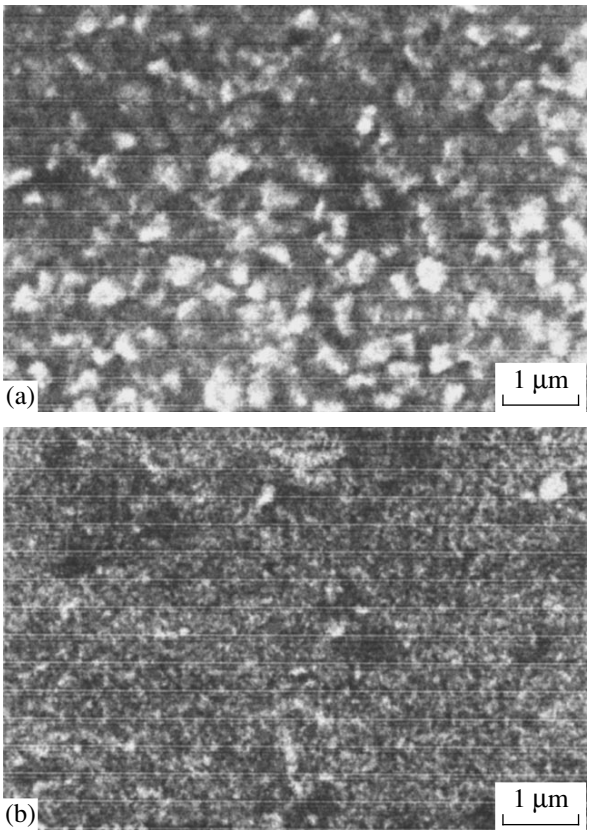

Fig. 2. Micrographs of the surface of samples (a) 26C and (b) 06C observed in a CamScan scanning electron microscope.

mechanical stresses are quite readily released by displacing dislocations to close-lying grain boundaries. In coarser grains, the stress release by dislocations escaped at the grain boundaries is hindered. In addition, the coarse grains may contain 2–3 martensite nuclei interacting with each other via a field of elastic stresses or soft optical phonons [8], the second mechanism (known as the Jahn–Teller martensite mechanism) usually dominating. The Jahn–Teller martensite mechanism leads to the ordering of the new phase nuclei with the formation of a domain superstructure [8] and the development of mechanical stresses on the domain walls.

It must be noted that the Jahn–Teller domain superstructure formation in VO_2 may take place at temperatures above 8°C [8], which are markedly lower than the phase transition temperature in single-crystalline vanadium dioxide (67°C). The appearance and decay of martensite nuclei above 8°C will lead to fluctuations in the mechanical stresses and internal deformations of the domain walls. Therefore, the films containing predominantly VO_2 in the form of coarse grains would exhibit fluctuations in the conduction electron scattering on the stressed domain walls. These fluctuations must be clearly manifested at temperatures well below the phase transition temperature—even in the region of room temperature at which the noise measurements were performed. It should be noted that a close model of the $1/f$ noise generation in VO_2 films was suggested previously [9], where the noise was caused by the fluctuations of internal stresses in blocks of which the film is composed.

Using the magnetron-sputter-deposited VO_x films, we have previously prepared prototype samples of a 65-unit microbolometric array of the membrane type with an area of 46×46 μm by a technology involving photolithography, liquid-phase etching, and ion-sputtering stages [10]. In these samples, a level of the detection capacity of microbolometers [$D^* = 5 \times 10^7$ (cm $Hz^{1/2}$)/W] was limited to a considerable extent by the current $1/f$ noise ($K = 4.4 \times 10^{-20}$ cm^3). The VO_x films obtained in this study exhibit a markedly lower noise level [$K = (2.4–34) \times 10^{-22}$ cm^3). We believe that using these films in MBMs must increase the sensitivity of microbolometers 3–10 times. In addition, the absence of the semiconductor–metal transition in the thermosensitive layer will favor expansion of the range of linearity and/or working temperatures of the microbolometers.

REFERENCES

1. I. A. Khrebtov and V. G. Malyarov, Opt. Zh. **64** (6), 3 (1997) [J. Opt. Technol. **64**, 511 (1997)].
2. T. Breen, M. Kohin, C. A. Marshall, *et al.*, Proc. SPIE **3698**, 308 (1999).
3. V. G. Malyarov, I. A. Khrebtov, Yu. V. Kulikov, *et al.*, Proc. SPIE **3819**, 136 (1999).
4. V. Yu. Zerov, Yu. V. Kulikov, V. N. Leonov, *et al.*, Opt. Zh. **66** (5), 8 (1999) [J. Opt. Technol. **66**, 387 (1999)].
5. F. N. Hooge, T. G. M. Kleinpenning, and L. K. G. Vandamme, Rep. Prog. Phys. **44** (5), 479 (1981).
6. I. A. Khakhaev, F. A. Chudnovskiĭ, and E. B. Shadrin, Fiz. Tverd. Tela (St. Petersburg) **36** (6), 1643 (1994) [Phys. Solid State **36**, 898 (1994)].
7. W. Bruckner, H. Opperman, W. F. Reichelt, *et al.*, Proc. SPIE **1983**, 252 (1994).
8. V. S. Vikhnin, I. N. Goncharuk, V. Yu. Davydov, *et al.*, Fiz. Tverd. Tela (St. Petersburg) **37** (12), 3580 (1995) [Phys. Solid State **37**, 1971 (1995)].
9. M. V. Baĭdakova, A. V. Bobyl', V. G. Malyarov, *et al.*, Pis'ma Zh. Tekh. Fiz. **23** (13), 58 (1997) [Tech. Phys. Lett. **23**, 520 (1997)].
10. V. G. Malyarov, I. A. Khrebtov, A. D. Smirnov, *et al.*, Proc. SPIE (2000) (in press).

Translated by P. Pozdeev

Technical Physics Letters, Vol. 27, No. 5, 2001, pp. 381–383. Translated from Pis'ma v Zhurnal Tekhnicheskoĭ Fiziki, Vol. 27, No. 9, 2001, pp. 64–71.

Silicon Structures with Dielectric Insulation Obtained by Vertical Anisotropic Etching

E. G. Guk, A. G. Tkachenko, N. A. Tokranova, L. S. Granitsyna, E. V. Astrova, B. G. Podlaskin, A. V. Nashchekin, I. L. Shul'pina, and S. V. Rutkovskiĭ

Ioffe Physicotechnical Institute, Russian Academy of Sciences, St. Petersburg, 194021 Russia

Received December 21, 2000

Abstract—Silicon structures with vertical insulating walls were prepared for multielement devices with high element packing density requiring deep pockets in silicon single crystals. The technology is based on the anisotropic etching of (110)-oriented silicon crystals and filling the etch grooves with an organosilicon polymer based suspension. © *2001 MAIK "Nauka/Interperiodica".*

The technology of dielectric insulated silicon (DIS) structures has occupied a firm place among the traditional methods of silicon processing and is widely employed in fabrication of a number of semiconductor devices requiring high-quality insulation of some elements [1]. The applications include multielement photodetectors, position-sensitive detectors of nuclear particles, and some other devices involving single-crystalline silicon layers of considerable thickness. However, in the traditional DIS technology, an increase in the pocket depth implies a significant increase in the area occupied by insulating layers. Other significant disadvantages of the existing DIS technology are the long process time and high energy consumption in the stage of filling the V-shaped etch grooves with polycrystalline silicon. This process is also most unsatisfactory from ecological standpoint.

Below, we propose a new method for the fabrication of DIS structures based on the anisotropic etching of (110)-oriented silicon [2], which allows the grooves of large depth with vertical walls to be obtained in combination with a specially developed technology of filling the etched grooves with an organosilicon polymer based suspension.

The principal possibility of using deep (~100 μm) vertical grooves for dielectric insulation was originally pointed out by Bean and Ranyan [3]. However, practical implementation of this idea was complicated by problems encountered in filling the deep relief by gas-phase deposition of polycrystalline silicon. Indeed, polycrystalline silicon frequently blocks the upper part of a groove in the very beginning of the process, when the channel is by no means completely filled, so that a considerable part of channel remains empty [4]. The proposed method provides for the complete filling of grooves of any depth and shape, thus eliminating the above problems and considerably simplifying the DIS structure fabrication. Our technology of filling the etch grooves with finely dispersed silicon is based on the formation of a homogeneous filling mass using an organosilicon polymer as a binder.

In our experiments, this polymer binder was represented by a dimethylsiloxane rubber (DMSR) of the SKT grade, possessing good solubility and film-forming properties. The chemical structure of this polymer is as follows:

$$R_3Si–[–O–Si(R_2)–]_a–O–SiR_3,$$

where $R = CH_3$. The thermal oxidation of DMSR leads to its decomposition, the main products being SiO_2, H_2O, and CO_2. This process is accompanied by the silicon dioxide structuring due to intermolecular condensation of side silanol groups [5]. However, filling the groove directly with this oxide is impossible because the gas evolution accompanying the thermal degradation process leads to a considerable decrease in volume of the solid phase. In order to retain the initial filler volume in the grooves, we used a DMSR solution containing suspended finely dispersed 3–5 μm silicon particles. Subsequent oxidation of the finely dispersed silicon particles in the grooves increases the filler volume. Thus, we may select a filler composition with the optimum silicon to polymer ratio, which would allow the initial solid phase volume in the groove to be retained upon thermal oxidation of the mixture.

The experiments were performed with 500-μm-thick polished (110)-oriented *n*-Si wafers (KEF-7 grade). The deep groves with vertical walls were formed by the method of alkaline anisotropic etching [6]. In contrast to the anisotropic etching of (100)-oriented silicon (where precise orientation of the etched relief with respect to the crystal axes is required), the etched figures in Si(110) must be precisely oriented to within a few minutes of arc in order to avoid considerable lateral etching. In connection with this, we have developed a special method for high-precision orientation of the long side of etch grooves parallel to the (111) plane projection onto the (110) plane. This was achieved in an

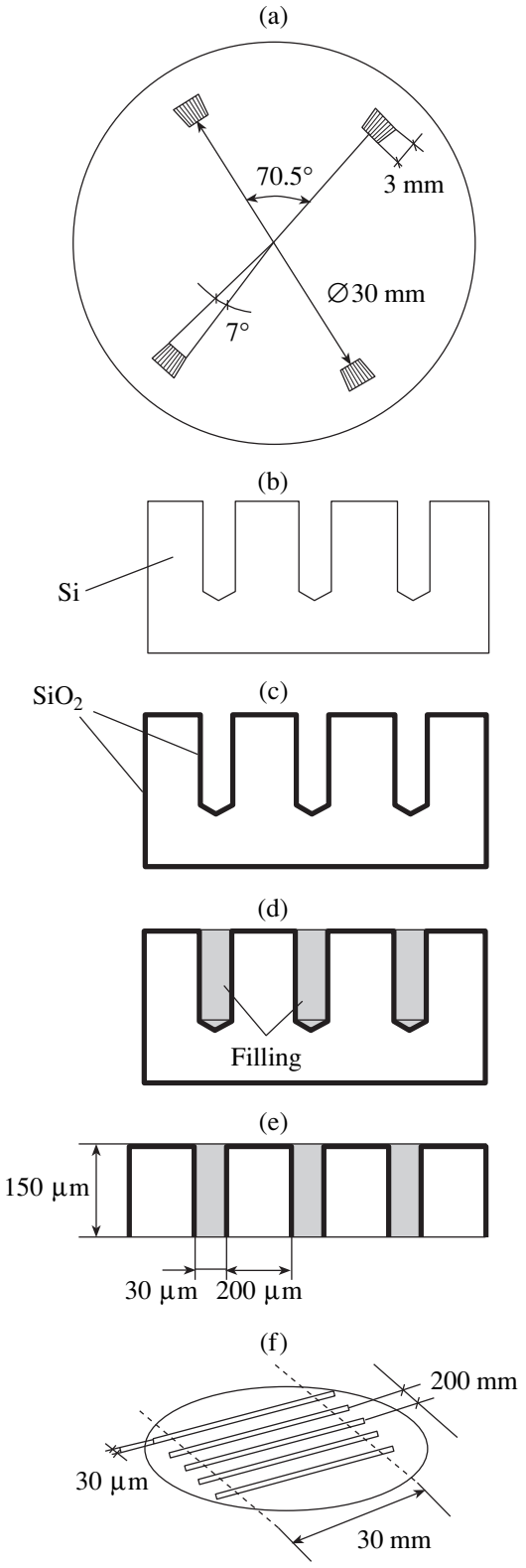

Fig. 1. Schematic diagrams illustrating a new DIS technology based on the anisotropic etching of Si(110) wafers: (a) matching marks used for high-precision orientation of the template pattern relative to the (111) plane projections; (b) deep groove etching; (c) thermal oxidation; (d) groove filling; (e) groove bottom opening; (f) wafer periphery removal.

additional technological stage of forming and etching special matching marks. The marks represented four groups of windows open in the protective oxide mask. The marks were arranged in pairs on the silicon wafer diameters making an angle of 70.5° (Fig. 1a). Each group contained 180 bands with a width of 5 μm and a length of 3 mm, oriented radially at an interval of 2′ (minutes of arc). The anisotropic etching to a depth of 300 μm left only about 20 (of the total of 180) bands distinguishable in each mark, of which only 2–3 elements remained unetched in the lateral direction. The other bands disappeared as a result of the strong lateral etching. Then the protective mask on the silicon surface was restored and the working template pattern was oriented using the obtained matching marks. The anisotropic etching of samples was carried out for 250 min in a 44% aqueous KOH solution at $T = 60$°C.

The anisotropic etching treatment left parallel grooves with a depth of 150 μm, a width of 30 μm, and a length of 35 mm. (Figs. 1b and 2a). The samples with etched grooves were subjected to thermal oxidation in water vapor at 1000°C to form a 0.6-μm-thick oxide layer (Fig. 1c). Then the grooves were filled with a suspension of finely dispersed silicon in a 5% DMSR solution in toluene (this process was effected in a centrifuge). After the solvent removal by preliminary drying, the samples were subjected to thermal degradation at 200°C and oxidized in water vapor at 900°C for 1 h (Fig. 1d). Examination of a sample cleaved perpendicularly to the grooves showed that the grooves are completely filled down to bottom (Fig. 2b). Note that the same silicon suspension can be used to fill the V-shaped grooves (Fig. 2c). In the final stage, the rear side of the etched plate (bearing vertical grooves filled with polycrystalline silicon) was polished to open the groove bottoms (Fig. 1e) and the peripheral parts of the open structure were removed by scribing so as to unshort the pockets (Fig. 1f) and obtain a set of insulated silicon regions.

The final structure comprised a series of isolated single crystal silicon strips with a length of 30 mm and a width of 200 μm or 2 mm, tightly bound with a binder representing sintered and oxidized finely dispersed silicon. In order to eliminate leaks on the cut surfaces, the samples were additionally oxidized for 2 h at 1000°C in water vapor. The electric measurements were conducted on samples with windows made in the insulating oxide layer over the single crystal silicon regions. The leak current between insulated single crystal silicon regions, measured with electrometer in a dark chamber, was about 2×10^{-10} A at a bias voltage of 10 V. Estimates showed that this value is determined by the dielectric properties of insulating thermal oxide.

The structure of the single crystal silicon regions was checked by X-ray topography of the upper surface of the samples. The measurements were performed in the backscattering mode for the 151, 333, and 331 reflections using Cu$K_{\alpha 1}$ radiation. The X-ray diffraction patterns showed evidence of bending of the sample

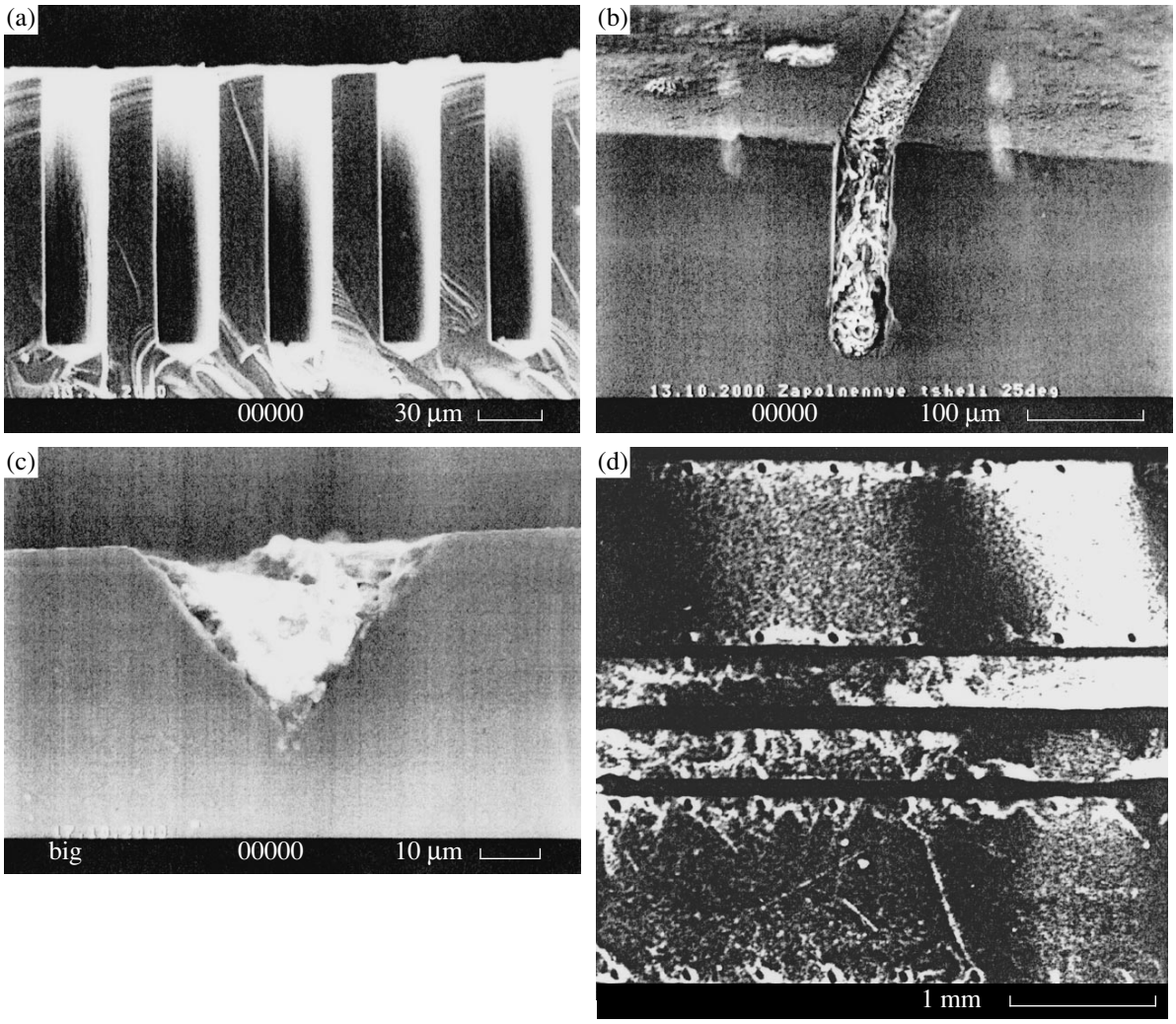

Fig. 2. DIS structures studied by (a–c) scanning electron microscopy and (d) X-ray topography: (a) sample cross section after deep groove etching; (b) cross-section of a filled groove with vertical walls; (c) cross-section of a filled V-shaped groove; (d) X-ray topograph of a final structure (top view) obtained for a 151 reflection measured in the asymmetric Bragg geometry using Cu $K_{\alpha 1}$ radiation (grooves imaged dark; dislocations imaged bright; black dots reflect the matching figures not considered here; nonuniform background contrast indicates bending of the sample plate).

structures and revealed the dislocation formation at the groove boundaries, which is related to the relaxation of mechanical stresses (Fig. 2d). By optimizing the filler composition and the thermal treatment regimes, it was possible to reduce the level of mechanical stresses in the final structures. In principle, it is possible to eliminate deformation of silicon plates and decrease the probability of the formation of defects and dislocations in the working single crystal silicon layer.

Thus, we demonstrated the advantages of a new method developed for the fabrication of deep DIS structures intended for use in various semiconductor devices of the matrix type.

Acknowledgments. This study was supported by the Program "Physics of Solid State Nanostructures" supervised by the Ministry of Science of the Russian Federation (project no. 99-1107).

REFERENCES

1. N. A. Bryukhno, E. M. Zharkovskiĭ, Yu. A. Kontsevoĭ, *et al.*, in *Reviews on Electron Techniques*, Ser. 3: *Microelectronics* (Moscow, 1987), Issue 4.
2. D. L. Kendall, Appl. Phys. Lett. **26**, 195 (1975).
3. K. E. Bean and W. R. Runyan, J. Electrochem. Soc. **124** (1), 5C (1979).
4. S. Ottow, V. Lehmann, and H. Foll, J. Electrochem. Soc. **143** (1), 385 (1996).
5. E. L. Warrick *et al.*, Rubber Chem. Technol. **52** (3), 437 (1979).
6. D. L. Kendall, Annu. Rev. Mater. Sci. **9**, 373 (1979).

Translated by P. Pozdeev

Technical Physics Letters, Vol. 27, No. 5, 2001, pp. 384–386. Translated from Pis'ma v Zhurnal Tekhnicheskoĭ Fiziki, Vol. 27, No. 9, 2001, pp. 72–78.

Fullerenes Catalyze the Graphite–Diamond Phase Transition

A. Ya. Vul'*, V. M. Davidenko*, S. V. Kidalov*, S. S. Ordan'yan, and V. A. Yashin*****

** Ioffe Physicotechnical Institute, Russian Academy of Sciences, St. Petersburg, Russia*

*** Il'ich Abrasive Plant, Joint-Stock Company, St. Petersburg, Russia*

**** St. Petersburg State Technical University, St. Petersburg, Russia*

Received December 15, 2000

Abstract—The effect of fullerenes on the graphite–diamond phase transition was experimentally studied. Adding a catalytic amount of fullerenes to graphite during the diamond synthesis at relatively low pressures (4.5–5.5 GPa) and temperatures (about 1200°C) increases the percentage graphite to diamond conversion by a factor of 1.8 as compared to the case of an initial charge containing only graphite or fullerene. Adding fullerene to graphite allows the pressure and temperature of the synthesis to be decreased. *© 2001 MAIK "Nauka/Interperiodica".*

The discovery of fullerenes, a new allotropic modification of carbon [1], posed a question as to whether the structural transition from fullerene to diamond is possible by analogy with the graphite–diamond phase transition. Indeed, each carbon atom in a fullerene molecule, as well as in the graphite structure, has equivalent contacts with three neighbors and, hence, occurs in an sp^2 hybridized state [2]. Since the development of a method for the fullerene synthesis in macroscopic amounts [3], this problem was studied on an experimental level. The paper with the intriguing title "Fullerene C_{60} Harder than Diamond?" [4] presented theoretical estimates suggesting that the hydrostatic compressibility of fullerene may exceed that of diamond. This hypothesis further stimulated the study of phase transitions in fullerenes at high pressures and somewhat changed the direction of research.

Presently, it is reliably established that fullerene phases of the C_{60} type polymerized at high temperatures and pressures ($T \approx 1000$°C, $P \approx 10$ GPa) are in fact competitive with diamond in hardness, while exceeding the latter in plasticity [5]. However, the economic prerequisites for commercial use of these materials are yet unclear because typical pressures used for the synthesis of commercially significant hard materials (diamond and boron nitride) are markedly lower (ranging within 4–8 GPa) [6, 7]. The problems involved in the diamond synthesis from fullerenes were given much less attention, although the first patent on replacing graphite by fullerene in the diamond synthesis appeared a decade ago [8].

A hypothesis that replacing graphite by C_{60} fullerene in the diamond synthesis may allow for a decrease in the process parameters because a curvature of the fullerene cluster surface provides for a certain "admixture" of the sp^3 hybridization (typical of the diamond structure) in the carbon–carbon bonds was directly formulated in the well-known monograph [2] and seemed to be promising. However, attempts at using fullerene instead of graphite did not confirm these expectations. It was found [9] that the diamond synthesis from fullerene requires even higher temperatures ($T > 1400$°C) and pressures ($P > 6$ GPa) than the process involving graphite. Moreover, the percentage of fullerene to diamond conversion depends on the metal catalyst employed, only a few of which provided for the level of conversion achieved for the graphite–diamond phase transition. The nature of the effect of the metal catalyst and fullerene combination remained unclear.

In this paper, we develop an alternative approach based on the idea of using fullerenes as an additional catalyst in the standard process of diamond synthesis from graphite in high-pressure vessels [10, 11].

Although there is still no commonly accepted point of view concerning the mechanism of diamond synthesis from graphite [12], most of the researchers adopt a model assuming that the diamond crystals grow from carbon dissolved in the metal catalyst. According to this model, the diamond growth temperature is limited from below by the melting temperature of the metal and by the diamond–graphite equilibrium curve on the carbon phase diagram. Some rare deviations from this behavior illustrate certain uncompleteness of the model [13]. First, there are indications that the diamond crystals may grow from a solid solution formed by carbon and the metal catalyst; second, the crystal growth sometimes proceeds at temperatures markedly exceeding the melting point of the metal catalyst, which also disagrees with the generally adopted model.

Based on the first experimental results [14], it was suggested that the temperature of fullerene dissolution in a metal catalyst is lower than that of graphite, which must decrease the temperature of diamond synthesis. The assumption was based on a higher chemical potential of the curved surface of fullerene molecules [15]. In

1063-7850/01/2705-0384$21.00

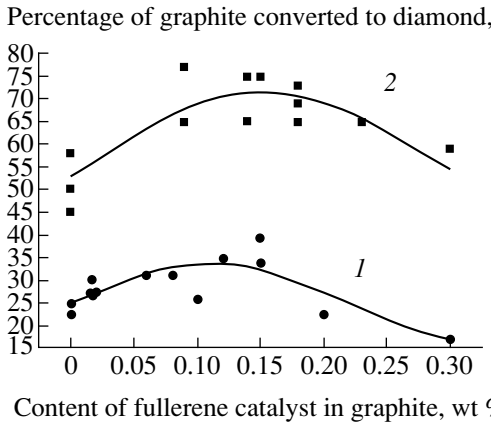

Fig. 1. The effect of fullerenes on the percentage graphite to diamond conversion in a graphite–metal charge processed under static synthesis conditions: (*1*) 4.5 GPa, 10 min; (*2*) 5.5 GPa, 90 s.

our opinion, dissolved fullerene forms crystallization centers on which the growth of diamond crystals takes place, while graphite still serves as the main source of carbon for the crystal growth process. This approach allows very small "catalytic" fullerene additives to graphite to be used in the diamond synthesis.

Below, we present the results of experiments that confirm validity of this approach. Some data were previously published in a patent description [10].

The experiments were carried out using a 10-MN press and a standard high-pressure apparatus with a working chamber comprising two truncated hemispheres with a total volume of 4.4 cm^3. The initial material for the synthesis was a mixture of graphite with a nickel–manganese catalyst. The high-pressure chamber was heated with a 50-Hz alternating current in the regime of heating power stabilized to within 1%. The pressure was also stabilized with an error not exceeding 1%. The synthesized products were analyzed by a conventional chemical enrichment technology used in the artificial diamond synthesis, followed by the diamond crystal size classification.

Figure 1 presents data on the efficiency of graphite to diamond conversion with catalysts containing fullerene additives at an amount from 10^{-2} to 3×10^{-1} wt % relative to graphite. Fullerenes were added either in a pure form, or with a fullerene-containing soot, or as a $C_{60} + C_{70}$ fullerene mixture. In the latter two cases, the net fullerene content was calculated. As seen from these data (Fig. 1), the fullerene additives produce a certain catalytic effect and there is an optimum relative content of fullerenes in the graphite in the interval from 0.01 to 0.3 wt %. Under the optimum conditions, the percentage of graphite to diamond conversion increases by a factor of 1.8 as compared to the fullerene-free reactor charging.

In order to check for the statistical scatter of data, we have also studied the effect of fullerene catalyst on the diamond synthesis in commercial apparatuses equipped with a 6.3-MN press. The experiments were performed in a high-pressure vessel at a pressure of

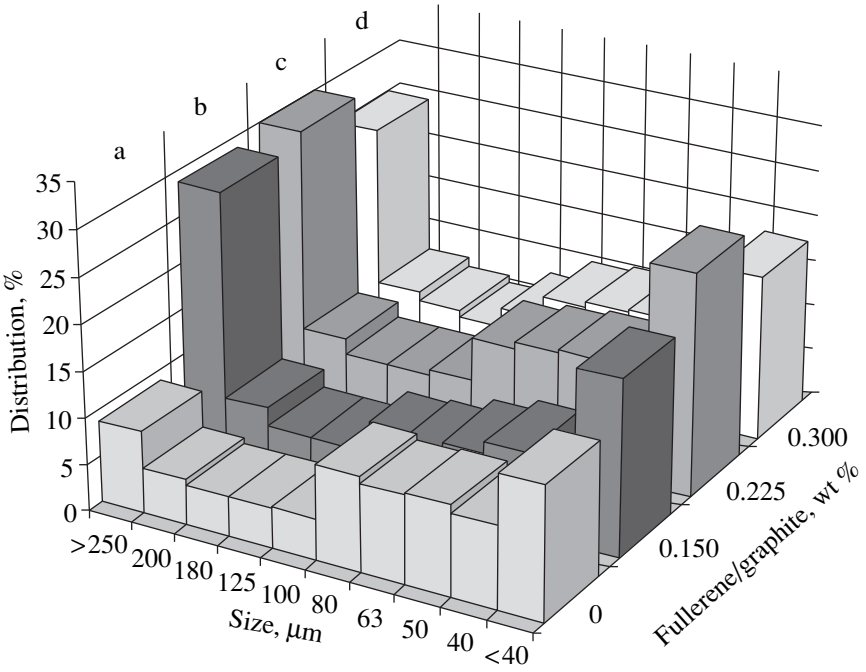

Fig. 2. Diamond size distribution in four series of syntheses using 6.3-MN commercial apparatuses. The integral of the distribution profile gives the total percentage graphite to diamond conversion for each series (differing by a relative content of the fullerene catalyst).

5.5 GPa and a temperature in the range of the thermodynamic stability of diamond.

There were four series of experiments (a–d) using virtually the same charge composition, differing only by insignificant amounts of fullerene: (a) no fullerene (780 runs); (b) 0.15 wt % (1740 runs); (c) 0.225 wt % (1710 runs); (d) 0.3 wt % (1780 runs). The experimental results were averaged within each series to show the percentage graphite to diamond conversion of 50.5, 56.5, 66.1, and 60.2 in series a–d, respectively.

Figure 2 shows the results of the sieving analysis of the diamond crystal size distribution in the four series of experiments, presented by histograms averaged within each series. As is seen, the presents of fullerene catalysts noticeably changes the crystal size distribution toward increasing percentage content of coarse and fine particles. The proportion of coarse (>250 μm) and fine (<40 μm) diamonds exhibits of a nearly twofold increase as compared to the fullerene-free charging. The time of synthesis in all runs being the same, we may suggest that fullerenes increase the crystal growth rate and/or serve as the "crystallization centers." On the latter centers, the crystal growth begins earlier (at lower pressures and temperatures) than in pure graphite, which allows the diamonds to grow to a greater size.

Based on the results of our experiments, we may draw two conclusions: (i) fullerenes exhibit an additional catalytic effect during the diamonds synthesis from graphite in the presence of metal catalysts; (ii) adding fullerenes increases the percentage graphite to diamond conversion up to 35% for the synthesis at a pressure of 4.5 GPa and up to 75% at 5.5 GPa, which is 1.8 times the level achieved with pure graphite. The results obtained in large commercial series indicate that the use of fullerenes as catalytic additives to the graphite charge may be economically profitable for the commercial production of artificial diamonds.

REFERENCES

1. H. W. Kroto, J. R. Heath, S. C. O'Brien, *et al.*, Nature **318**, 162 (1985).
2. M. S. Dresselhaus, G. Dresselhaus, and P. Eklund, *Science of Fullerenes and Carbon Nanotubes* (Academic, New York, 1996).
3. W. Krätschmer, L. D. Lamb, F. Fostiropoulos, *et al.*, Nature **347**, 354 (1990).
4. R. S. Ruoff and A. L. Ruoff, Nature **350**, 663 (1991).
5. V. V. Brazhkin, A. G. Lyapin, S. V. Popova, *et al.*, J. Appl. Phys. **84**, 219 (1998).
6. O. Fugunaga, Y. S. Ko, M. Konoue, *et al.*, Diamond Relat. Mater. **8**, 2036 (1999).
7. L. F. Vereshchagin, *Selected Works. Synthetic Diamonds and Hydrostatic Extrusion* (Nauka, Moscow, 1982).
8. *Utilization de fullerenes comme produits de depart dans la fabrication de diamant,* Nunez-Requiero, Manuel, PCT WO 93/02212. July 10, 1992, National Priority Date (France) July 15, 1991, Published February 4, 1993, FR2684090A1.
9. G. Bocquillon, C. Bogicevic, C. Fabre, *et al.*, J. Phys. Chem. **97**, 12924 (1993).
10. *Method for Production Artificial Diamonds*, PCT Application A. Vul', S. Kidalov, S. Kozyrev, *et al.*, RU1997000114492, Patent RU N2131763 (1997).
11. M. V. Baidakova, V. Yu. Davidov, S. V. Kidalov, *et al.*, in *Extended Abstracts and Program of the 23rd Biennial Conference on Carbon, Penn State Univ., 1997*, p. 354.
12. N. Setaka, in *Synthetic Diamond: Emerging CVD Science and Technology*, Ed. by K. E. Spear and J. P. Dismukes (Wiley, New York, 1994), pp. 57–90.
13. H. Kanda, M. Akaishi, and S. Yamaoka, Appl. Phys. Lett. **65**, 784 (1994).
14. V. A. Mukhanov, N. G. Spitsyna, L. I. Buravov, *et al.*, Pis'ma Zh. Tekh. Fiz. **22** (18), 1 (1996) [Tech. Phys. Lett. **22**, 731 (1996)].
15. V. V. Brazhkin, A. G. Lyapin, Y. V. Antonov, *et al.*, Pis'ma Zh. Éksp. Teor. Fiz. **62**, 328 (1995) [JETP Lett. **62**, 350 (1995)].

Translated by P. Pozdeev

Technical Physics Letters, Vol. 27, No. 5, 2001, pp. 387–388. Translated from Pis'ma v Zhurnal Tekhnicheskoĭ Fiziki, Vol. 27, No. 9, 2001, pp. 79–82.

The Process of a Bi-2223/Ag Ribbon Sintering Studied by the Method of Acoustic Emission

E. Dul'kin*, V. Beilin*, E. Yashchin*, M. Roth*, and L. V. Grebenkina**

** Graduate School of Applied Science, The Hebrew University of Jerusalem, Jerusalem, 91904 Israel*

*** Institute of Mechanics and Applied Mathematics, Rostov State University, Rostov-on-Don, 344104 Russia*

Received December 14, 2000

Abstract—The secondary sintering of a Bi-2223/Ag ribbon, following the stages of primary sintering and rolling to a strain of $\varepsilon \sim 18\%$, was studied by methods based on the acoustic emission, thermal expansion, and magnetic susceptibility measurements. During the second thermal treatment, a signal of acoustic emission from the ribbon was detected in a temperature range from 570 to 660°C. The process of liquid-phase healing of the rolling cracks in the ribbon material is considered as a reason of the acoustic emission. The possibility of using the acoustic emission measurements for nondestructive testing in the Bi-2223/Ag ribbon fabrication technology is considered. © *2001 MAIK "Nauka/Interperiodica".*

The technology used for the fabrication of superconducting Bi-2223/Ag ribbons includes several stages: (i) filling the Ag tube with a nonsuperconducting Bi–Pb–Sr–Ca powder mixture (corresponding to the 2223-phase stoichiometry), (ii) drawing of the filled tube, (iii) flat ribbon rolling, and (iv) thermomechanical treatment involving two sintering stages with intermediate rolling [1]. The intermediate rolling provides for the densification of a ceramic composition, which is necessary to reach a high critical current density J_c.

Unfortunately, the rolling of sintered superconducting ceramics induces microcracks in the material. These defects, which frequently remain unhealed even after a prolonged secondary sintering of the material, limit the current-carrying capacity of the ribbon [2–3]. The healing of microcracks in Bi-2223/Ag ribbons was never studied in detail: it was only suggested that this process must be controlled by liquid-phase reactions. The phenomenon of rapid elimination of the rolling damage discovered recently based on the results of magnetic susceptibility and magnetooptical measurements [4] indicated that the microcracks can be healed even at the stage of heating the rolled ribbons to a temperature of secondary sintering.

As is known, the process of crack generation and elimination in high-T_c ceramics can be studied by methods based on the acoustic emission measurements [5]. Previously, this approach was successfully used for the study of recrystallization in sintered YBCO ceramics [6]. The purpose of this work was to study the secondary sintering of Bi-2223/Ag ribbons by methods based on the acoustic emission (AE), thermal expansion, and magnetic susceptibility (MS) measurements.

The experiments were performed on 10-mm-long 3-mm-wide 0.250-mm-thick samples of a Bi-2223/Ag ribbon prepared as described elsewhere [7]. After the primary sintering stage, the samples were rolled to a final strain of $\varepsilon \sim 18\%$. The AE intensity $\dot{N}$ and the thermal expansion ΔL were measured in the course of heating and cooling at a rate of 2–3 K/min [8]. The magnetic susceptibility was measured by the inductive technique at a frequency of 740 Hz in the temperature range from 250 to 77 K.

The results of AE measurements are presented in the figure. As the samples were heated above room temperature, the ceramics initially exhibited monotonic compression and the AE signals were absent. The sample shrinkage (reaching ~5%) ceased in the region of 450°C, and then the first AE signals were detected above 570°C. As the temperature was increased further, the AE intensity $\dot{N}$ exhibited exponential growth and then sharply terminated at $T = 660$°C. The heating was

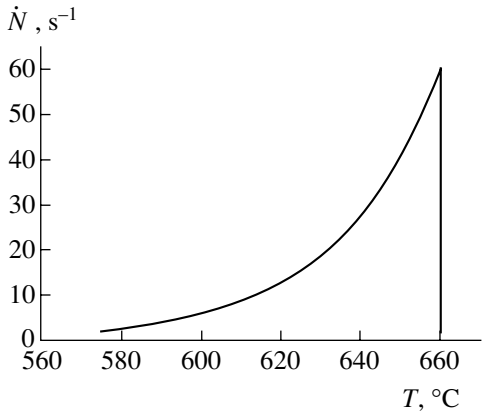

A plot of the relative thermal expansion $\Delta L/L$ and the acoustic emission intensity $\dot{N}$ versus temperature for Bi-2223/Ag ribbons.

continued up to 836°C, but the samples exhibited neither dilatation not acoustic emission.

The observed AE response can be interpreted based on the results of *in situ* investigation of the phase transformations in Bi-2223/Ag ribbons [9]. According to the phase diagram, this system occurs in the liquid state in a temperature range from 400 to 660°C [9]. Note that this temperature range coincides with the interval (570–660°C) featuring the acoustic emission in our samples. Therefore, we may suggest that the liquid phase formation favors healing of the rolling-induced microcracks, which are the main source of the AE signal. This hypothesis is confirmed by the magnetic susceptibility data: a short-time (1 h) annealing of the rolled ribbon at 650°C leads to narrowing of a peak of the imaginary part $\chi''(T)$ of the magnetic susceptibility in the vicinity of the critical temperature. As was demonstrated in [4], this is evidence for an increase in the degree of the electrical connectivity of the ceramics related to the crack healing.

Thus, the AE signals observed in our samples heated in the temperature interval from 570 to 660°C reflect the process of crack healing during the secondary sintering of rolled Bi-2223/Ag ribbons. It should be noted that the AE measurements are sufficiently sensitive to observe the early stage of this process during relatively rapid heating. Therefore, the AE method can be effectively used for the study of processes occurring in Bi-2223/Ag high-T_c ceramic ribbons and for the quality monitoring in the course of their fabrication.

REFERENCES

1. L. Martini, Supercond. Sci. Technol. **11**, 231 (1998).
2. J. W. Anderson, X. Y. Cai, M. Feldmann, *et al.*, Supercond. Sci. Technol. **12**, 617 (1999).
3. M. Polak, J. A. Parrell, A. Polyanskii, *et al.*, Appl. Phys. Lett. **70**, 1034 (1997).
4. A. Polyanskii, V. Beilin, A. Goldgirsh, *et al.*, in *Proceedings of the 2000 International Workshop on Superconductivity, Matsue-shi, Shimane, Japan, 2000*, p. 253.
5. M. P. Staines and N. E. Flower, Supercond. Sci. Technol. **4**, S233 (1991).
6. E. A. Dul'kin, Sverkhprovodimost: Fiz., Khim., Tekh. **7**, 105 (1994).
7. V. Beilin, A. Goldgirsh, E. Yashchin, *et al.*, Physica C (Amsterdam) **309**, 56 (1998).
8. E. A. Dul'kin, Sverkhprovodimost: Fiz., Khim., Tekh. **5**, 102 (1992).
9. T. Frello, H. F. Roulsen, L. Gottschalk Andersen, *et al.*, Supercond. Sci. Technol. **12**, 293 (1999).

Translated by P. Pozdeev

Technical Physics Letters, Vol. 27, No. 5, 2001, pp. 389–393. Translated from Pis'ma v Zhurnal Tekhnicheskoĭ Fiziki, Vol. 27, No. 9, 2001, pp. 83–94.

The Interaction of Charged Planes in an Electron Cloud and Plasma

S. I. Yakovlenko

General Physics Institute, Russian Academy of Sciences, Moscow, 117942 Russia

Received December 18, 2000

Abstract—Distributions of the field potential, the field intensity, and the plasma density are considered for charged planes surrounded by thermoemission electrons, compensating the charge of these planes, or by a finite-density plasma. It is shown that the planes in both cases repulse each other due to the action of electrostatic forces. An expression for the electrostatic pressure is derived. © *2001 MAIK "Nauka/Interperiodica".*

Introduction

Among possible models describing the properties of a thermoemission dust plasma [1], a two-dimension model of dust particles is of special interest because it allows a general solution by quadratures to the Poisson–Boltzmann equation. It is a usual practice (see, e.g., [2, 3]) to consider the case when positive charges in the plasma are totally concentrated on the dust particles surrounded by a cloud of thermoelectrons. However, the situation involving additional ionization of the gas containing the dust particles is also of interest. Examples are the dust plasma in an electric discharge and the dust plasma under the nuclear excitation conditions [4, 5]. Below, we will consider the interaction of charged planes in these cases.

Formulation of the Problem

The Poisson–Boltzmann equation. Let us consider the case when the electron gas surrounding the charged particles is formed due to the emission of electrons from the dust particles possessing a sufficiently high temperature T. In addition, the particles are surrounded by a partially ionized gas. In order to find the spatial distribution of the potential ϕ, the field intensity $\mathbf{F} = -\nabla\phi$, and the charge density $\rho = e(N_i - N_e)$, we must solve the Poisson equation $\nabla\mathbf{F} = 4\pi\rho$. The ion and electron densities N_i and N_e appearing in this equation are determined by the Boltzmann distribution: $N_i = N_{i0}\exp(-e\phi/T)$ and $N_e = N_{e0}\exp(e\phi/T)$, where N_{i0} and N_{e0} are the ion and electron densities at the points of zero potential and ∇ is the vector Hamiltonian.

Thus, the Poisson–Boltzmann equation takes the form

$$\Delta\phi = 4\pi e(N_{e0}\exp(e\phi/T) - N_{i0}\exp(-e\phi/T)), \quad (1)$$

where $\Delta = \nabla^2$ is the Laplacian. The particles and the plasma are assumed to have the same temperature.

Dimensionless variables. The length will be measured in units of $d = 8\pi e^2/T$. In terms of the dimensionless potential φ, field intensity $\mathbf{E}$, and electron density n_e

$$\varphi = \phi e/T; \quad \mathbf{E} = \mathbf{F}ed/T; \quad n_e = (8\pi e^2/T)^3 N_e, \quad (2)$$

Eq. (1) reduces to the following equation for the dimensionless potential φ:

$$\Delta\varphi = (1/2)(\exp(\varphi) - \delta\exp(-\varphi)), \quad (3)$$

where $\delta = N_{i0}/N_{e0}$ is the parameter describing the additional ionization. In this case, $(\nabla\mathbf{E}) = -(1/2)(\exp(\varphi) - \delta\exp(-\varphi)$ and $\mathbf{E} = -\nabla\varphi$. Since the plasma is quasi-neutral, $0 \le \delta \le 1$.

In the two-dimensional case, Eq. (3) takes the form

$$\begin{gathered} d^2\varphi/dx^2 = (1/2)(\exp(\varphi) - \delta\exp(-\varphi)), \\ E = -d\varphi/dx, \quad n_e = \exp(\varphi). \end{gathered} \quad (4)$$

Here, x is the distance to the charged particle.

Boundary conditions. It is natural to set the density of the positive charge of charged surface σ as the first boundary condition. Thus, we specify the field intensity F_0 on the charged surface. This value corresponds to the field intensity in a plane capacitor: $F_0 = 4\pi\sigma$ or $E_0 = \sigma d^2/2e$.

The second boundary condition is set at some point a_0 corresponding to the zero field intensity. At this point, the surface charge is fully compensated by the charge of the electron layer: $E(a_0) = 0$.

Distribution of the Field Intensity and Potential

General solution. The most comprehensive considerations of Eqs. (4) in the cases of $\delta = 1$ and 0 cm are given in [6] and [3], respectively. Here, we analyze the general case.

1063-7850/01/2705-0389$21.00

Depress the Poisson–Boltzmann equation order by treating the field intensity as a function of potential:

$$EdE/d\varphi = (1/2)(\exp(\varphi) - \delta\exp(-\varphi)).$$

The first integration yields a relationship between the field intensity and the potential:

$$E = (\exp(\varphi) + \delta\exp(-\varphi) - \exp(\varphi_1) - \delta\exp(-\varphi_1))^{1/2}. \quad (5a)$$

Here, φ_1 is the potential at point a_0 of the zero field.

The second integration yields a relationship between the potential φ and the coordinate x:

$$x = \int_{\varphi}^{\varphi_0} \frac{dy}{\sqrt{\exp(y) + \delta\exp(-y) - \exp(\varphi_1) - \delta\exp(-\varphi_1)}}. \quad (5b)$$

Here $\varphi_0 = \varphi(0)$ is the potential on the charged plane. This value is connected with the specified boundary field intensity E_0 by the relationship (5a) taken at $\varphi = \varphi_0$. A relationship between φ_1 and φ_0 (and, accordingly, E_0) follows from formula (5b) for $x(\varphi_1) = a_0$. Formulas (5) represent the general solution by quadratures to the two-dimensional problem under study.

Lone charged plane. Consider a lone charged plane ($a_0 \longrightarrow \infty$) immersed into a half-space with zero density of positive charges ($\delta = 0$). If the thermoemission electrons totally shield the positive charge of this plane, we should set $\delta = 0$ and $\varphi_1 = -\infty$ in Eq. (5b), after which the integration yields

$$\varphi(x) = 2\ln[2E_0/(xE_0 + 2)]; \quad (6)$$
$$E(x) = 2E_0/(xE_0 + 2), \quad n_e(x) = [2E_0/(xE_0 + 2)]^2.$$

If the lone charged plane ($a_0 \longrightarrow \infty$) is immersed into a half-space filled with a plasma, we should set $\delta = 1$ because the surface density of positive charges in a flat plasma layer will be infinite for an infinitely thick layer (at a finite space charge density). Therefore, we can neglect thermoemission electrons located at infinity. Assuming the field and the potential to be zero at an infinite distance from the charged plane (accordingly, $\varphi_1 = 0$), performing integration, and solving the obtained expression for φ, we arrive at a well-known result (see, e.g., [6, 7]):

$$\varphi(x, \varphi_0) = 2\ln\left(\frac{1 + \exp(-x)\tanh(\varphi_0/4)}{1 - \exp(-x)\tanh(\varphi_0/4)}\right),$$

$$E = 2\sinh(\varphi/2),$$

$$n_e(x, \varphi_0) = \left(\frac{1 + \exp(-x)\tanh(\varphi_0/4)}{1 - \exp(-x)\tanh(\varphi_0/4)}\right)^2,$$

where $\varphi_0 = 2\,\mathrm{arcsinh}(E_0/2)$.

Two charged planes. The field between two charged planes vanishes at a finite distance $x = a_0$. For planes with equal surface charge densities, the distance a_0 is the halved spacing between the planes.

If $\delta = 0$, integration of Eq. (5b) yields

$$\varphi(x) = \ln(E^2 + E_1^2), \quad E(x) = E_1\tan[(a_0 - x)E_1/2], \quad n_e(x) = (E^2 + E_1^2), \quad (7)$$

where the quantity $E_1 \equiv \exp(\varphi_1/2)$ (and, accordingly, φ_1) is related to a_0 via a simple formula:

$$a_0 = (2/E_1)\arctan(E_0/E_1). \quad (8)$$

For $\delta \neq 0$, the relationship between φ_1 and a_0, φ_0, and δ is far more complicated:

$$a_0 = \int_{\varphi_1}^{\varphi_0} \frac{dy}{\sqrt{\exp(y) + \delta\exp(-y) - \exp(\varphi_1) - \delta\exp(-\varphi_1)}}$$

$$= \frac{1}{\delta^{1/4}} \int_{\varphi_1 + 2\ln(1/\delta)}^{\varphi_0 + 2\ln(1/\delta)} \frac{dy}{\sqrt{2\cosh(y) - \cosh(\varphi_1 + 2\ln(1/\delta))}}$$

$$= \frac{1}{\delta^{1/4}} \int_{\varphi_1 + 2\ln(1/\delta)}^{\varphi_0 + 2\ln(1/\delta)} \frac{(1/2)dy}{\sqrt{\cosh^2(y/2) - \cosh^2(y_1/2)}}$$

$$= \frac{k}{\delta^{1/4}} \int_{u(\varphi_0 + 2\ln(1/\delta))}^{u(\varphi_1 + 2\ln(1/\delta))} \frac{dz}{\sqrt{(1 - z^2)(1 - k^2z^2)}}$$

$$= \frac{k}{\delta^{1/4}} F(k, u(\varphi_0 + 2\ln(1/\delta))),$$

or

$$a_0 = \delta^{-1/4} kF(k, u(\varphi_0 + 2\ln(1/\delta))), \quad (9)$$

where

$$u(\varphi) = 1/(k\cosh(\varphi)), \quad k = 1/\cosh(\varphi_1 + 2\ln(1/\delta)),$$

$$F(k, u) = \int_u^1 \frac{dz}{\sqrt{(1 - z^2)(1 - k^2z^2)}}.$$

An implicit dependence of the potential on the coordinate x is determined by the expression

$$x = a_0 - \delta^{-1/4} kF(k, u(\varphi + 2\ln(1/\delta))). \quad (10)$$

It is of interest to consider the case of a large positive potential $\varphi_0 \gg 1$. With $\varphi_0 \longrightarrow \infty$, we obtain [6] that

$a_0 = \delta^{-1/4} kK(k)$, where $K(k) \equiv F(k, 0)$ is the complete elliptic integral written in its normal form.

The distributions of potential in the cases (Fig. 1) when two conducting planes with identical potentials $\varphi = \varphi_0$ are placed into an electron cloud compensating their charges ($\delta = 0$) or into and unbounded plasma ($\delta = 1$) are shown in Figs. 2 and 3.

Repulsion of Charged Planes

Electrostatic pressure. The field intensities to the left and to the right of the plane surface (Fig. 1) $F_{01} = (T/ed)E_{01}$ (on the side of the unbounded half-space) and $F_{02} = (T/ed)E_{02}$ (on the side of the space bounded by another plane) are different. In this case, the field produces an electrostatic pressure onto the plane:

$$P = (1/8\pi)(F_{01}^2 - F_{02}^2) = (1/8\pi)(T/ed)^2 p = T(T/8\pi e^2)^3 p,$$

where $p = (E_{01}^2 - E_{02}^2)$ is the dimensionless pressure. When $E_{01} > E_{02}$, the planes repulse each other; when $E_{01} < E_{02}$, they attract each other.

Thermoemission plasma. In the case of a thermoemission plasma ($\delta = 0$), we have (see also [3])

$$E_{01}^2 = n_{e0}, \quad E_{02}^2 = n_{e0} - E_1^2.$$

Here, $n_{e0} = C(b)\vartheta^{-3/2}\exp(-1/\vartheta)$ is the dimensionless density of thermoemission electrons near the heated plane. This expression follows from the Richardson–Dushman formula: $C(b) = 2(m_e/2\pi\hbar^2)^{3/2}(8\pi e^2)^3/b^{3/2} = 2.9 \times 10^5\ (\text{eV}/b)^{3/2}$, where $\vartheta = T/b$ is the reduced temperature, b is the work function of an electron leaving the wall, and $\hbar$ is the Planck constant.

As a result, we obtain the following formula for the dimensionless pressure:

$$p = E_{01}^2 - E_{02}^2 = E_1^2 \geq 0.$$

Thus, in this system, the force directed toward the unbounded half-space always exceeds the force directed toward the space bounded by another plane. In other words, the planes repulse each other. This is caused by the pressing-out of electrons from the interplane space toward electrodes (this effect was earlier mentioned in [3]).

The value of $E_1 \equiv \exp(\varphi_1/2)$ is related to the plane half-spacing a_0 and the electrode potential φ_0 via the transcendental relationship (6). From this formula, we obtain a relationship between the potential and a_0:

$$a_0 = \frac{2}{E_1}\arctan\left(\frac{E_{02}}{E_1}\right) = \frac{2}{E_1}\arctan\left(\frac{\sqrt{E_{01}^2 - E_1^2}}{E_1}\right)$$

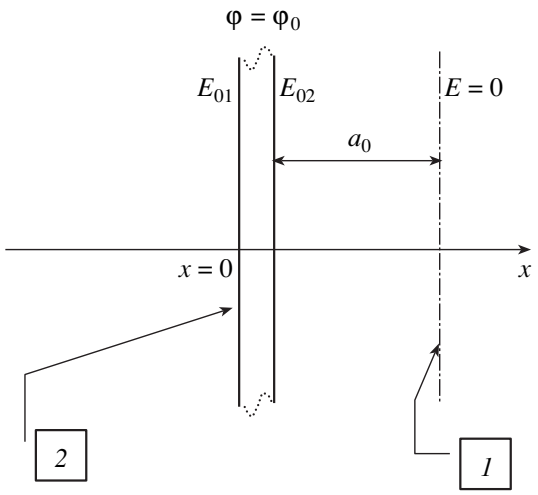

Fig. 1. Geometry of the problem of two plates surrounded by an electron cloud or placed into a plasma: (*1*) the axis of symmetry and (*2*) the plate with a specified potential.

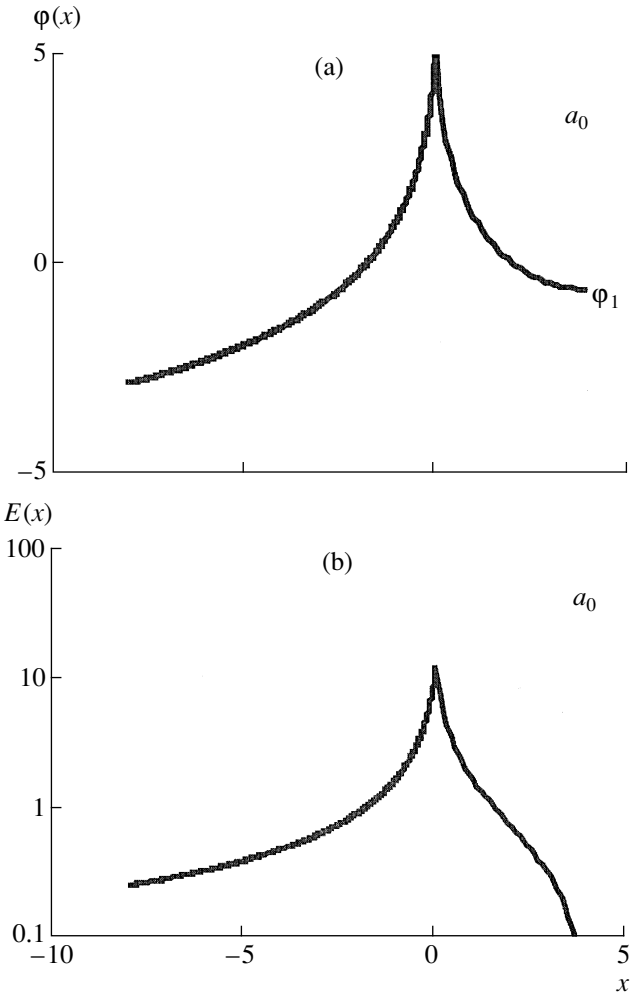

Fig. 2. Plots of (a) the potential and (b) the field intensity vs. coordinate x in the problem of two plates with $\delta = 0$, $a_0 = 4$, and $\varphi_0 = 5$.

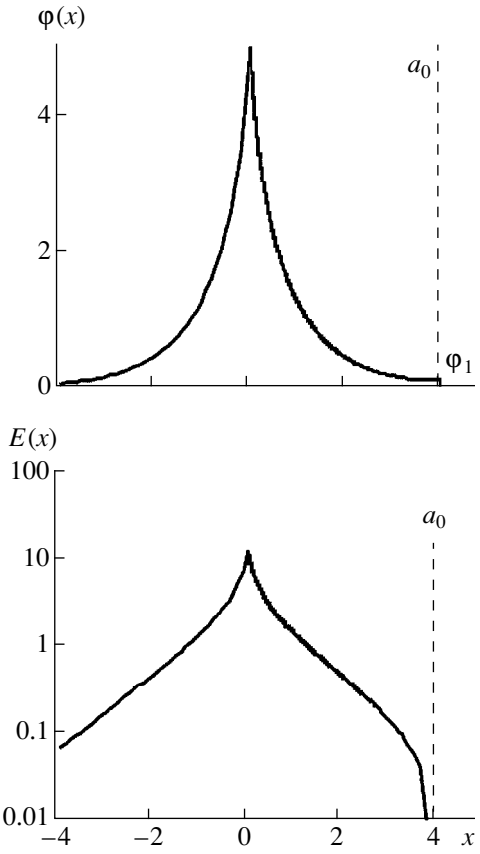

Fig. 3. The same case as in Fig. 2 with $\delta = 1$, $a_0 = 4$, and $\varphi_0 = 5$.

or

$$a_0 = \frac{2}{\sqrt{p}}\arctan\left(\frac{\sqrt{n_{e0} - p}}{p}\right). \quad (11)$$

At large distances, the pressure magnitude decreases proportionally to the squared spacing between the planes and tends to a finite value at small distances. In other words, $p = (\pi/a_0)^2$ at $a_0 \gg 1$ (the most interesting case) and $p = n_{e0}$ at $a_0 \ll 1$ (Fig. 4).

Charged planes in plasma. Let us consider the case when the planes are immersed into an unbounded plasma ($\delta = 1$). From formula (5a), we obtain

$$E_{01}^2 = 4\sinh^2(\varphi_0/2),$$
$$E_{02}^2 = 4(\sinh^2(\varphi_0/2) - \sinh^2(\varphi_1/2)),$$

from which, it follows that

$$p = (E_{01}^2 - E_{02}^2) = 4\cosh(\varphi_1). \quad (12)$$

If $\delta = 1$, the planes also repulse each other [6]. In this case, according to Eq. (9),

$$a_0(\varphi_0, \varphi_1) = k(\varphi_1)F(k(\varphi_1), u(k(\varphi_1), \varphi_0)), \quad (13)$$

where $u(\varphi) = 1/(k\cosh(\varphi))$ and $k = 1/\cosh(\varphi_1)$. The dependence of φ_0 on n_{e0} is determined by the expression

$$n_{e0} = \left(\frac{1 + \tanh(\varphi_0/4)}{1 - \tanh(\varphi_0/4)}\right)^2 = \exp(\varphi_0).$$

Accordingly, $\varphi_0 = \ln(n_{e0})$.

Expressions (11) and (12) specify a parametric relationship between the pressure, the plane spacing, and the density n_{e0} (Fig. 5).

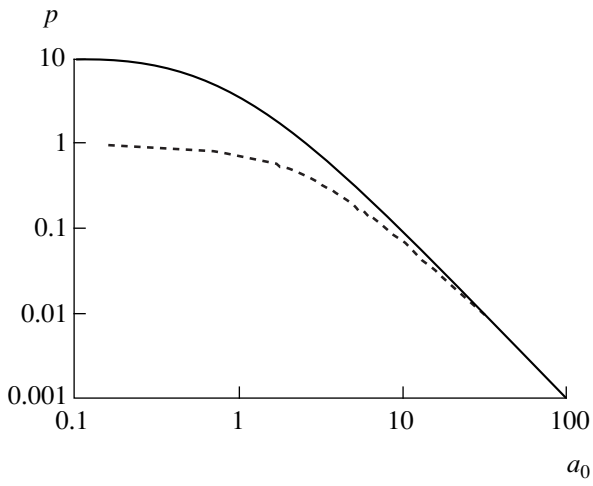

Fig. 4. Electrostatic pressure p vs. the plane half-spacing a_0 at $\delta = 0$ and $n_{e0} = 10$ (solid curve) and 1 (dotted curve).

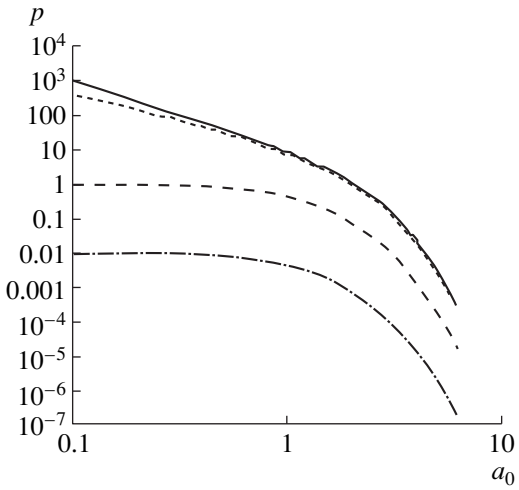

Fig. 5. Electrostatic pressure p vs. the plane half-spacing a_0 at $\delta = 1$ and (solid curve) $\varphi_0 \longrightarrow \infty$ and $n_{e0} \longrightarrow \infty$, (dotted curve) $\varphi_0 = 7$ and $n_{e0} = 10^3$, (dashed curve) $\varphi_0 = 1$ and $n_{e0} = 2.7$, and (dot-and-dash curve) $\varphi_0 = 0.1$ and $n_{e0} = 0.1$.

Conclusion

Thus, the electrostatic interaction between charged planes (either surrounded by an electron cloud or immersed into a plasma) causes the mutual repulsion of these planes. At the same time, numerical calculations [8] showed that, in the case of spherical particles, we must observe attraction. This effect is probably caused by the following two circumstances. First, in the two-dimensional problem, we neglect the flow of electrons from peripheral to central region along the axis connecting the dust particles. Second, the force of interaction between charged particles (with no charges in the environment) is independent of the plane spacing, whereas the force of interaction of charged spheres is inversely proportional to the squared spacing between these spheres. Therefore, the electrons accumulated at approximately one-half of the distance between the dust particles have a larger effect on the interaction of spherical particles that on the interaction of charged planes. In any case, the problem of interaction of finite-size particles in an electron cloud or in a plasma requires additional investigation.

REFERENCES

1. V. E. Fortov, A. P. Nefedov, O. F. Petrov, *et al.*, Zh. Éksp. Teor. Fiz. **111** (2), 467 (1997) [JETP **84**, 256 (1997)].
2. A. N. Tkachev and S. I. Yakovlenko, Zh. Tekh. Fiz. **69** (1), 53 (1999) [Tech. Phys. **44**, 48 (1999)].
3. S. I. Yakovlenko, Pis'ma Zh. Tekh. Fiz. **26** (8), 47 (2000) [Tech. Phys. Lett. **26**, 337 (2000)].
4. V. E. Fortov, V. I. Vladimirov, L. V. Deputatova, *et al.*, Dokl. Akad. Nauk **336** (2), 184 (1999) [Dokl. Phys. **44**, 279 (1999)].
5. S. I. Yakovlenko, Kratk. Soobshch. Fiz. (2001) (in press).
6. B. V. Derjaguin and L. D. Landau, Acta Physicochim. URSS **14** (6), 633 (1941).
7. D. V. Sivukhin, in *Reviews of Plasma Physics*, Ed. by M. A. Leontovich (Atomizdat, Moscow, 1964; Consultants Bureau, New York, 1968), Vol. 4.
8. S. I. Yakovlenko, Pis'ma Zh. Tekh. Fiz. **25** (16), 83 (1999) [Tech. Phys. Lett. **25**, 670 (1999)].

Translated by A. Kondrat'ev

Technical Physics Letters, Vol. 27, No. 5, 2001, pp. 394–397. Translated from Pis'ma v Zhurnal Tekhnicheskoĭ Fiziki, Vol. 27, No. 10, 2001, pp. 1–8.

Low-Temperature (T = 250–400 K) Oxygen Adsorption on $YBa_2Cu_3O_{6.9}$ Ceramics

V. N. Kuznetsov

Institute of Physics, St. Petersburg State University, St. Petersburg, Russia

e-mail: kuznets@photonics.phys.spbu.ru

Received October 30, 2000

Abstract—Oxygen adsorption on $YBa_2Cu_3O_{6.9}$ ceramics at T = 250–400 K was studied by thermal desorption (TD) mass spectrometry. It was established that, depending on the adsorption temperature (T_a), oxygen occurs on the substrate surface either in two forms (γ1 and γ2, for T_a < 350 K) or in a single form (γ2, for $T_a \geq 350$ K). In the TD spectrum, γ1 adsorbed oxygen species are manifested by a peak with a maximum at T_{max} = 330–340 K. When the adsorption temperature increases from 290 to 400 K, the TD peak of γ2 oxygen species shifts from $T_{max} \approx 380$ K to 440 K, which is accompanied by a decrease in the temperature "boundary" for the desorption of structural oxygen. In addition, γ2 oxygen species are capable of participating in isotope exchange with the oxygen of the ceramics. For both forms of adsorbed oxygen, TD most probably proceeds by the associative mechanism with an activation energy of 0.63 ± 0.08 eV (γ1) and 1.13 ± 0.02 eV (γ2). A model qualitatively explaining oxygen sorption in ceramics is proposed, according to which γ2 species are formed in the initial adsorption stage. © *2001 MAIK "Nauka/Interperiodica".*

Increasing the stability of high-temperature superconducting materials based on $YBa_2Cu_3O_x$ (YBCO) ceramics depends on the knowledge of mechanisms of processes occurring in the oxygen subsystem. Some phenomena related to a decrease in the temperature of transition to the superconducting state (T_c) upon the "low-temperature" ($T \leq 500$ K) treatments are still given no exhaustive explanation. For example, exposure of the epitaxial YBCO films at 450 K in O_2 at a pressure of p = 10 Pa [1] or the exposure of the ceramics at 473 K in vacuum [2] can lead to a 7–10 K decrease the T_c value. Kalanov *et al.* [2] explained this effect by a decrease in the oxygen concentration in the boundary layers of various submicron structures (grains, twins, blocks). At the same time, heating the freshly prepared YBCO films in this temperature region is accompanied by the absorption of oxygen [3].

The nature and properties of oxygen occurring at the structural boundaries inside YBCO and at the ceramic–gas phase interface are still insufficiently studied [4]. This situation is explained by the fact that data on the state of oxygen adsorbed on single crystals cannot be obtained because of their small surface area. In the investigations of YBCO powders, ceramics, and films, the main effort is devoted to the study of sorption and the desorption of structural oxygen, the first peak of which in the TD spectra of ceramics is observed at ~750 K [5, 6]. Because of the lack of data concerning the oxygen adsorption, we studied the adsorption–desorption process in the O_2–YBCO system by TD mass spectrometry.

The experimental setup comprised an MI-1201 mass spectrometer equipped with a VEU-1 secondary-electron multiplier, an ultrahigh-vacuum system, a data acquisition system, and a programmed sample heating system. A sample of the YBCO ceramics with a diameter of 9.3 mm and a thickness of 2.2 mm was placed into a flat-wall quartz cell so as to ensure a reliable thermal contact between the sample and the cell walls. A low-inertia heater ensured sample heating at a constant rate β = 0.1–0.25 K/s in the temperature range from 250 to 1000 K. In the 250–275 K interval, the sample temperature was stabilized by cooled ethyl alcohol. Oxygen with the natural isotope composition and that enriched with the O^{18} isotope was purified by diffusion through walls of a silver capillary and adsorbed at a pressure in the range from 4×10^{-2} to 1.6×10^2 Pa.

The experiments were performed using samples of the $YBa_2Cu_3O_x$ ceramics with x = 6.9 and a specific area of 220 cm^2/g synthesized in the Institute of Physics (St. Petersburg State University) by sintering oxide powders. In order to remove the traces of H_2O, CO, CO_2, and other contaminants, the sample was heated in a vacuum at 520 K for no less than 10 h. After this pretreatment, the TD spectra measured below 530 K exhibited only the peak of structural oxygen with a desorption rate monotonically increasing with temperature in the 480–530 K interval. The total amount of structural oxygen released during a single measurement did not exceed $10^{-5}\%x$, so that repeated TD cycles virtually did not change the bulk oxygen content in the sample studied.

1063-7850/01/2705-0394$21.00

Figure 1 shows typical TD spectra of oxygen adsorbed at 290 K (curves *1* and *2*). The TD peak shape and position (T_{max}) depend on the temperature of oxygen adsorption (T_a). For T_a = 250–275 K, the TD spectrum displays two peaks with the halfwidth of $\Delta T \approx$ 40 K and T_{max} values differing by no more than 30 K (Fig.1, curves *3* and *4*). As the adsorption temperature T_a increases from 250 to ~310 K, the total oxygen coverage θ increases by no more than 25%, while the high-temperature component contribution increases more than two times. As a result, the two components are not resolved in the TD spectrum corresponding to T_a = 290 K (Fig.1, curves *1* and *2*). When the adsorption temperature increases to T_a = 350–400 K, only a single peak with $\Delta T \approx$ 35 K is observed in the TD spectrum, the maximum of which shifts toward high temperatures depending on T_a (Fig.1, curves *5* and *6*). In addition, the sample corresponding to T_a = 400 K shows a reduction in θ and a decrease (by 10–15 K) in the "boundary" (onset) temperature of the structural oxygen desorption (Fig.1, curve *6*). The amount of gas absorbed by the sample at 400 K exceeds the amount absorbed at 290 K by a factor of ≥1.7, while the adsorption coverage θ drops by a factor of ~2.5 (Fig.1, curves *1* and *6*).

The above results allow us to conclude that the adsorption of O_2 at T_a < 350 K leads to the appearance of two forms of adsorbed species (γ1 and γ2) corresponding to the TD peaks with T_{max} = 330–340 and ~380 K. An increase in the contribution of the γ2 form accompanying the T_a growth from 250 to 310 K suggests that the adsorbed species may partly transform from the γ1 to γ2 form. At T_a > 350 K, only γ2 adsorbed species are formed. This form is capable of partly converting into a state similar to that of structural oxygen, which is manifested by a shift of the structural oxygen desorption boundary (O_{st}). The sequence of processes accompanying the low-temperature adsorption of O_2 on YBCO ceramics can be described by the following scheme: $(O_2)_g \longrightarrow \gamma 1 \longrightarrow \gamma 2 \longrightarrow O_{st}$.

Direct evidence for the $\gamma 2 \longrightarrow O_{st}$ transition was obtained in experiments with the adsorption of oxygen enriched with an O^{18} isotope (α denoting the degree of enrichment). Initially, O_2 was in equilibrium with respect to the homomolecular exchange, as described by the parameter y = 0 [$y = (C_{34})^* - (C_{34})_0$, where $(C_{34})^*$ and $(C_{34})_0$ are the equilibrium (homomolecular exchange) and initial concentrations of $O^{16}O^{18}$ molecules]. As is seen from Fig. 1 (curves *7* and *8*), the relative degree of enrichment in the temperature region of γ2 desorption (on the high-temperature wing of the TD spectrum) is $\alpha/\alpha_0 < 1$, while $y > 0$. According to [7], this variation of the system parameters indicates that adsorbed O_2 molecules exchange two atoms with the surface oxygen. This process takes place when the atomic exchange upon the dissociative adsorption stage proceeds at a much higher rate than the rate of associative desorption.

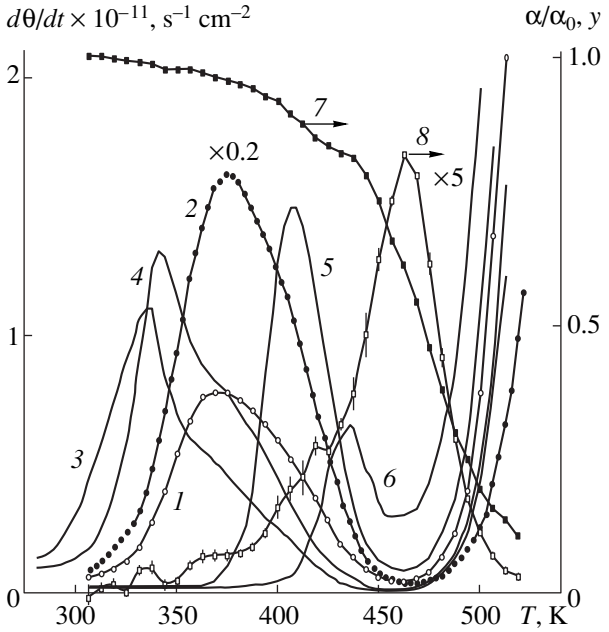

Fig. 1. (*1–6*) Thermal desorption spectra of oxygen adsorbed on $YBa_2Cu_3O_{6.9}$ ceramics under various conditions and the plots of (*7*) relative degree of enrichment α/α_0 and (*8*) parameter y of desorbed gas versus temperature (see the text for explanations). Oxygen adsorption conditions (temperature, K; pressure, Pa; exposure, min): (*1*) 290; 4×10^{-2}; 14; (*2*) 290; 1.6×10^2; 75; (*3*) 250; 13; 10; (*4*) 275; 13; 10; (*5*) 352; 4×10^{-2}; 22; (*6*) 400; 4×10^{-2}; 22; (*7, 8*) 290; 13; 20; heating rate β = 0.167 (*3, 4*), 0.25 K/s (*1, 2, 4, 6*).

In order to determine the desorption activation energy E_d for the adsorbed oxygen species, the TD data were analyzed in terms of the 1st and 2nd order desorption equations with respect to θ. For this purpose, the TD spectra were plotted in the coordinates of $\ln[(d\theta/dt)/\theta]$ ($F1$) and $\ln[(d\theta/dt)/\theta^2]$ ($F2$) versus $1/kT$ and approximated by straight lines in the interval from $1/kT_1$ to $1/kT_2$. The results of this data processing showed that a minimum error for T_a < 350 K is obtained when the plots of $F1$ and $F2$ values versus $1/kT$ are approximated by two straight segments with different slopes. The corresponding values of parameters of the desorption equations are listed in the table. As is seen from these data, both model desorption equations provide close E_d values with the same error for γ1. However, since the approximation interval for the 2nd order equation is 1.7 times greater than that for the 1st order equation (see table), the value $(E_d)_{\gamma 1} = 0.63 \pm 0.08$ eV seems to be more reliable. In the temperature region corresponding to the desorption of the γ2 oxygen form, the E_d values given by the two kinetic equations are significantly different. Since the monomolecular desorption model ($F1$) provides very low values of both E_d and the preexponential factor, we adopted the value $(E_d)_{\gamma 2} = 1.13 \pm 0.02$ eV for γ2. Thus, the associative mechanism of desorption is more likely for both forms

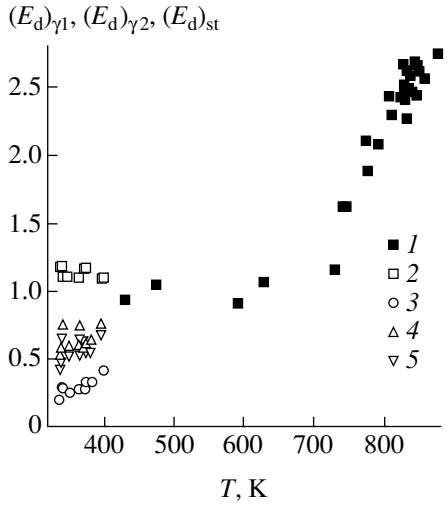

Fig. 2. A plot of the activation energy for the desorption of (*1*) structural and (*2*–*5*) adsorbed oxygen determined using model desorption kinetic equations of the (*2*, *5*) first and (*3*, *4*) second order for the (*4*, *5*) low-temperature and (*2*, *3*) high-temperature wing of the thermal desorption peak (see the text for explanations).

of adsorbed oxygen, which implies that the adsorption of oxygen is dissociative. It must be noted that, when only the peak of γ2 oxygen is observed in the TD spectrum (Fig. 1, curves *5* and *6*), the interval of linear approximation (indicated in parentheses in the table) is close to the peak width determined at the base.

The $(E_d)_{\gamma 2}$ value determined as described above was compared to the activation energy for the desorption of structural oxygen $(E_d)_{st}$ determined in the initial region (ΔT = 80–100 K) of desorption. The content of O_{st} and the boundary temperature for its desorption were altered by heating a sample for 1 h at various temperatures in a vacuum or in O_2 at $p = (1.3–40) \times 10^2$ Pa. For a reliable measurement of the kinetics of O_{st} desorption, it was sufficient to liberate an amount of oxygen not exceeding 10^{-5}% of the rated content. Therefore, it was possible to assume that the desorption rate was independent of the oxygen content and perform a linear approximation of the plot of $\ln(d\theta/dT)$ versus $1/kT$. The $(E_d)_{st}$ values are plotted in Fig. 2 (black squares), where the abscissa T indicates the center of the approximation interval. Also plotted in Fig. 2 are the E_d values for adsorbed oxygen (open symbols) used for the calculation of data in the table (here, $T = T_{max}$). For the structural oxygen with a desorption boundary in the range from 430 to 730 K, Fig. 2 yields $(E_d)_{st} = 1.04 \pm 0.05$ eV, which is close to the $(E_d)_{\gamma 2}$ value obtained within the framework of the associative desorption mechanism.

The $(E_d)_{\gamma 2}$ and $(E_d)_{st}$ values coincide (to within the error of determination) with the values of activation energy for the oxygen inward and outward diffusion in YBCO films: E_{dif} = 1.09–1.15 eV [8]. The average value of $E_{dif} = 1.2 \pm 0.07$ eV calculated using the data of review [4] is also comparable with $(E_d)_{\gamma 2}$ and $(E_d)_{st}$ estimates. According to [9, 10], the diffusion and isotope exchange of oxygen in YBCO ceramics proceed in the $CuO_{1-\delta}$ plane with $E_{dif} \approx 1.0$ eV. For $T > 730$ K, the isotope exchange activation energy increases to reach 1.65 eV (710–790 K) and 2.26 eV (790–850 K) due to the participation of oxygen from BaO and CuO_2 planes [9]. These results qualitatively agree with the increase in $(E_d)_{st}$ observed in Fig. 2 in the same temperature interval.

Thus, the high sensitivity of the experimental setup allowed the oxygen adsorption on YBCO ceramics to be followed beginning with the stage of adsorption state formation. It was established that oxygen adsorption already takes place at 250 K, possessing presumably a dissociative character. The values of $(E_d)_{\gamma 2}$ and $(E_d)_{st}$ (in the 430–730 K interval) are close to the known values of E_{dif} for oxygen in the $CuO_{1-\delta}$ planes. This fact allowed us to suggest that the γ2 form of adsorbed oxygen corresponds to an atom occupying an oxygen vacancy at the interface between the $CuO_{1-\delta}$ plane and the vacuum. Since $(E_d)_{\gamma 2} \approx E_{dif}$, we may expect (beginning with $T_a \sim 350$ K) a considerable contribution due to the inward and outward diffusion of these oxygen atoms by the $CuO_{1-\delta}$ plane. In this case, the adsorption of O_2 at $T_a > 350$ K will be accompanied by a growth in the concentration of atoms originated from adsorption in the near-surface region. In the course of desorption, this is manifested by a shift of the T_{max} value for γ2 species toward higher temperatures. After the adsorption at T_a = 400 K, the oxygen species diffusing inward will be partly desorbed together with the structural oxygen,

Desorption activation energy E_d, preexponential factor ν, and lnν determined in the interval from $1/kT_1$ to $1/kT_2$ for desorption kinetic equations of the first (*F*1) and second (*F*2) order, and assignment of these parameters to γ1 and γ2 forms of adsorbed oxygen

	E_d, eV	lnν	ν	T_1, K	T_2, K	Form
*F*1	0.57 ± 0.08	13.2 ± 0.07	5.4E5, s^{-1}	311	359	γ1
*F*2	0.63 ± 0.08	–(15 ± 1.6)	3E-7, $cm^2\ s^{-1}$	311	391	γ1
*F*1	0.29 ± 0.02	3.8 ± 0.5	4.5E1, s^{-1}	356	423	γ2
*F*2	1.13 ± 0.02	–(0.9 ± 0.1)	4E-1, $cm^2\ s^{-1}$	397	430	γ2
				(349)	(435)	

thus decreasing the temperature boundary for the structural oxygen desorption.

The proposed model qualitatively describes the initial stages of the adsorbed oxygen penetration into the near-surface layer of the $CuO_{1-\delta}$ plane. We believe that analogous low-temperature processes will probably develop at the boundaries of these planes in various submicron structures.

REFERENCES

1. Yu. N. Drozdov, S. A. Pavlov, and A. E. Parafin, Pis'ma Zh. Tekh. Fiz. **24** (1), 55 (1998) [Tech. Phys. Lett. **24**, 24 (1998)].
2. M. U. Kalanov, M. S. Paĭzullakhanov, R. Kh. Maminov, *et al.*, Pis'ma Zh. Tekh. Fiz. **23** (1), 13 (1997) [Tech. Phys. Lett. **23**, 13 (1997)].
3. S. Kitelberger, U. Bolz, R. P. Huebener, *et al.*, Physica C (Amsterdam) **312** (1–2), 7 (1999).
4. Yu. M. Baĭkov, E. K. Shalkova, and T. A. Ushakova, Sverkhprovodimost: Fiz., Khim., Tekhn. **6** (3), 449 (1993).
5. É. A. Grigor'yan, R. V. Kir'yanov, and A. G. Merzhanov, Sverkhprovodimost: Fiz., Khim., Tekhn. **5** (4), 710 (1992).
6. M. S. Hegde, Mater. Res. Bull. **23** (8), 1171 (1988).
7. V. S. Muzykantov, V. V. Popovskiĭ, and G. K. Boreskov, Probl. Kinet. Katal. **12**, 155 (1968).
8. S. Kitelberger, U. Bolz, R. P. Huebener, *et al.*, Physica C (Amsterdam) **302** (2–3), 93 (1998).
9. V. B. Vykhodets, T. E. Kurennykh, K. V. Trifonov, *et al.*, Zh. Éksp. Teor. Fiz. **106** (2), 648 (1994) [JETP **79**, 355 (1994)].
10. V. B. Vykhodets, T. E. Kurennykh, and B. V. Slobodin, Fiz. Tverd. Tela (St. Petersburg) **39** (1), 42 (1997) [Phys. Solid State **39**, 35 (1997)].

Translated by P. Pozdeev

Technical Physics Letters, Vol. 27, No. 5, 2001, pp. 398–400. Translated from Pis'ma v Zhurnal Tekhnicheskoĭ Fiziki, Vol. 27, No. 10, 2001, pp. 9–15.

On the Nature of an Anomalous RF Electromagnetic Pulse Caused by an Extensive Air Shower

A. D. Filonenko

East Ukrainian State University, Lugansk, 91034 Ukraine

e-mail: uni@vugu.lugansk.ua

Received September 20, 2000

Abstract—Theoretical estimates validating a hypothesis concerning the origin of anomalously intense RF pulses generated in extensive air showers are obtained. It is shown that these pulses are due to a quasi-coherent radiation of the transverse current of ionization electrons flowing in the shower in a 10^4–10^5 V/m field of the thunderstorm cloud. For particles with an energy of $W_0 = 10^{17}$ eV, the amplitude of the field generated by the anomalous RF pulse is on the order of 10^{-1} V/m at ~500 m from the shower axis. © *2001 MAIK "Nauka/Interperiodica".*

The fact that, under certain conditions (depending on the state of the atmosphere), an extensive air shower can generate anomalously intense radio-frequency radiation caused by a particle with the initial energy W_0 exceeding 10^{16} eV (see, e.g., [1–3]), is assumed to be reliably established. Despite numerous attempts made to discover the nature of this phenomenon, no satisfactory explanation has yet been given. It is evident that this anomalous radiation is related to the increased intensity of the field generated by atmospheric electricity under unstable weather conditions. Moreover, it is known that one of the hypotheses explaining normal radioemission is based on the mechanism involving the radiation of an electromagnetic field by excess electrons of the shower in a constant gradient of the Earth's electric potential (the so-called geoelectric hypothesis [4–6]). Therefore, it was natural to seek an explanation for the anomalous radioemission by considering this radiation mechanism in a high-intensity electrostatic field. It is known that, under bright weather conditions, the vertical gradient of the Earth's electric potential is about 100 V/m. In a thundershower, this value may be higher by two or even three orders of magnitude.

When the number of electrons in an extensive air shower is maximal, the energy γ of most of these particles is about 100 (see, e.g, [7]). Since the acceleration of charged particles in the longitudinal and transverse electric fields is proportional to γ^{-3} and γ^{-1}, respectively, the aforementioned radiation mechanism is evidently ineffective [4–6, 8, 9].

This was probably the reason for abandoning the radiation concept and assuming that the observed phenomenon is a consequence of an electric breakdown of the atmosphere along the ionization track caused by the motion of the shower disk [1]. However, simple estimates show that the intensity of the electromagnetic field generated in these cases will exceed experimental values by many orders of magnitude. For example, the amplitude of the electromagnetic pulse reported in [2] corresponds to a field intensity of about 0.05 V/m for the chosen frequency band. This value is substantially smaller than the field intensity caused by the storm discharge even at rather long distances.

The author of this paper also believes that the anomalous RF pulse is related to the high intensity of the field generated by the atmospheric electricity. However, unlike [2–6, 9], he assumes that the intense radioemission is caused by the transverse current of ionization electrons (rather than the longitudinal current of excess electrons) in the field of a thundercloud. Electrons and positrons of an extensive air shower have an energy of the order of 10^8 MeV and eventually spend this energy for the ionization or excitation of atmospheric atoms. It is known that the mean energy spent for the ionization of one atom equals approximately 30 eV.

After thermalization, the ionization electron drifts along the field lines for a time τ_a up to the instant when it attaches to a neutral molecule of oxygen. The attachment (i.e., the drift) time of a thermalized electron is on the order of 10^{-8}–10^{-7} s. Naturally, this time depends on the concentration of neutral molecules [10]. Such electron motion is just an elementary event of the anomalous radio emission of an extensive air shower.

The possibility of the transverse drift of an electron in the thundercloud field is of fundamental importance. In the aforementioned experiments, the antennas recording the radioemission were placed in the immediate vicinity of the shower axis (at a distance of about 0.2–1 km). It is also known that the space radiation pattern of a charged particle having traveled a path R_δ

1063-7850/01/2705-0398$21.00

exhibits a maximum in the plane perpendicular to the direction of propagation $\mathbf{R}_\delta$ and a zero-level minimum in this direction. This is true for wavelengths $\lambda \gg R_\delta$ and travel time $\omega\tau_a \le 1$ (see [11], p. 227). In this case, the spectral field intensity can be determined using a simple expression [12, 13]:

$$E_1(\omega) = \frac{qi\omega e^{ikR_0}R_\delta}{4\pi\varepsilon_0 c^2 R_0}\sin\alpha \ (\text{V/m Hz}), \qquad (1)$$

where q is the particle charge, ω is the frequency of the corresponding harmonic, R_0 is the distance from the observer to the charge, R_δ is the charge path length, α is the angle between the direction of propagation and the direction to the observer, $k = \omega/c$, $c = 3 \times 10^8$ m/s, and $(4\pi\varepsilon_0)^{-1} = 9 \times 10^9$ m/F.

Equation (1) shows that no radiation is emitted in the direction of $\alpha = 0$. Therefore, for an observer located near the shower axis, the most effective radiation mechanism is that related to the transverse drift of electrons. This radiation is most pronounced at $\alpha = \pi/2$. In addition, according to [14], the number of excess electrons does not exceed 10% of the total number of electrons. For example, in a shower with the energy $W_0 = 10^{17}$ eV, the total number of electrons N_0 at the maximum of the electron concentration is approximately 10^8 and, consequently, the number of excess electrons equals 10^7. The number of ionization electrons in this example is $10^{17}/30 \approx 3 \times 10^{15}$. This value is eight orders of magnitude higher than the number of excess electrons. Therefore, the radioemission caused by the ionization electrons may be substantially more effective.

In order to obtain estimates for the intensity of the electromagnetic field caused by the transverse drift of ionization electrons, we will consider the following idealized model of an extensive air shower (EAS) [15]. In this model, the EAS is an aggregate of N_0 charged particles (electrons and positrons) located in the volume of a negligibly thin disk of radius r_0, moving vertically downward at a velocity close to the speed of light ($\gamma \approx 100$). The active part of the path L of this on the whole neutral disk comprises several kilometers. Almost the entire initial energy W_0 of an EAS particle is finally spent for the ionization and excitation of atmospheric molecules.

The most intense part of the shower (where the total number of particles approaches N_0) is located at a height of several kilometers. Evidently, the elementary radiators in this model are the electrons of the ionized molecules rather than the charged particles of the shower. Upon the ionization of these molecules, which were at rest before the arrival of the shower disk, the thermalized electrons drift in the horizontal direction. In this case, for the observer located near the shower axis (see the note given above), the angle α is about $\pi/2$. The elementary radiators can be considered as virtually

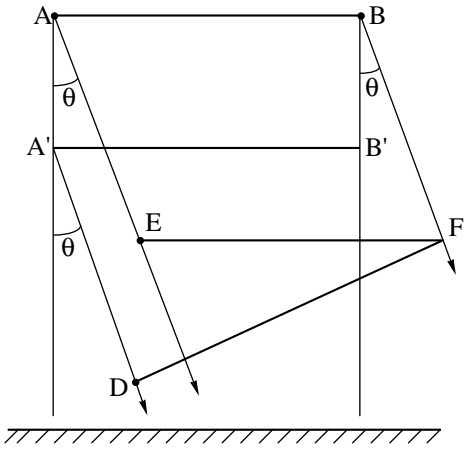

Mutual orientation of the shower disk AB (A'B'), radiation direction BF, and vertical direction AA'.

immobile in comparison with the speed of the disk, since the drift speed $v_d = qE_\perp/mv_m$ even for $E_\perp = 10^5$ V/m is only 2×10^5 m/s, which is three orders of magnitude lower than the speed of light.

Assume further that the observer is located in the wave zone; consequently, $\lambda \ll R_0$. Then, for a specified direction Θ (the angle between the shower axis and the direction $\overline{R_0}$), we can determine the frequency range $0 \le \omega \le \omega_0$ for which the phase difference $\Delta\varphi$ between oscillations arriving at the observation point from arbitrary points in the disk does not exceed π. In this case, in order to evaluate the field intensity at the observation point, we can arithmetically sum up the amplitudes of elementary harmonics (1).

The figure depicts the position of a shower disk (AB = $d = 2r_0$) at the initial time instant. A time t later, the disk will occupy position A'B', where AA' = BB' = vt and AE = BF = ct is the path traveled by the wave during this time interval in the direction Θ. At $t = 0$, the phase difference of the signals arriving from points A and B is determined only by the configuration presented in the figure and equals $d\sin\theta$. As the shower moves and the air molecules become ionized, each electron released from an atom for time τ_a becomes an elementary source of electromagnetic waves with amplitude $E(\omega)$ determined by expression (1).

For an arbitrary time instant t, when the disk is positioned at A'B', the phase difference $\Delta\varphi$ will be maximum for the wave emitted from point B at time $t = 0$ and the wave emitted from point A' at time t. One can see from the figure that $\Delta\varphi = \text{A'D}2\pi/\lambda = d\sin\Theta + ct - vt\cos\Theta$. Substituting $t = L/v$, we obtain that the frequency range $\Delta\omega = \omega_0$ is

$$\Delta\omega = \frac{\pi c}{\beta d\sin\Theta + L(1-\beta\cos\Theta)}. \qquad (2)$$

Choose, for example, $\Theta = 10°$. In this case, we can readily calculate that, for the existing isotropic spatial

distribution of the directions of cosmic rays, approximately 2% of these rays will have a direction such that an observer placed on the Earth's surface would occur within a radiation cone with the apex angle $2\theta = 20°$. Substituting typical values for $L = 3 \times 10^3$ m and $\beta = 0.9998$ (for $\gamma = 50$), $d = 2r_0 = 200$ m, and $c = 3 \times 10^8$ m/s, we obtain from formula (2) that $\Delta\omega = 10^7$ s^{-1}. For a thundercloud field $E_\perp = 10^5$ V/m, the path length $R_\delta = qE_\perp\tau_a/m\nu_m = 6 \times 10^{-2}$ m at a height of 5–6 km [16]. Here $q = 1.6 \times 10^{-19}$ C, $\tau_a = 3 \times 10^{-7}$ s, $m = 0.9 \times 10^{-30}$ kg, and $\nu_m = 0.8 \times 10^{11}$ s^{-1}.

Summing up (1) over ω from 0 to $\omega_0 = 10^7$ s^{-1} and taking into account that $\sin\alpha = \cos\Theta$ and that the total number of ionization electrons in the shower is equal to W_0/I, where $I = 30$ eV, we arrive at the following expression for the resultant amplitude:

$$E = \frac{q\omega_0^2 R_\delta W_0}{8\pi\varepsilon_0 c^2 R_0 I}\cos\Theta \text{ V/m}. \quad (3)$$

Substituting typical values of parameters and values of physical constants into formula (3), we obtain that, for a particle with energy $W_0 = 10^{17}$ eV, the field intensity E calculated at a typical distance $R_0 = 3 \times 10^3$ m equals 0.05 V/m. This value coincides with the field intensity observed in the experiments [1–3].

Since the flux of particles with the energy $W_0 = 10^{17}$ eV corresponds to approximately ten events per hour in a solid angle of 1 sr for a detector with a characteristic area of 10 km^2, for a radiation pattern beamwidth 2Θ of 20° we may expect approximately one event per hour. Therefore, it is clear that, in the presence of a thundercloud, it is highly probable that a giant RF pulse accompanying an extensive air shower will be detected. For the example considered above, it follows from (2) that the frequency range in which the total amplitude can be estimated by arithmetic summation of the elementary amplitudes (1) extends from zero up to $\nu = 1.5$ MHz. The phase difference $\Delta\varphi$ between the elementary amplitudes taken from a wider frequency range exceeds π and, consequently, brings a negative contribution to the resultant field.

In conclusion, it should be noted that the described natural phenomenon is rather similar to the process in an ionization counter. In both cases, the particle forms a track which, in the former case, causes an RF electromagnetic pulse (radio wave) in the transverse electrostatic field and, in the latter case, forms an avalanche of charged particles in the electrostatic field between the cathode and the anode. In both cases, these processes induce an electric signal at the output of a detector. Therefore, seemingly exotic (at the first glance) particle detection techniques described in [17–19] may form the basis for a new approach to the detection of high-energy cosmic rays [20]. It may be expected that the discovered mechanism of the anomalous radioemission of an extensive air shower will be of interest not only in general physics but may also aid the discovery of new approaches to solving the latter problem.

REFERENCES

1. A. V. Aleksandrov, L. T. Filimonov, *et al.*, in *Proceedings of the 20th International Cosmic Ray Conference, 1987*, Vol. 6, p. 132.
2. M. Kusunose, H. Sasaki, and T. Ogava, in *Proceedings of the 22nd International Cosmic Ray Conference, 1991*, Vol. 4, p. 359.
3. K. Suga, F. Kakimoto, and K. Nishi, in *Proceedings of the 19th International Cosmic Ray Conference, 1985*, Vol. 7, p. 268.
4. R. R. Wilson, Phys. Rev. **108**, 155 (1957).
5. W. N. Charman, Nature **215**, 497 (1967).
6. W. N. Charman and J. V. Jelley, Can. J. Phys. **46**, 216 (1968).
7. S. Z. Belen'kiĭ, *Cumulative Processes in Cosmic Rays* (OGIZ, Moscow, 1948).
8. D. R. Tompkins, Phys. Rev. D **10**, 136 (1974).
9. K. Sivaprasad, Aust. J. Phys. **31**, 439 (1978).
10. Yu. P. Raizer, *Gas Discharge Physics* (Nauka, Moscow, 1987; Springer-Verlag, Berlin, 1991).
11. L. D. Landau and E. M. Lifshitz, *The Classical Theory of Fields* (Nauka, Moscow, 1967; Pergamon, Oxford, 1975).
12. P. I. Golubnichiĭ and A. D. Filonenko, Pis'ma Zh. Tekh. Fiz. **20** (12), 57 (1994) [Tech. Phys. Lett. **20**, 499 (1994)].
13. P. I. Golubnichiĭ, A. D. Filonenko, and V. I. Yakovlev, Izv. Akad. Nauk, Ser. Fiz. **58** (12), 115 (1994).
14. G. A. Askar'yan, Zh. Éksp. Teor. Fiz. **41** (2), 616 (1961) [Sov. Phys. JETP **14**, 441 (1962)].
15. G. B. Khristiansen, G. V. Kulikov, and Yu. A. Fomin, *Cosmic Radiation of Superhigh Energy* (Atomizdat, Moscow, 1975).
16. V. L. Ginzburg, *The Propagation of Electromagnetic Waves in Plasmas* (Nauka, Moscow, 1967; Pergamon, Oxford, 1970).
17. A. D. Filonenko, Izv. Akad. Nauk, Ser. Fiz. **61** (3), 456 (1997).
18. A. D. Filonenko, Pis'ma Zh. Tekh. Fiz. **24** (24), 65 (1998) [Tech. Phys. Lett. **24**, 975 (1998)].
19. A. D. Filonenko, Pis'ma Zh. Éksp. Teor. Fiz. **70** (10), 639 (1999) [JETP Lett. **70**, 649 (1999)].
20. A. D. Filonenko, Pis'ma Zh. Tekh. Fiz. **23** (10), 57 (1997) [Tech. Phys. Lett. **23**, 399 (1997)].

Translated by A. Kondrat'ev

Technical Physics Letters, Vol. 27, No. 5, 2001, pp. 401–402. Translated from Pis'ma v Zhurnal Tekhnicheskoĭ Fiziki, Vol. 27, No. 10, 2001, pp. 16–19.

Features of Explosive Electron Emission from a Multipoint Liquid-Metal Emitter

O. P. Korovin, S. S. Karatetskiĭ, E. O. Popov, and V. N. Shrednik

Ioffe Physicotechnical Institute, Russian Academy of Sciences, St. Petersburg, 194021 Russia

e-mail: korovin@ssdkorovin.ioffe.rssi.ru

Received January 9, 2001

Abstract—A multipoint liquid-metal (MLM) emitter operating in the explosive regime is characterized by a significantly greater working capacity than solid-state explosive cathodes. The MLM emitter described is capable of producing a series of blow-up emission pulses with a repetition period from 25 μs to 1 ms controlled by external circuit parameters. The high stability of the MLM emitter operation is explained by the explosive emission taking place simultaneously from several hundreds of emitting points. *© 2001 MAIK "Nauka/Interperiodica".*

The study of liquid-metal emitters operating in the explosive emission regime, despite the obvious advantages of such sources, does not attract the attention of researchers. As a rule, investigations of the liquid-metal emitters are restricted to the field emission regime, and the measurements are terminated on approaching the region of voltages corresponding to the explosion development. Among recent publications, an exception is offered by the results reported in [1], where the study of emission from a single point was followed by an attempt at creating a system of several liquid-metal emitting points.

Below we report on the features of explosive emission from a multipoint liquid-metal (MLM) gallium emitter operating in the explosive regime. The emitter is analogous to that described previously [2], representing a layer of liquid gallium covered with a 10-μm-thick Lavsan (Dacron) track membrane with 0.4-μm holes. The hole density was 10^7 cm^{-2}. Figure 1 shows schematic diagrams of the emitter surface and the measuring circuit. The MLM emitter operation in the explosive emission mode was studied for different shapes of the supply voltage: (i) a 50-Hz sinusoid half-wave and (ii) a saw-tooth voltage with a period varied from 1 Hz to 1 kHz.

The blow-up current pulse was detected by a collector and measured with a Faraday cup. The voltage signal was transmitted via a coaxial cable and an attenuator to an S7-19 oscillograph possessing a frequency band of 5 GHz. The pattern observed on the oscillograph display was manually scanned and the data transferred from the scanner to a personal computer for sub-

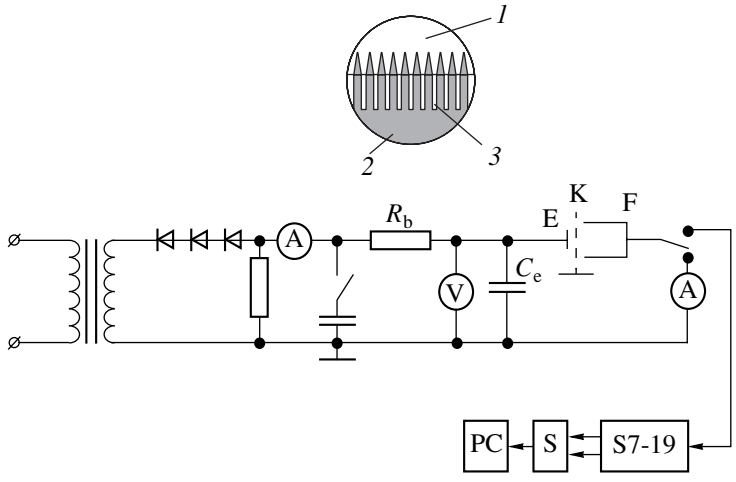

Fig. 1. Schematic diagrams of the multipoint liquid-metal emitter surface and the measuring circuit: (*1*) vacuum; (*2*) liquid metal; (*3*) track membrane; (R_b) ballast resistance controlling the repetition frequency of emission pulses; (C_e) stray capacitance of the circuit; (E) emitter; (K) grid collector; (F) Faraday cup; (S) manual scanner; (PC) personal computer.

1063-7850/01/2705-0401$21.00 © 2001 MAIK "Nauka/Interperiodica"

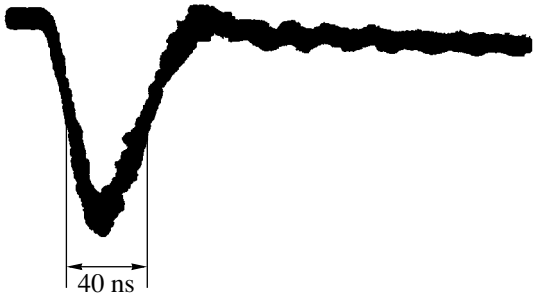

Fig. 2. A typical integrated oscillogram of the explosive emission current pulse.

sequent processing. This registration method allowed us to exclude an expensive fast-response analog-to-digital converter that might be readily damaged by the signal studied. On the other hand, this method of data transfer to the computer was faster than that employing photographic registration, followed by unavoidable scanning of the photographs. The method employed for registration of the explosive emission current pulse ensured that an "integrated" signal was obtained resulting from superposition of approximately 500 pulses during a scanning time of 10 s. Smearing the image allowed us to judge the reproducibility of the explosive emission pulses.

Figure 2 shows a typical integrated oscillogram of the explosive emission current pulse. The current pulse duration depends on the energy stored in the capacitor C_e representing a mounting capacitance of the emitter circuit. Connecting a static voltmeter with an input capacitance of 20 pF produced a 5 ns increase in the pulse duration (FWHM). An analysis of the emitter blow-up pulse shape showed that the leading front duration is equal to the current pulse duration in the Faraday cup, measured at the pulse base. Thus, the system measures the time of electron component pumping from the plasma formed during the explosive emission.

For the MLM emitter operation in the explosive regime, it is necessary that the electric field strength exceed a certain threshold level. By our data, the interval of the threshold voltage variation is as small as 0.02%. This fact indicates that MLM emitters can be used as a base of voltage limiters with an operation time on the order of one nanosecond, provided that measures are taken to reduce the mounting capacitance value (C_e). By varying R_b (see Fig. 1), it is possible to control the time of system readiness upon the arrival of the first limiting pulse. In the regime of MLM emitter operation supplied with a 50-Hz sinusoid halfwave of increasing amplitude, it was possible to obtain the explosive emission pulse on each halfwave peak. Further increase in the high-voltage transformer output signal amplitude led to the appearance of second, third, and so on blow-up pulses following one another at a certain interval. The minimum interval was determined by the time required to charge the C_e capacitance. In our scheme, this interval could be varied from 25 μs to 1 ms by changing R_b.

The MLM emitter described exhibited stable operation without significant changes in the field emission characteristics for several tens of hours. In the explosive emission regime, no changes in the blow-up pulse parameters with a current amplitude of up to 50 A were observed after producing 10^7 pulses. We believe that the stable and reproducible emitter operation is ensured by the blow-up emission taking place simultaneously from several hundreds of emitting points. This is confirmed by the fact that a negative charge ejected in a single pulse was on the order of 6×10^{-7} C, which corresponds to not less that 3.75×10^{12} singly ionized plasma atoms. The total mass of these atoms is more than 50 times the mass of a single liquid gallium tip.

Obvious advantages of MLM explosive and field emitters include the very large number of emitting points, the stable shape of these points determined by a balance of surface tension and electric field strength, recovery of the emitter surface upon the point blow-up, and insensitivity to ion bombardment. All these properties were clearly manifested in the experiment.

Acknowledgments. This study was supported by the Russian Foundation for Basic Research, project no. 98-02-18414.

REFERENCES

1. G. N. Fursey, L. A. Shirochin, and L. M. Baskin, J. Vac. Sci. Technol. **15** (2), 410 (1997).
2. O. P. Korovin, E. O. Popov, V. N. Shrednik, and S. S. Karatetskiĭ, Pis'ma Zh. Tekh. Fiz. **25** (8), 39 (1999) [Tech. Phys. Lett. **25**, 310 (1999)].

Translated by P. Pozdeev

Technical Physics Letters, Vol. 27, No. 5, 2001, pp. 403–405. Translated from Pis'ma v Zhurnal Tekhnicheskoĭ Fiziki, Vol. 27, No. 10, 2001, pp. 20–25.

Nonlinear Microwave Spin Wave Interferometer

A. B. Ustinov and B. A. Kalinikos

St. Petersburg State Electrotechnical University, St. Petersburg, Russia

e-mail: eivt@eltech.ru

Received December 26, 2000

Abstract—The characteristics of a nonlinear microwave spin wave interferometer were experimentally studied for the first time. The interferometer was implemented according to a bridge scheme with a nonlinear spin wave phase shifter based on an yttrium-iron garnet film. The maximum sensitivity of the nonlinear interferometer with respect to the input signal level was reached with a phase shifter operating on the forward volume spin waves. In the GHz frequency range, an increase in the microwave power up to a few mW led to a signal phase shift exceeding 180°. © *2001 MAIK "Nauka/Interperiodica".*

The linear and nonlinear phenomena accompanying the propagation of microwave spin waves in ferromagnetic films were studied from the standpoint of both fundamental science and applications. Despite a large variety of existing thin-film spin wave devices (see, e.g., [1, 2]), the possibilities of creating new systems for the microwave signal processing with the aid of spin waves are by no means exhausted. In particular, an interesting technological task is to develop a spin wave interferometer analogous to the integral optical Mach–Zehnder interferometer employed in a large number of optical devices [3]. Recently, Fetisov and Patton described a linear spin wave interferometer for use in bistable microwave devices [4]. However, a nonlinear spin wave interferometer would expand the possibilities of signal processing directly at microwave frequencies.

The purpose of this work was to study the characteristics of a nonlinear microwave spin wave interferometer with a nonlinear element representing a thin-film spin wave phase shifter.

Figure 1 presents a schematic diagram of an experimental prototype of the nonlinear spin wave interferometer. The device implements a bridge scheme with two arms. The first arm comprises a spin wave phase shifter, with the output signal phase shift depending on the amplitude. The second (reference) arm contains a variable attenuator. The experimental system was designed so as to provide for the possibility of using phase shifters operating on various types of spin waves.

Each nonlinear phase shifter had the form depicted in Fig. 1. The spin waves were excited using microstrip transducers *1* with a length of 2 mm and a width of 50 μm deposited onto an 0.5-mm-thick aluminia (polycor) substrate. The transducers were supplied via microstrip lines with a wave impedance of 50 Ω. Phase shifter *4* represented an epitaxial yttrium-iron garnet (YIG) film *2* grown on a gadolinium–gallium garnet substrate *3*. The YIG film was placed and fixed directly on the microstrip transducers. The phase shifter was exposed to a constant magnetic field generated by an electric magnet. The magnetic field direction could be changed.

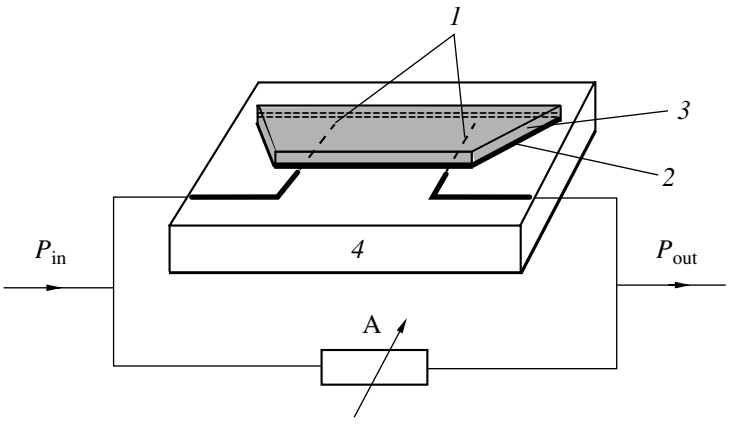

Fig. 1. A schematic diagram of the nonlinear spin wave interferometer (see the text for explanations).

1063-7850/01/2705-0403$21.00 © 2001 MAIK "Nauka/Interperiodica"

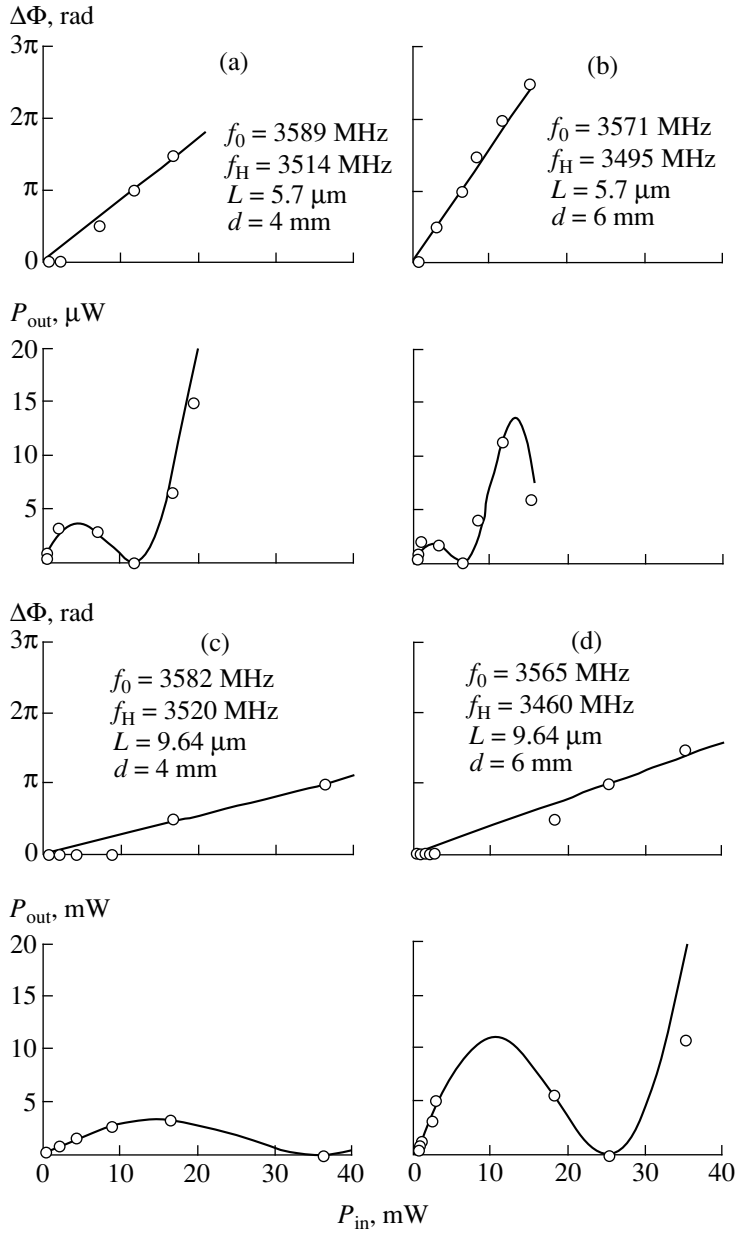

Fig. 2. Phase (top) and amplitude (bottom) characteristics of various nonlinear spin wave interferometers. Points present the experimental data, solid lines show the results of model calculations.

The experiments were carried out using phase shifters with the microstrip transducers spaced by $d = 4$ or 6 mm, which were based on single-crystal YIG films with a thickness L of 5.7 or 9.64 μm. The measurements were performed for the spin waves of three types (forward volume, backward volume, and surface spin waves) most frequently used in experimentation.

The principle of the operation of a nonlinear interferometer is based on the interference of high-intensity spin waves and on a nonlinear shift of their frequencies accompanying variation of the wave amplitudes. The nonlinear shift of the wave frequency is caused by a decrease in the constant magnetization component accompanying an increase in the alternating component. At a constant frequency, a shift of the dispersion curve caused by the decrease in the constant magnetization component leads to a change in the wavenumber and, hence, in the phase of the spin wave at the phase shifter output. Thus, a change in the input power level leads to a change in the phase shift between signals traveling in different arms of the interferometer.

Using a variable attenuator, we may readily change the ratio of amplitudes of the signals arriving from different arms to the interferometer output. Selecting the attenuation coefficient so as to ensure that the signals from the two arms arrive at the output with equal ampli-

tudes, we will obtain a zero output signal provided that the two components have opposite phases.

The results of our experiments showed, in agreement with simple physical considerations, that the maximum sensitivity with respect to the input signal level is offered by a nonlinear interferometer with a phase shifter operating on the forward volume spin waves. Figures 2a–2d show the plots of phase difference $\Delta\Phi$ (top parts) and output power P_{out} (bottom parts) versus input microwave signal power P_{in}. Points represent the experimental data and solid lines show the results of numerical modeling. The theoretical characteristics were modeled based on the dispersion law of the forward volume spin waves [2], which was used to derive an expression describing a change Δk in the wavenumber of the spin wave with increasing amplitude. Using this expression, we calculated $\Delta\Phi$ as a function of the squared spin wave amplitude (proportional to the microwave power). In these calculations, we also took into account that the spin wave amplitude decreases (as a result of relaxation) during the wave propagation and, hence, the resulting phase shift $\Delta\Phi$ is an integral characteristic.

In order to compare the theory with experiment, we used two fitting parameters, representing the coefficients of proportionality between the microwave power and the squared normalized spin wave amplitude at the interferometer input and output (denoted by ζ and ξ, respectively). Upon accomplishing the fitting procedure, these parameters were found to be $\zeta = 2.6$, $\xi = 8.7 \times 10^{-3}$ (for the experimental data presented in Fig. 2a); $\zeta = 1.6$, $\xi = 10.9 \times 10^{-3}$ (for Fig. 2b); $\zeta = 6.2$, $\xi = 2.9 \times 10^{-3}$ (Fig. 2c); and $\zeta = 5.4$, $\xi = 21.5 \times 10^{-3}$ (Fig. 2d). As can be seen from Figs 2a–2d, these values of the fitting parameters ensure a good agreement between experiment and theory. The input microwave power, for which the phase shift reaches 180°, varies from a few mW to several tens of mW depending on the nonlinear interferometer design.

An analysis of the interferometer characteristics shows that an increase in the film thickness leads to a decrease in the slope of the $\Delta\Phi(P_{in})$ plot. This result is related to the fact that spin waves propagating in a thicker film possess a higher group velocity. Therefore, for the same nonlinear frequency shift, the wavevector of a spin wave propagating in a thick film would exhibit a smaller change than in a thin film. An increase in the distance between the transducers leads to a growth in the slope of the plot of phase shift versus input microwave power $\Delta\Phi(P_{in})$. This is readily explained since, with neglect of the wave attenuation, the change in the spin wave phase shift is $\Delta\Phi = d\Delta k$. The plots in Fig. 2 show that the microwave signal at the interferometer output is zero for the input signal power corresponding to a phase shift of 180°. This condition corresponds to the complete suppression of the input signal in the interferometer.

The results of our investigation showed that, upon properly selecting the operation parameters and the spin wave phase shifter design, we may obtain various types of interferometer transmission characteristics. The nonlinear spin wave interferometer may find application in various fields, for example, this device can be used in frequency selective limiters and signal-to-noise enhancers.

REFERENCES

1. J. D. Adam, D. M. Back, K. M. S. V. Bandara, *et al.*, *Physics of Thin Films. Thin Films for Advanced Electronics Devices* (Academic, New York, 1991).
2. S. A. Baruzdin, Yu. V. Egorov, B. A. Kalinikos, *et al.*, *Functional Devices of Signal Processing (Fundamentals of Theory and Algorithms)* (Radio i Svyaz', Moscow, 1997).
3. A. S. Semenov, V. L. Smirnov, and A. V. Shmal'ko, *Integrated Optics for Data Transfer and Processing Systems* (Radio i Svyaz', Moscow, 1990).
4. Y. K. Fetisov and C. E. Patton, IEEE Trans. Magn. **35** (2), 1024 (1999).

Translated by P. Pozdeev

Technical Physics Letters, Vol. 27, No. 5, 2001, pp. 406–407. Translated from Pis'ma v Zhurnal Tekhnicheskoĭ Fiziki, Vol. 27, No. 10, 2001, pp. 26–30.

Nano- and Microsecond Laser Pulse Confinement in Compensated Gallium Arsenide

I. V. Bagrov, A. P. Zhevlakov, and A. I. Sidorov

Institute of Laser Physics, St. Petersburg, Russia

Received December 7, 2000

Abstract—Experimental data on the nano- and microsecond pulsed laser radiation ($\lambda = 1.315$ μm) confinement in compensated GaAs are reported. There are three regions of confinement, which are controlled by radiation self-defocusing due to single-photon absorption by deep impurity levels, self-defocusing due to two-photon absorption, and self-focusing caused by thermal dynamic lens formation. © *2001 MAIK "Nauka/Interperiodica".*

The phenomenon of laser radiation confinement due to self-focusing as a result of two-photon absorption in semiconductors was extensively studied (see, e.g., [1–3]). However, most of the experimental and theoretical results were obtained for a picosecond interval of the laser pulse durations, in which the influence of a number of factors (including the recombination and diffusion of charge carriers and the temperature of the medium) on this phenomenon is negligibly small. These limitations allowed very low energy thresholds (down to 10 nJ) for the confinement effect to be obtained in some semiconductors (ZnSe, GaAs, Si) [3]. Below we present experimental data on the laser radiation confinement in doped GaAs for $\lambda = 1.315$ μm in the case of nano- and microsecond pulse durations.

The optical confinement scheme comprised two glass lenses with the focal lengths of $F1 = 11$ cm and $F2 = 12$ cm and a 6-mm diaphragm situated at a distance of 41 cm from the second lens (see the inset in Fig. 1a). A nonlinear element, representing a 2-mm-thick plate of GaAs ($\rho \approx 1$ MΩ cm) without antireflection coatings was placed in the common focal plane of both lenses. The source of radiation was a photodissociated iodine laser with $\lambda = 1.315$ μm and a laser pulse base width of 50 ns in the *Q*-switched operation mode. In the free lasing mode, the pulse base width increased up to 6 μs. All experiments were carried out at room temperature.

Figure 1 shows plots of the radiation energy at the confinement system output versus the input energy for a laser pulse duration of $\tau = 50$ ns. As is seen, the doped GaAs crystal studied exhibits three regions of confinement characterized by the threshold energies $Q_{thr} \approx 0.5$ μJ (Fig. 1a), 100 μJ (Fig. 1b), and 2.5 mJ (Fig. 1c). These confinement regions are separated by intervals where the Q_2 versus Q_1 plots are almost linear. Figure 2 shows the confinement characteristics measured for a laser pulse duration of $\tau = 6$ μs. Here, there are only two confinement regions with $Q_{thr} \approx 15$ μJ (Fig. 2a) and 500 μJ (Fig. 2b); for $Q < 15$ mJ, the plot of Q_2 versus Q_1 is linear.

In order to analyze the experimental data, we have estimated the energy thresholds for confinement by the two-photon absorption mechanism with an allowance for thermal effects. The calculation was performed

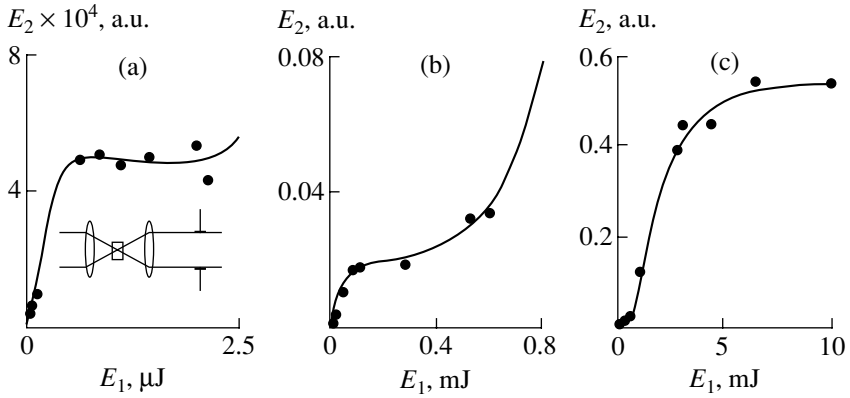

Fig. 1. The plots of energy output versus input illustrating the pulsed laser radiation confinement in doped GaAs for $\tau = 50$ ns. The inset shows the optical scheme.

1063-7850/01/2705-0406$21.00 © 2001 MAIK "Nauka/Interperiodica"

using a two-photon absorption coefficient of GaAs equal to $\beta = 0.06$ cm/MW at $\lambda = 1.06$ μm [4] and the temperature coefficient of the refractive index $dn/dT = +1.6 \times 10^{-4}$ K^{-1} [5]. As is known, doped GaAs is characterized by deep impurity levels at a distance of $\Delta E = 0.3$–0.7 eV from the bandgap edge [6]. These levels serve as the traps of charge carriers, thus rendering the crystal a semiinsulator. Upon the absorption of photons with $h\nu > \Delta E$, the trapped carriers pass from bound to free state. An increase in the carrier concentration leads to the formation of a negative dynamic lens in the region of absorption, which results in radiation defocusing. This effect accounts for the confinement with $Q_{thr} \sim 0.5$ μJ for $\tau = 50$ ns and with $Q_{thr} = 15$ μJ for $\tau = 6$ μs.

It is the single-photon nature of the process of absorption on the impurity centers that accounts for the very low confinement threshold. The absorption process, despite its linear character, gives rise to a nonlinear optical effect of the radiation confinement. This is related to the nonlinearity of the dynamic lens, the properties of which are determined by the ratio of the rates of carrier generation and trapping (the reverse process) and by the process of carrier diffusion. The process of radiation confinement caused by absorption on the impurity centers terminates when all carriers trapped in the region of radiation absorption pass to the free state.

The confinement with $Q_{thr} = 100$ μJ for $\tau = 50$ ns and with $Q_{thr} = 500$ μJ for $\tau = 6$ μs are related to radiation self-defocusing caused by a two-photon absorption. This effect was considered in detail [1–3] for picosecond laser pulses. A special feature of the nano- and microsecond laser pulses is that the pulse duration becomes comparable with or greater than the lifetime of nonequilibrium carriers. This leads to an increase in the confinement threshold for the two-photon absorption. Another feature is that the confinement process is significantly influenced by thermal effects because the laser pulse duration is sufficient for the energy transfer from the excited electron subsystem to the crystal lattice. In GaAs possessing $dn/dT > 0$, this leads to the formation of a positive dynamic thermal lens partly compensating for the negative lens effect and decreasing the dynamic range of confinement.

As is seen from Fig. 1c for $\tau = 50$ ns, radiation self-focusing on the positive thermal lens under the condition $F2 > L$ leads to the appearance of the third confinement region with $Q_{thr} = 2.5$ mJ. This region is absent for $\tau = 6$ μs because a considerable amount of heat is lost during this time from the region of pulse action and the resulting weak thermal lens may only compensate for the negative lens, which is manifested in the increasing slope of the Q_1 versus Q_2 plot (Fig. 2b). In this analysis, we did not take into account the possible dependence of confinement on the electrooptical effect in GaAs. The outdiffusion of nonequilibrium carriers from the region of pulse action may lead to a change in the refractive index caused by the electrooptical effect in the internal electric field. The influence of this phenomenon on the confinement process requires separate consideration.

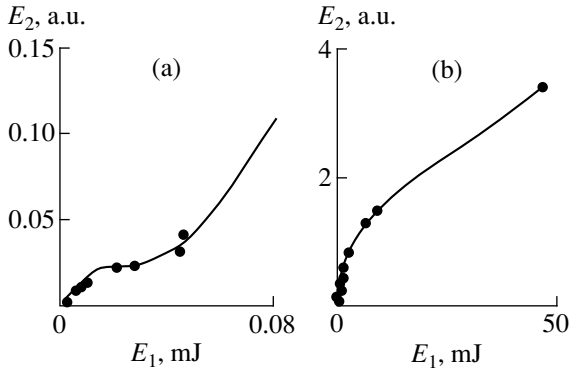

Fig. 2. Radiation confinement in doped GaAs for $\tau = 6$ μs.

Thus, we have established that the single-photon absorption on deep impurity levels in doped GaAs makes it possible to significantly reduce the radiation confinement threshold even for microsecond laser pulses. For nanosecond pulses, an additional confinement region appears (provided that $F2 < 1$) due to radiation self-focusing on a thermal dynamic lens.

Acknowledgments. This study was supported by International Science and Technology Center, project no. 1454.

REFERENCES

1. T. F. Boggess, S. C. Moss, I. W. Boyd, *et al.*, Opt. Lett. **9** (7), 291 (1984).
2. J. A. Hermann, J. Opt. Soc. Am. B **1** (5), 729 (1984).
3. E. W. van Stryland, Y. Y. Wu, D. J. Hagan, *et al.*, J. Opt. Soc. Am. B **5** (9), 1980 (1988).
4. A. Azema, J. Botineau, F. Gires, *et al.*, J. Appl. Phys. **49** (1), 24 (1978).
5. *Industrial Lasers. A Handbook*, Ed. by G. A. Abil'siitov (Mashinostroenie, Moscow, 1991), Vol. 2.
6. *Gallium Arsenide. Synthesis and Properties*, Ed. by F. P. Kesamanly and D. N. Nasledov (Nauka, Moscow, 1973).

Translated by P. Pozdeev

Technical Physics Letters, Vol. 27, No. 5, 2001, pp. 408–410. Translated from Pis'ma v Zhurnal Tekhnicheskoĭ Fiziki, Vol. 27, No. 10, 2001, pp. 31–36.

Fullerenes Obtained during Graphite Evaporation with Stationary CO_2 Laser Radiation

D. V. Afanas'ev, G. A. Baranov, A. A. Belyaev, G. A. Dyuzhev, and A. K. Zinchenko

Ioffe Physicotechnical Institute, Russian Academy of Sciences, St. Petersburg, 194021 Russia
Laser Research Center, Efremov Institute of Electrophysical Equipment, St. Petersburg, Russia
Received December 22, 2000

Abstract—Fullerenes were obtained for the first time during the evaporation of a graphite target irradiated with a high-power continuous laser. The laser and arc fullerene synthesis processes are compared. © *2001 MAIK "Nauka/Interperiodica".*

The first fullerenes were obtained by the laser evaporation of graphite [1] using focused second-harmonic radiation (λ = 532 nm; pulse energy, ~30 mJ; pulse duration, 5 ns) of a Q-switched Nd:YAG laser. The process of carbon evaporation took place in a high-density flow of helium. Under these conditions, the graphite evaporation and fullerene formation processes are separated in time.

The possibility of fullerene formation during continuous graphite evaporation by a laser beam is by no means obvious. The carbon vapor and fractal soot particles, including fullerenes [2], must absorb the laser radiation. This would result, on the one hand, in only a part of the laser beam power reaching the target surface and, on the other hand, in the absorbed power heating the soot particles and, probably, destroying the fullerenes.

The experiments were performed using an electric-discharge continuous-wave flow CO_2 laser of the Slavyanka type [3] (λ = 10.6 μm; power, 1–15 kW, beam diameter, 50 mm; beam divergence, 2×10^{-3} rad). Reflected from a mirror objective with a focal distance of 435 mm, the laser beam entered through a KCl window into a cylindrical vacuum chamber with a diameter of 180 mm and length of 300 mm. Having passed through the window situated on the top flange of the chamber, the laser beam was focused on graphite cylinders of various diameters and lengths mounted on the water-cooled bottom edge. Prior to the experiments, the working chamber was evacuated to a residual pressure of 10^{-1} Torr and then filled with helium. A weak helium flow at the window surface prevented carbon soot deposition there. Upon termination of the laser-induced evaporation process, the soot was collected from the chamber walls and weighed. The content of fullerenes α in the soot was determined using a standard method based on the absorption measurements in a toluene solution [4].

Figure 1 shows the plots of the carbon soot formation rate q versus the laser radiation power. Curve *1* refers to the case when the graphite cylinder diameter was considerably greater than the laser spot diameter. In this case, the laser beam made a deep (up to 1 cm) pit in the graphite surface. Curve *2* corresponds to the case when the target and beam diameters were equal and the graphite cylinder was completely burned off. As can be seen, the q values are significantly greater in the latter case than in the former one, which is explained by different conditions of heat removal and by hindered carbon vapor escape from the deep laser pit in the former case. These conclusions were confirmed by the results of experiments with a laser beam scanning at various velocities over the graphite surface, As is seen from the data presented in Fig. 2, the q value increases with the

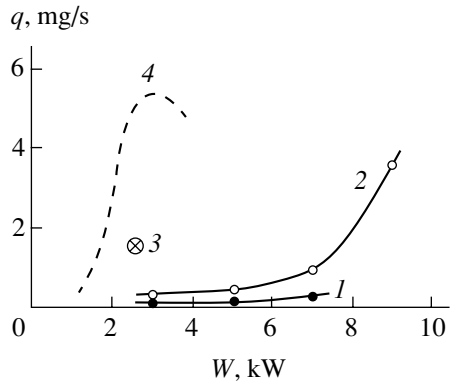

Fig. 1. Plots of the fullerene-containing soot formation rate q versus the laser radiation power W (P_{He} = 100 Torr): (*1*) graphite target of large diameter; (*2*) graphite target of small diameter; (*3*) laser beam scanning over the target surface at a velocity of 24 cm/s; (*4*) arc discharge (data from [4]).

1063-7850/01/2705-0408$21.00 © 2001 MAIK "Nauka/Interperiodica"

beam scan velocity. However, even for a maximum beam scanning velocity (ensuring the graphite evaporation from an almost flat surface, which corresponds to point *3* in Fig. 1), the relative energy consumption ("energy cost") for the soot produced by laser evaporation is higher than that for the arc discharge (see curve *4* in Fig. 1 reproducing the data from [4]).

One reason for the high "energy cost" of laser fullerenes obtained in our experiments is the laser radiation screening by torch on the zone of graphite evaporation. This is confirmed both by the strong dependence of the q value on the laser beam scanning velocity and by the results of an additional experiment in which the vacuum chamber with operating fullerene arc was illuminated with an Ar laser beam. It was found that, depending on the arc discharge regime and the distance from the arc center, the laser beam attenuation coefficient varied from 0.5 up to 1.0. Apparently, provided the removal of the carbon soot from the laser spot region was effective, the "energy cost" of laser and arc fullerenes would be equal.

The fullerene formation processes during the arc and laser evaporation of graphite may be significantly different. In the arc, the carbon vapor temperature is high and fullerenes are formed in a fan-shaped gas-plasma stream ejected from the interelectrode gap. During the laser evaporation process, the carbon vapor temperature is lower, the vapor particle velocity is markedly smaller, and these particles may be additionally heated as a result of laser radiation absorption by the carbon species. Nevertheless, the fullerene content α in the soot produced by the laser evaporation under optimum conditions is almost the same as that for the optimum arc process (Fig. 3). In addition, the α value for the arc process exhibits a sharp drop with increasing supplied power, while a decrease in α with increasing beam power for the laser evaporation process is not as pronounced.

A difference in the kinetics of fullerene formation during the arc and laser evaporation is indicated by the results presented in Fig. 4. For the arc process, the plot of α versus helium pressure exhibits sharp nonmonotonic variations. The analogous plot for the laser evaporation process is smoother, the maximum is shifted toward higher pressures, and the α values at low pressures (~20 Torr) are nonzero (in contrast to the arc, where no fullerenes at all are formed under these conditions).

The results of these experiments give us hope that, provided optimization of the process conditions, laser evaporation technology may become an effective method for fullerene synthesis. At present, we may suggest two possible ways for the process optimization: (i) the soot "blowing-off" from the laser spot region and (ii) the "hybrid" laser–gas discharge scheme, in which charged particles are generated in the zone of fullerene formation. As was demonstrated previously [5], the generation of charged particles during the thermal evaporation of graphite significantly intensifies the process of fullerene formation. An advantage of the laser technology for the fullerene synthesis over the arc process is the possibility of using nonconducting carbon materials.

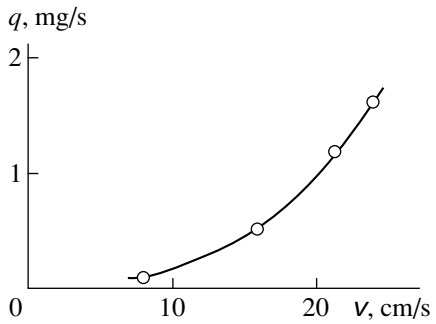

Fig. 2. A plot of the fullerene-containing soot formation rate q versus the velocity of laser beam scanning over the target surface (P_{He} = 100 Torr; W = 2.6 kW).

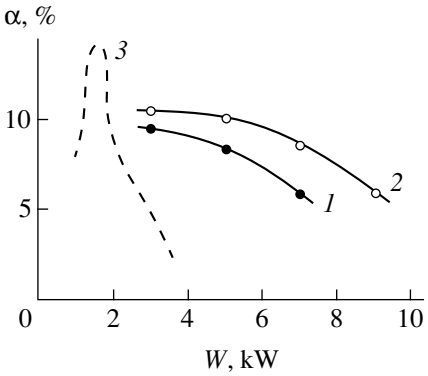

Fig. 3. Plots of the fullerene content α versus the laser radiation power W (P_{He} = 100 Torr): (*1*) graphite target of large diameter; (*2*) graphite target of small diameter; (*3*) arc discharge (data from [4]).

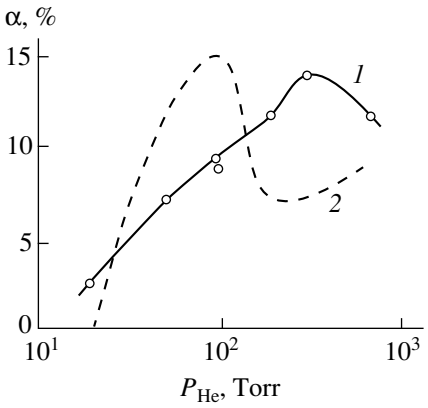

Fig. 4. Plots of the fullerene content α versus the helium pressure P_{He} ($W \sim 3$ kW): (*1*) laser evaporation of a graphite target with small diameter; (*2*) arc discharge (data from [4]).

Acknowledgments. This study was supported by the Interinstitution Scientific-Technological Program "Fullerenes and Atomic Clusters" (complex project no. 3) and by the Russian Foundation for Basic Research (project no. 00-02-16928).

REFERENCES

1. H. W. Kroto, J. R. Heath, S. C. Brien, *et al.*, Nature **318**, 162 (1985).
2. O. P. Gorelik, G. A. Dyuzhev, D. V. Novikov, *et al.*, Zh. Tekh. Fiz. **70** (11), 118 (2000) [Tech. Phys. **45**, 1489 (2000)].
3. A. V. Astakhov, G. A. Baranov, A. B. Budanov, *et al.*, in *Proceedings of the 3rd All-Union Conference "Application of Lasers in Industry," Shatura, 1989*, p. 54.
4. D. V. Afanas'ev, I. O. Blinov, A. A. Bogdanov, *et al.*, Zh. Tekh. Fiz. **64** (10), 76 (1994) [Tech. Phys. **39**, 1017 (1994)].
5. D. V. Afanas'ev, G. A. Dyuzhev, and V. I. Karataev, Pis'ma Zh. Tekh. Fiz. **25** (5), 35 (1999) [Tech. Phys. Lett. **25**, 182 (1999)].

Translated by P. Pozdeev

Technical Physics Letters, Vol. 27, No. 5, 2001, pp. 411–413. Translated from Pis'ma v Zhurnal Tekhnicheskoĭ Fiziki, Vol. 27, No. 10, 2001, pp. 37–42.

The Effect of Pulsed Magnetic Fields on Thin $Cd_{0.5}Zn_{0.5}S$ Layers

M. N. Levin, V. N. Semenov, and Yu. V. Meteleva

Voronezh State University, Voronezh, Russia

e-mail: levin@lev.vsu.ru

Received October 23, 2000

Abstract—It is experimentally established that a short-duration action of a pulsed magnetic field with an induction of $B < 1$ T leads to a stable increase in the intensity of luminescence from thin $Cd_{0.5}Zn_{0.5}S$ films. The films were prepared by pyrolysis of the aerosol of an aqueous solution of metal thiocarbamide complexes on heated substrates. © *2001 MAIK "Nauka/Interperiodica".*

Thin films of metal sulfides of the CdS–ZnS system obtained by the pyrolysis of the aerosols of aqueous solutions of metal thiocarbamide complexes on heated substrates (thermal spray deposition technique [1]) are capable of visible luminescence emission at room temperature [2, 3]. The possible practical applications of such films stimulate the search for methods of increasing the emission intensity.

Recently, it was reported that the intensity of electroluminescence in ZnS single crystals exhibits a severalfold increase upon the exposure of a sample to single pulses of a magnetic field with an induction of $B = 7$ T [4] or $B = 24$ T [5]. However, upon the initial increase, the luminescence intensity relaxed with time and returned to the initial level within several tens of hours. On the other hand, it is known that much weaker pulsed magnetic fields ($B < 1$ T) are capable of irreversibly modifying the impurity-defect structure of $A^{III}B^{V}$ [6], Czochralski-grown silicon (Cz–Si) [7], and $A^{II}B^{VI}$ [8] semiconductor crystals, the latter class including films of the CdS–ZnS system.

The purpose of this work was to study the effect of pulsed magnetic fields on the luminescent properties of thin $Cd_{0.5}Zn_{0.5}S$ films prepared by pyrolysis of the aerosols of aqueous solutions of Cd and Zn thiocarbamide complexes on heated substrates.

The experiments were performed with 0.1–0.5-μm-thick $Cd_{0.5}Zn_{0.5}S$ films obtained by the thermal spray deposition of an aqueous solution of metal thiocarbamide complexes ($[Cd(N_2H_4CS)_2Cl_2]$ and $[Zn(N_2H_4CS)_2Cl_2]$) onto Sitall (glass-ceramic composite) substrates heated to $T \sim 600$ K. The films were exposed to single-polarity magnetic field pulses of a triangular shape with variable amplitude ($B = 0.2$–0.6 T), a duration of $\tau = 2 \times 10^{-5}$ s, and a repetition rate of $t_0 = 2 \times 10^{-2}$ s. The number of pulses was varied up to $N = 3000$. The magnetic treatment of the samples was carried out in air at $T = 300$ K or in liquid nitrogen vapors at $T = 77$ K.

The luminescence in the film samples was excited by radiation of an LG-21 nitrogen laser operating at a wavelength of $\lambda = 334$ nm. The sample emission was measured using an automated setup of the KSVU type based on an MDR-24 monochromator. The photoluminescence (PL) spectra were recorded prior to the pulsed magnetic field application, one hour after treatment, and then every 24 h.

The main effect of the pulsed magnetic field application is illustrated in Fig. 1. As is seen, a short-duration magnetic field action upon the $Cd_{0.5}Zn_{0.5}S$ films led to a long-term increase in the PL intensity without significant changes in the emission spectrum. Figure 2 shows the pattern of variation of the PL intensity with time after the magnetic treatment.

A very important result is that the pulsed magnetic field action upon the $Cd_{0.5}Zn_{0.5}S$ films studied produced an irreversible increase in the PL intensity. This is a principal difference of the observed effect from the short-duration increase in the electroluminescence intensity reported in [4, 5] for ZnS crystals exposed to single pulses of a strong magnetic field. The increase in the PL intensity observed in our experiments was proportional to the number of applied magnetic field pulses, but rather weakly depended on the field strength (pulse amplitude). The bars in Fig. 2 show the scatter of data corresponding to the pulse amplitude varied in the interval indicated above. The magnetic field action on the samples cooled to liquid nitrogen temperature produced no increase in the PL intensity.

The experimental results obtained can probably be interpreted as follows. The fact that the spectral position of the PL band maximum remains unchanged indicates that the pulsed magnetic field action does not change the nature of the emission centers. It is commonly accepted that a maximum of the PL band of

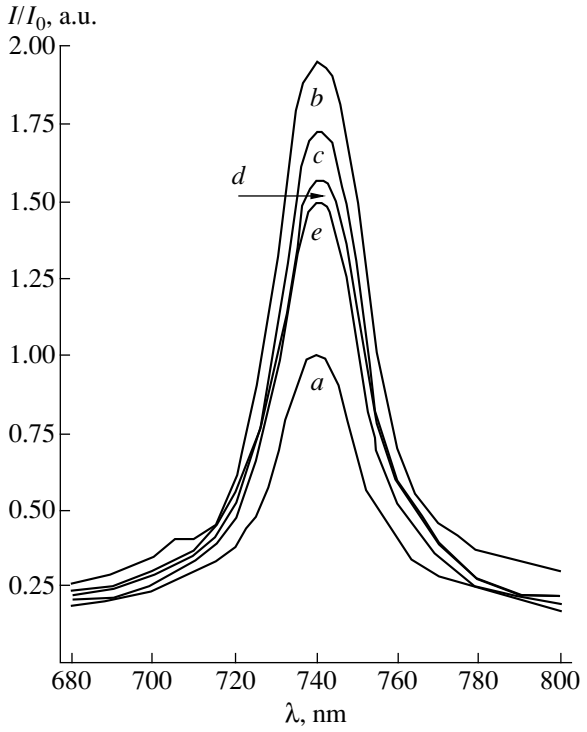

Fig. 1. Photoluminescence spectra of $Cd_{0.5}Zn_{0.5}S$ films measured (*a*) before and (*b*–*e*) at various times after a pulsed magnetic field treatment (h): (*b*) 1; (*c*) 24; (*d*) 48; (*e*) 164. Magnetic treatment regime: $B = 0.6$ T; $\tau = 2 \times 10^{-5}$ s; $t_0 = 2 \times 10^{-2}$ s; $N = 2000$.

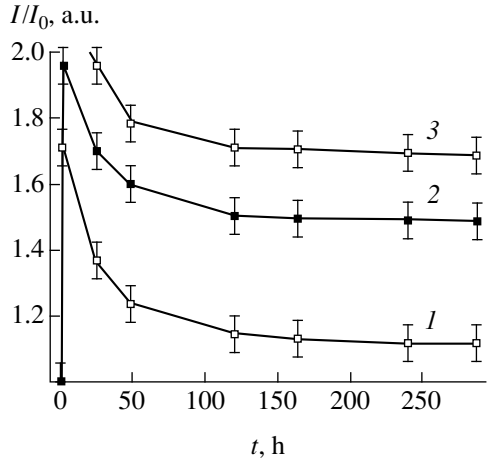

Fig. 2. Time variation of the maximum PL intensity in $Cd_{0.5}Zn_{0.5}S$ films (normalized to the initial values) treated in a pulsed magnetic field at $B = 0.2$–0.6 T, $\tau = 2 \times 10^{-5}$ s; $t_0 = 2 \times 10^{-2}$ s, and $N = 1000$ (*1*); 2000 (*2*); 3000 (*3*).

$Cd_{0.5}Zn_{0.5}S$ films observed at $\lambda \sim 730$–750 nm is due to the presence of oxygen atoms substituted for sulfur atoms in the crystal lattice sites [9].

Thin $Cd_{0.5}Zn_{0.5}S$ films obtained by the pyrolysis of the aqueous solution aerosol in air are unavoidably enriched with oxygen. This oxygen partly substitutes for sulfur in the lattice sites, thus providing for the initial luminescence level, while the remaining oxygen either occurs in interstitials or enters into some metastable defect complexes. We may suggest that the application of a pulsed magnetic field to the $Cd_{0.5}Zn_{0.5}S$ films initiates decomposition of the oxygen-containing defect complexes (leading to the release of atomic oxygen) or displaces oxygen atoms from interstitial positions. A certain part of these additional atoms may occupy the existing vacant lattice sites, thus producing additional emission centers in the films subjected to the pulsed magnetic field treatment.

A similar effect of the pulsed-magnetic-field-induced formation of oxygen–vacancy centers was previously observed in oxygen-rich silicon single crystals grown from the melt by the Czochralski method [7]. A mechanism responsible for the magnetic field action upon the defect structure of Cz–Si crystals was related to the weakening of the Si–O bond as a result of nonequilibrium population of a metastable term [7, 10].

In the $Cd_{0.5}Zn_{0.5}S$ films, a possible mechanism leading to the decay of the initial defect complexes can be related to the removal of prohibition concerning spin-forbidden electron transitions to the multiplet states corresponding to weaker molecular bonds. This excitation of molecular bonds may facilitate the bond breakage as a result of thermal fluctuations of the lattice. The probability of such breakage considerably increases under the action of multiply repeated magnetic pulses.

The proposed mechanism is consistent with the experimentally observed dependence of the effect of increased PL intensity on the number of magnetic pulses and the absence of this effect in the samples treated with a pulsed magnetic field at liquid nitrogen temperature. The long-term relaxation of the PL intensity, following the initial increase and resulting in attaining a new stable level (Fig. 2), can be related to consumption of some of the emission centers in the process of secondary defect formation, the rate of which is limited by diffusion, which is rather slow at room temperature.

Thus, we have experimentally established that a short-duration action of a relatively weak ($B < 1$ T) pulsed magnetic field leads to a significant and stable increase in the PL intensity in thin $Cd_{0.5}Zn_{0.5}S$ films obtained by the pyrolysis of an aqueous solution of metal thiocarbamide complexes in air. This effect can be used to increase the quality of thin luminescent layers of the CdS–ZnS system.

REFERENCES

1. L. Pawlowski, *The Science and Engineering of Thermal Spray Coatings* (Wiley, Chichester, 1995).

2. V. N. Semenov, V. G. Klyuev, M. A. Kushnik, *et al.*, Zh. Prikl. Spektrosk. **59** (1–2), 114 (1993).
3. V. N. Semenov, O. V. Ostapenko, A. I. Lukin, *et al.*, Neorg. Mater. **36** (2), 160 (2000).
4. Yu. I. Golovin, R. B. Morgunov, A. A. Baskakov, *et al.*, Fiz. Tverd. Tela (St. Petersburg) **41** (11), 1944 (1999) [Phys. Solid State **41**, 1783 (1999)].
5. Yu. I. Golovin, R. B. Morgunov, A. A. Baskakov, *et al.*, Pis'ma Zh. Éksp. Teor. Fiz. **69** (2), 114 (1999) [JETP Lett. **69**, 127 (1999)].
6. V. N. Davydov, E. A. Loskutova, and E. P. Naĭden, Fiz. Tekh. Poluprovodn. (Leningrad) **23** (9), 1596 (1989) [Sov. Phys. Semicond. **23**, 989 (1989)].
7. M. N. Levin and B. A. Zon, Zh. Éksp. Teor. Fiz. **111** (4), 1373 (1997) [JETP **84**, 760 (1997)].
8. V. P. Vlasov, F. A. Zaitov, V. M. Kanevskiĭ, *et al.*, Fiz. Tverd. Tela (St. Petersburg) **34** (10), 3264 (1992) [Sov. Phys. Solid State **34**, 1747 (1992)].
9. N. P. Golubeva and M. V. Fok, Zh. Prikl. Spektrosk. **17** (2), 261 (1972).
10. M. N. Levin and B. A. Zon, Phys. Lett. A **260**, 386 (1999).

Translated by P. Pozdeev

Technical Physics Letters, Vol. 27, No. 5, 2001, pp. 414–418. Translated from Pis'ma v Zhurnal Tekhnicheskoĭ Fiziki, Vol. 27, No. 10, 2001, pp. 43–51.

Reconstruction of Scalar Time-Delay System Models

A. S. Karavaev, V. I. Ponomarenko, and M. D. Prokhorov

Saratov Branch, Institute of Radio Engineering and Electronics, Russian Academy of Sciences, Saratov, Russia

e-mail: mdprokh@ire.san.ru

Received January 9, 2001

Abstract—A new method is proposed for the reconstruction of scalar time-delay system models. The method is simple, fast, and applicable to the analysis of noisy data. The performance of the proposed method is illustrated by application to the time series obtained in a numerical experiment (with a possible noise component) and in a real radiophysical system. © *2001 MAIK "Nauka/Interperiodica"*.

Introduction. Systems, whose dynamics are not entirely determined by the present state, but depend on the past state as well (called time-delay systems), represent a large class of dynamic systems and are frequently described by models in the form of differential equations with delayed argument [1–3]. The model delay equations can be reconstructed from the experimental time series and used for determining the parameters of the time-delay system studied.

For many physical and biological time-delay systems, the models are formulated as first-order differential equations with delays of the following general type:

$$\varepsilon\dot{x}(t) = -x(t) + f(x(t-\tau_0)), \qquad (1)$$

where x is the dynamic variable, f is a nonlinear function, τ_0 is the delay time, and ε is a dimensionless parameter characterizing the ratio of relaxation and delay times. In order to uniquely determine the evolution of the system, it is necessary to set the initial conditions in the entire interval $[x(t_0-\tau_0), x(t_0)]$. Thus, the system possesses an infinite number of degrees of freedom and is unambiguously described in a phase space of infinite dimensionality.

Bünner *et al* [4, 5] showed that, if a trajectory determined by Eq. (1) is projected from the phase space of infinite dimensionality to the three-dimensional (3D) space $[x(t-\tau_0), x(t), \dot{x}(t)]$, the manifold of points attended by the system in this space is situated on a surface (2D space). A cross section of this surface by the plane $\dot{x}(t) = 0$ determines the form of the nonlinear function f because Eq. (1) under these conditions yields

$$x(t) = f(x(t-\tau_0)). \qquad (2)$$

Since the delay time τ_0 is a priori unknown, the time series is projected into 3D spaces $[x(t-\tau), x(t), \dot{x}(t)]$ with various τ values and then the cross sections of these spaces $[x(t-\tau), x(t)]$ are constructed for $\dot{x}(t) = 0$. A single-valued relationship (2) in these cross sections takes place only for $\tau = \tau_0$. As a quantitative criterion for selecting τ_0, we may use either various measures of complexity of the projected time series [4–8] or a minimum error of predictions based on the constructed model [9, 10].

Below we propose a new method for the reconstruction of scalar time-delay system models, which is based on a statistical analysis of derivatives of the observable dynamic variable at various points of the time series. The method is aimed at a reconstruction of the model differential equations of type (1) from the time series, including determination of the delay time, the nonlinear function $f[x(t-\tau_0)]$, and the parameter ε.

Description of the method. The proposed approach is based on the following considerations. Let us differentiate the model delay equation (1) with respect to time:

$$\varepsilon\ddot{x}(t) = -\dot{x}(t) + \frac{df(x(t-\tau_0))}{dx(t-\tau_0)}\dot{x}(t-\tau_0). \qquad (3)$$

For the absolute majority of points on the chaotic trajectory of Eq. (1), $\dot{x}(t)$ and $\ddot{x}(t)$ do not simultaneously turn zero. [Indeed, in the general case, the condition $\dot{x}(t) = \ddot{x}(t) = 0$ for a function $x(t)$ can be fulfilled either at an inflection point or at a point of nonquadratic extremum; otherwise, there must be an interval in which the dynamic variable is constant.] Then, for $\dot{x}(t) = 0$, $\ddot{x}(t) \neq 0$ and we infer from Eq. (3) that $\dot{x}(t-\tau_0) \neq 0$. This result implies that $\dot{x}(t)$ and $\dot{x}(t-\tau_0)$ do not simultaneously turn zero. For $\tau \neq \tau_0$, relationship (3) is not satisfied and the derivatives $\dot{x}(t)$ and $\dot{x}(t-\tau_0)$ can be simultaneously equal to zero.

Based on these considerations, it is possible to determine the unknown delay time τ_0 using the available time series. For this purpose, let us first find the

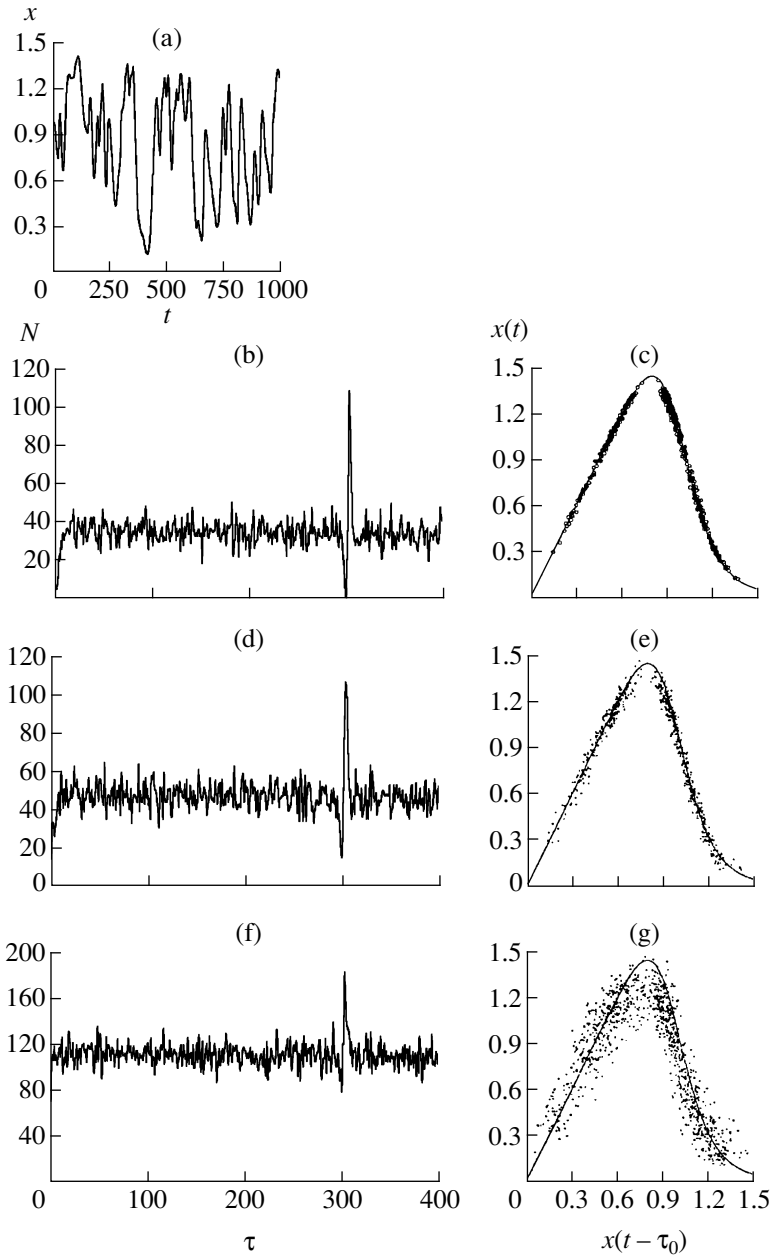

Fig. 1. (a) Time series of a Mackey–Glass system with $a = 0.2$, $b = 0.1$, $c = 10$, and $\tau_0 = 300$; (b, d, f) $N(\tau)$ plots in the absence of noise and for a 3 or 10% noise level, respectively; (c, e, g) nonlinear function (5) (solid curves) and the reconstructed functions (circles in 2c and points in 2e, 2g) in the absence of noise and for a 3 or 10% noise level, respectively.

points of extrema on the trajectory, that is, the points where $\dot{x}(t) = 0$. Then it is necessary to determine for various τ over the entire time series the number N of situations in which $\dot{x}(t) = \dot{x}(t - \tau) = 0$. Finally, we plot $N(\tau)$ (see, e.g., Fig. 1b) and determine the delay time by taking into account that the absolute minimum of $N(\tau)$ is reached at $\tau = \tau_0$. The proposed method is simple and fast. The volume of computations is reduced by a factor of several tens as compared to that required in the previously known schemes used for the reconstruction of time-delay systems. This is related to the fact that, after determining $\dot{x}(t)$ (this is a necessary stage in all methods), the procedure reduces entirely to the operations of comparing and adding, rather than calculating approximation errors or certain measures of the motion complexity.[1]

[1] In principle, one may determine $\dot{x}(t)$ and $\ddot{x}(t)$ simultaneously and exclude from consideration the points where $\dot{x}(t) = \ddot{x}(t) = 0$. However, the results of our investigations indicate that, for most time patterns of various systems in the state of developed chaos, the number of such points is extremely small or zero. Therefore, the analysis can be restricted to determining the first derivative.

Once the time delay is determined, we may reconstruct the nonlinear function $f[x(t-\tau_0)]$ by plotting the points for which $\dot{x}(t) = 0$ on the $[x(t-\tau_0), x(t)]$ plane. According to Eq. (2), this plot reproduces the unknown nonlinear function. Upon reconstructing the function $f[x(t-\tau_0)]$, we may find the parameter ε using Eq. (1): $\varepsilon = [f(x(t-\tau_0)] - x(t))/\dot{x}(t)$.

Performance of the method. We can demonstrate the performance of the proposed reconstruction method by applying the procedure outlined above to numerical and experimental data. Let us first study a scalar time series (Fig. 1a) generated by the Mackey–Glass equation:

$$\dot{x}(t) = -bx(t) + \frac{ax(t-\tau_0)}{1 + x^c(t-\tau_0)}. \quad (4)$$

We will consider the case of $a = 0.2$, $b = 0.1$, $c = 10$, and $\tau_0 = 300$, which corresponds to the motion on a chaotic attractor. Equation (4) can be converted to the form (1) by introducing $\varepsilon = 1/b$ and the function

$$f(x(t-\tau_0)) = \frac{ax(t-\tau_0)}{b(1 + x^c(t-\tau_0))}. \quad (5)$$

According to the proposed method, we counted the number N of points in the interval $\tau \in [1, 400]$ where simultaneously $\dot{x}(t) = \dot{x}(t-\tau) = 0$, and plotted $N(\tau)$ (Fig. 1b). This plot was constructed for a time series containing 10000 points and exhibiting about 600 extrema. To determine $\dot{x}(t)$ from time series, we performed a 5-point smoothening using a second order polynomial. The absolute minimum of $N(\tau)$ is observed for $\tau = \tau_0 = 300$, where $N(300) = 0$. As the length of the time series (and, hence, the number of extrema) decreases, the minimum becomes less pronounced; beginning with a certain length, there appear points with $\tau \neq \tau_0$ for which $N(\tau) = 0$. The result of reconstruction of the nonlinear function is demonstrated in Fig. 1c (circles). The value of ε, determined as described above and averaged over all points of the time series at which $f[x(t-\tau_0)]$ is determined for $\dot{x}(t) \neq 0$, is $\varepsilon = 10.6$ (the exact value is $\varepsilon = 1/b = 10$).

In order to check the performance of the proposed method in the presence of noise, let us consider the series obtained by introducing a Gaussian white noise term into Eq. (4). Figures 1d–1g show the plots of $N(\tau)$ and the reconstructed nonlinear functions for an additive noise with zero mean and a mean square deviation amounting to 3 and 10% of the standard deviation for the initial noiseless series. As the noise level increases, the absolute minimum in the $N(\tau)$ plot becomes less pronounced: [$N_{\min}(\tau) = N(300) = 15$ (Fig. 1d) against $N_{\min}(\tau) = N(300) = 79$ (Fig. 1f)], while the plot in the $[x(t-\tau_0), x(t)]$ plane becomes more ambiguous. For the noise levels above 10%, $N(\tau_0)$ is no longer the absolute minimum of $N(\tau)$. These results indicate that the proposed method is sufficiently robust with respect to noise and can be used for the analysis of time series of real systems.

Now we will employ the proposed method to study a time-delay feedback oscillator [3]. For the system depicted in Fig. 2a, a model equation derived from Kirchhoff is as follows:

$$RC\dot{V}(t) = -V(t) + f(V(t-\tau_0)), \quad (6)$$

where $V(t)$ and $V(t-\tau_0)$ are the delay line (DL) input and output voltages, respectively; R and C are the resistance and capacitance of the filter elements, respectively; f is the transmission function of the nonlinear device (ND); and τ_0 is the delay time. Equation (6) has the form of (1) with $\varepsilon = RC$. We will study the corresponding time series, with the nonlinear function represented by a logistic delay function of the type

$$f(V(t-\tau_0)) = \lambda - V^2(t-\tau_0), \quad (7)$$

where λ is a nonlinearity parameter ($0 < \lambda \leq 2$).

Figures 2b–2d show the time series of system (6), the plot of $N(\tau)$, and the nonlinear function reconstructed for $\lambda = 1.9$, $\tau_0 = 1000$, and $RC = 10$. For the time series containing 10000 points and exhibiting about 400 extrema, $N_{\min}(\tau) = N(1000) = 0$. The nonlinear function reconstructed for $\tau_0 = 1000$ virtually coincides with that numerically obtained using Eq. (7). The reconstructed value of $\varepsilon = RC$ averaged over the entire series is $RC = 9.9$. Note that the RC value can be approximately evaluated from $\tau_c = \tau_m - \tau_0$, where τ_m is the value corresponding to the absolute maximum of $N(\tau)$. As the RC value increases, the characteristic time scale of the oscillations and the time interval between the extrema of $x(t)$ grow, which leads to the increase in τ_m and τ_c. By varying the values of RC, λ, and τ_0 within broad limits, we obtained the following empirical relationship: $\tau_c \approx RC/2$. Based on this result, an approximate estimate of RC can be obtained using the $N(\tau)$ plot and the relationship $RC \approx 2\tau_c$. In the presence of noise, this estimate may be more accurate than others because the restored nonlinear function may be ambiguous and require averaging.

Finally, we will study the time series obtained in a real radiophysical experiment according to the scheme depicted in Fig. 2e. Here, the RC filter and the nonlinear device (ND) (representing a transistor circuit with a nonlinear characteristic possessing a quadratic extremum) were analog units, while the delay line (DL) based on integrated circuits was a digital unit. The coupling between the analog and digital elements of the scheme was provided by the analog-to-digital and digital-to-analog converters (ADC and DAC, respec-

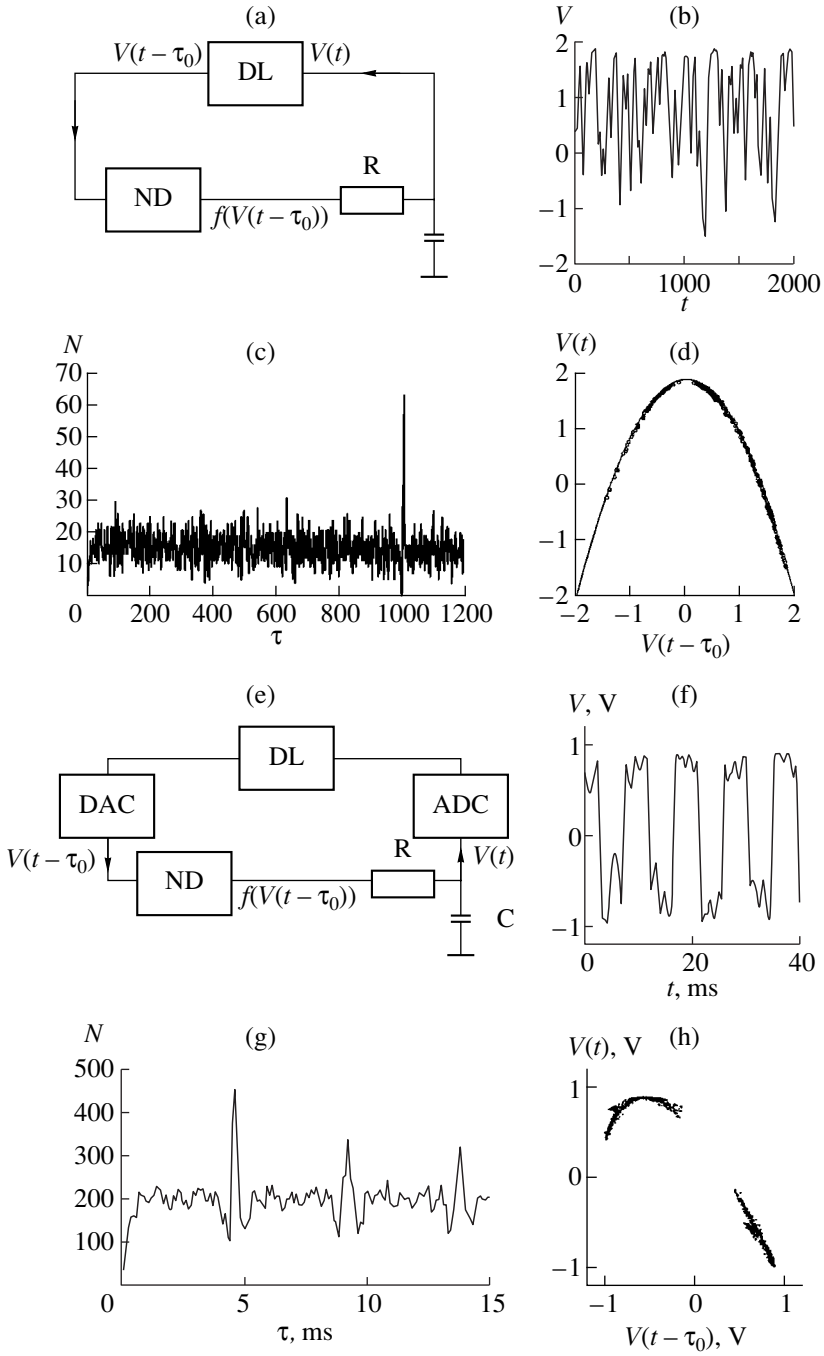

Fig. 2. (a, e) Schematic diagrams of the time-delay feedback oscillator studied in a numerical and real experiment, respectively (ND, nonlinear device; DL, delay line; ADC and DAC, analog-to-digital and digital-to-analog converters); (b, c, d) time series of system (6), $N(\tau)$ plot, and reconstructed nonlinear function (circles, for Eq. (6); solid curve, for Eq. (7)), respectively, for $\lambda = 1.9$, $\tau_0 = 1000$, and $RC = 10$; (f, g, h) time series of the experimental system, $N(\tau)$ plot, and reconstructed nonlinear function for $\tau_0 = 4.5$ ms and $RC = 0.08$ ms.

tively). Figure 2f shows a time series corresponding to $\tau_0 = 4.5$ ms, $RC = 0.08$ ms, and a sampling time of 0.1 ms, which contains 10000 points and exhibits about 1400 extrema. In this series, the absolute minimum of $N(\tau)$ is observed at $\tau = 4.4$ ms (Fig. 2g). The reconstructed nonlinear function (Fig. 2h) reproduces sufficiently well the ND transmission function. The RC value averaged over the entire time series is $RC = 0.11$ ms.

Conclusion. We proposed and verified on numerical and real radiophysical systems a new method for reconstructing scalar time-delay systems. The method is simple, requires a significantly smaller volume of compu-

tations as compared to other methods, and can be successfully used for the analysis of rather noisy data.

Acknowledgments. This study was supported by the Russian Foundation for Basic Research (project no. 99-02-17735) and by the US Civilian Research and Development Foundation for the Independent States of the Former Soviet Union (Award no. REC–006).

REFERENCES

1. M. C. Mackey and L. Glass, Science **197**, 287 (1977).
2. K. Ikeda, Opt. Commun. **30**, 257 (1979).
3. S. P. Kuznetsov, Izv. Vyssh. Uchebn. Zaved., Radiofiz. **25**, 1410 (1982).
4. M. J. Bünner, M. Popp, Th. Meyer, *et al.*, Phys. Lett. A **211**, 345 (1996).
5. M. J. Bünner, M. Popp, Th. Meyer, *et al.*, Phys. Rev. E **54**, 3082 (1996).
6. A. C. Fowler and G. Kember, Phys. Lett. A **175**, 402 (1993).
7. M. J. Bünner, Th. Meyer, A. Kittel, *et al.*, Phys. Rev. E **56**, 5083 (1997).
8. Y.-C. Tian and F. Gao, Physica D (Amsterdam) **108**, 113 (1997).
9. R. Hegger, M. J. Bünner, and H. Kantz, Phys. Rev. Lett. **81**, 558 (1998).
10. C. Zhou and C.-H. Lai, Phys. Rev. E **60**, 320 (1999).

Translated by P. Pozdeev

Technical Physics Letters, Vol. 27, No. 5, 2001, pp. 419–421. Translated from Pis'ma v Zhurnal Tekhnicheskoĭ Fiziki, Vol. 27, No. 10, 2001, pp. 52–56.

The Kinetics of Surface Monomolecular Reactions

G. Ya. Lavrent'ev

Ioffe Physicotechnical Institute, Russian Academy of Sciences, St. Petersburg, 194021 Russia

Received October 2, 2000

Abstract—A comparison of various theoretical kinetic schemes with experimental results shows that the surface monomolecular decay of both individual molecules and the fragments of polymolecular complexes is a nonequilibrium process corresponding to first- and second-order reactions, respectively. © *2001 MAIK "Nauka/Interperiodica".*

The course of monomolecular reactions in the gas phase is considered in much detail by several statistical theories [1, 2]. It was shown [3, 4] that, using the detailed balancing principle, the theory of monomolecular reactions in the gas phase can be applied to the heterogeneous process of the decay of polyatomic molecules, followed by their ionization according to the surface mechanism. Let us consider the interaction of molecules with the surface using a different approach, based on the Lindeman scheme for the monomolecular reaction mechanism based on the theory of collisions [2].

The process of activation of a molecule interacting with the surface atoms is described by the reaction

$$A + S \xrightarrow{k_1} A^* + S.$$

At the same time, the interaction of active molecules with the surface leads to their deactivation:

$$A^* + S \xrightarrow{k_2} A + S.$$

In addition to this, the activated molecules may decay on the surface by the scheme

$$A^* + S \xrightarrow{k_3} \text{Reaction products}.$$

In a stationary process, the concentration of active molecules is constant, which is determined by the condition that "activation rate = deactivation rate + reaction rate":

$$k_1[A] = k_2[A^*] + k_3[A^*].$$

In this case, the concentration of active molecules is

$$[A^*] = \frac{k_1[A]}{k_2 + k_3},$$

and the decay rate can be expressed as

$$-\frac{\partial[A]}{\partial t} = k_3[A^*] = \frac{k_1 k_3}{k_2 + k_3}[A]. \qquad (1)$$

Depending on the ratio of the rate constants of deactivation (k_2) and decay (k_3), we may consider Eq. (1) in two limiting cases.

1. $k_2 \gg k_3$. In this case, the lifetime of an active molecule $\tau^* = k_3^{-1}$ is large compared to the characteristic deactivation time $\tau = k_2^{-1}$ ($\tau^* \gg \tau$). Here, Eq. (1) acquires the following form:

$$-\frac{\partial[A]}{\partial t} = \frac{k_1 k_3}{k_2}[A] = k_\infty[A],$$

which describes a first-order reaction in agreement with the experiment. A low decay rate provides for an equilibrium energy distribution of the molecules and all the rate constants k_i (i = 1–3) and k_∞ can be written in the Arrhenius form. However, this equation does not describe experimental data on the flux of desorbed molecules as a function of the temperature.

2. $k_3 \gg k_2$. In this case, $\tau \gg \tau^*$ and Eq. (1) yields

$$-\frac{\partial[A]}{\partial t} = k_1[A] = k_0[A],$$

which shows that the process still corresponds to the first-order reaction. This is a very important result because the small (as compared to the deactivation time) lifetime of active molecules in the gas phase leads to second-order reactions at low pressures.

Under the conditions of fast decay of the active molecules, the reaction rate is determined by the rate of formation of these molecules (with the activation energy E). From this we infer that the equilibrium distribution of molecules with respect to energy must be violated because the decay in the equilibrium state involves mostly molecules with internal energies exceeding the activation energy by a value equal to the average energy. Indeed, the study of the relaxation of the energy distribution of polyatomic molecules on the surface [5] showed that the average temperature of the energy distribution of the ionized decay products in the initial stage of the decay reaction is lower than the surface temperature.

1063-7850/01/2705-0419$21.00 © 2001 MAIK "Nauka/Interperiodica"

The above considerations lead to the conclusion that the fast surface decay condition arises because the activation of an adsorbed molecule takes place only at a large amplitude of oscillations of the surface atoms, which is statistically a rare event. The oscillations of surface atoms with average amplitudes lead to neither activation nor deactivation of the adsorbed molecules.

Under the fast decay conditions, the statistical theory of monomolecular reactions gives the following expression for the reaction rate constant, which describes the experimental dome-shaped temperature dependences [2]:

$$k_m = F\left[\frac{E}{kT}\right]^{s-1}\exp\left(-\frac{E}{kT}\right), \quad (2)$$

where F = const, E is the activation energy (in our case, on the surface), and s is the total number of the vibrational degrees of freedom (equal to $3n - 6$ for polyatomic molecules); the quantity s is used when $kT \gg h\nu$, where ν are the frequencies of molecular oscillations.

In the opposite case of $kT \ll h\nu$ (all our experiments fall within this range), the power term in Eq. (2) is written with an effective number of the degrees of freedom b [1], which usually falls between 1/4 and 1/3 of the total number s [3, 4]:

$$k_m = F\left[\frac{E}{kT}\right]^{b}\exp\left(-\frac{E}{kT}\right). \quad (2a)$$

Now let us assume that the molecules occurring on the surface at a relatively low temperature form molecular complexes involving 2, 3, 4, or a greater number of molecules, which is typical of both atomic and molecular two-dimensional gases on the surface [6, 7]. The formation of polymolecular complexes on the surface may be accompanied by the reactions of dissociation, substitution, and association of the component molecules (i.e., leading to the formation of a polymolecular activated complex). Since the bonds in such a polymolecular complex are relatively weak, the complex may exist at a sufficiently low temperature. The results of desorption experiments in this emitter temperature interval showed temperature-dependent fluxes of desorbed molecules and ions for the associated ions of polyatomic molecules [8], peaks of dimer molecules [9], and peaks corresponding to the nonequilibrium surface ionization of acetone peroxide. The mechanisms of decay of such surface complexes and the temperature dependence of this process will be considered in the following paper. Here, we will only develop a scheme of the process and write equations describing the excitation and monomolecular decay of a molecule or a polymolecular complex fragment.

According to the main postulate of chemical kinetics, the decay rate of a given molecule A must be proportional to the concentration of these molecules. Therefore, we must separate molecule A from a polymolecular complex $A_N \Leftrightarrow A_1 + \ldots + A_N$. Thus, the process of excitation of fragment A entering into a polymolecular complex A_N on the surface is described by the following scheme:

$$A_N + S \equiv A_{N-1} + A + S \xrightarrow{k_1} A_{N-1} + A^* + S.$$

The process of deactivation (k_2) of an active molecule or its decay (k_3) into reaction products on the surface is as follows:

$$A^* + S \xrightarrow{k_2} A + S,$$

$$A^* + S \xrightarrow{k_3} \text{Reaction products}.$$

The concentration of excited molecules is determined from the condition of constant concentration of active molecules in the stationary process:

$$k_1[A_{N-1}][A] = k_2[A^*] + k_3[A^*],$$

which yields

$$[A^*] = \frac{k_1[A_{N-1}][A]}{k_3 + k_2}.$$

Therefore, the reaction rate is

$$-\frac{\partial[A]}{\partial t} = k_3[A^*] = \frac{k_1k_3}{k_2 + k_3}[A][A_{N-1}].$$

As is seen from this equation, the monomolecular decay of a fragment of a polymolecular complex is a second-order reaction. The results of experiments with associated ions of the [A + H] type (where H is hydrogen) showed that the process of associated ion formation actually follows the second-order reaction law [10]. The admission of hydrogen, deuterium, or water to the reaction zone did not lead to an increase in the desorption current. This fact indicates that the second order of the reaction is probably explained by the detachment of the associated ion from a polymolecular complex, rather than by the attachment of hydrogen to molecule A. This conclusion and the experimentally established first order of the reaction of decay of a single molecule [5] confirm the kinetic schemes considered above.

It should be emphasized that a very important conclusion is that the surface monomolecular decay of molecules is a nonequilibrium process. Should the lifetime of ions on the surface increase, the ion temperature may come into equilibrium with the surface temperature, but the process physics will remain the same.

Acknowledgments. I wish to thank N.D. Potekhina and N.M. Blashenkov for fruitful discussions and interest in this study.

REFERENCES

1. V. N. Kondrat'ev and E. E. Nikitin, *Kinetics and Mechanism of Gas-Phase Reactions* (Nauka, Moscow, 1975).
2. G. M. Panchenkov and V. P. Lebedev, *Chemical Kinetics and Catalysis* (Khimiya, Moscow, 1985).
3. N. M. Blashenkov, N. I. Ionov, and G. Ya. Lavrent'ev, Pis'ma Zh. Tekh. Fiz. **13** (7), 392 (1987) [Sov. Tech. Phys. Lett. **13**, 160 (1987)].
4. N. M. Blashenkov, N. I. Ionov, and G. Ya. Lavrent'ev, Teor. Éksp. Khim., No. 1, 62 (1988).
5. N. M. Blashenkov and G. Ya. Lavrent'ev, Zh. Tekh. Fiz. **60** (2), 154 (1990) [Sov. Phys. Tech. Phys. **35**, 227 (1990)].
6. E. W. Muller, Ergeb. Exakten. Naturwiss. **27**, 290 (1953).
7. T. T. Tsong, Surf. Sci. Rep., No. 8, 127 (1988).
8. É. Ya. Zandberg and U. Kh. Rasulev, Usp. Khim. **51** (9), 1425 (1982).
9. N. I. Ionov and M. A. Mittsev, Zh. Tekh. Fiz. **35** (10), 1863 (1965) [Sov. Phys. Tech. Phys. **10**, 1436 (1966)].
10. É. Ya. Zandberg and U. Kh. Rasulev, Dokl. Akad. Nauk SSSR **187** (4), 777 (1969) [Sov. Phys. Dokl. **14**, 769 (1969)].

Translated by P. Pozdeev

Technical Physics Letters, Vol. 27, No. 5, 2001, pp. 422–423. Translated from Pis'ma v Zhurnal Tekhnicheskoĭ Fiziki, Vol. 27, No. 10, 2001, pp. 57–61.

The Oxide Layer Charging in SIMOX Structures

A. Yu. Askinazi, A. P. Baraban, V. A. Dmitriev, and L. V. Miloglyadova

Institute of Physics, St. Petersburg State University, St. Petersburg, Russia

Received January 17, 2001

Abstract—The depth profile analysis, based on the measurement of high-frequency capacitance–voltage characteristics of an electrolyte–insulator–semiconductor system in the course of the layer-by-layer insulator removal by etching, showed that the formation of a SIMOX structure is accompanied by the appearance of positively charged defects in the oxide layer at the oxide– silicon interface. A change in the charge state of the SIMOX structures under the action of an applied electric field, near ultraviolet (UV) radiation, and low-temperature annealing was studied. © *2001 MAIK "Nauka/Interperiodica".*

Planar Si–SiO_2 structures and related metal–insulator–semiconductor (MIS) systems are base elements of modern micro and solid-state electronics. A study of the properties of these structures is of considerable interest for both fundamental science and applied research. An important method of obtaining Si–SiO_2 structures consists in the formation of buried oxide layers in the bulk of silicon by oxygen implantation (SIMOX technology). Despite numerous investigations of these structures, there are still open questions concerning the exact localization, properties, and nature of the electrically active centers in the SIMOX structures.

The purpose of this study was to determine the distribution and magnitude of charges appearing in the oxide layer of a SIMOX structure during the buried SiO_2 layer formation. We also studied the properties of defects responsible for the appearance of charges and the effects of applied field, UV irradiation, and low-temperature annealing on these defects.

The experiments were performed with Si–SiO_2 structures prepared by oxygen ion implantation at an energy of 190 keV and a total dose of 1.8×10^{18} cm^{-2} into a silicon substrate heated to a temperature of 650°C. The ion implantation was followed by thermal annealing for 6 h at T = 1320°C and by etching-off the external silicon layer, which left a silicon dioxide layer with a thickness of about 450 nm. The applied electric field strengths were sufficiently low to not produce a breakdown in the oxide film (E_{ox} = 1–5 MV/cm). The UV radiation ($h\nu$ = 4–6 eV) was emitted by a DRL-250 mercury lamp. The low-temperature annealing was effected in air at T = 200–300°C.

The charge state of the Si–SiO_2 sample structures was studied using a method of depth profiling based on the measurement of high-frequency capacitance–voltage characteristics of the sample in the course of the layer-by-layer oxide removal by etching. These data give a plot of the flat-band potential V_{fb} versus the oxide layer thickness d_{ox} (Figs. 1 and 2). The position X of the centroid of charges localized in the oxide layer was determined at the point of intersection of the V_{fb} versus d_{ox} plots extrapolated to the zero oxide film thickness. The true charge values were determined from the slopes of these plots [1]. All measurements were performed at 293 K in the electrolyte–insulator–semiconductor system.

It was established that the SIMOX structure formation leads to the appearance of a positive charge density $Q = (0.4 \pm 0.1) \times 10^{12}$ cm^{-2} in the oxide layer at the SiO_2–Si interface, with a centroid position $X = 65 \pm 10$ nm (Fig. 1). Exposure to the UV radiation in the absence of applied electric fields led to a virtually complete neutralization of this charge (Fig. 1). The applica-

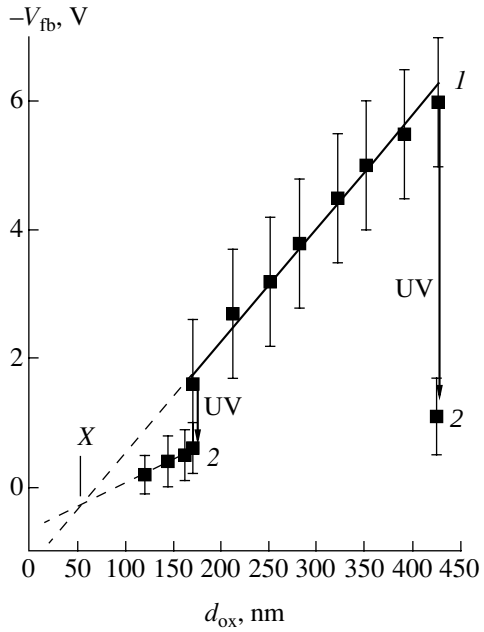

Fig. 1. Plots of the flat-band potential V_{fb} versus oxide layer thickness d_{ox} for SIMOX structures: (*1*) initial; (*2*) UV-irradiated.

tion of an electric field with a strength of E_{ox} = 1 MV/cm to a nonirradiated SIMOX structure did not affect the charged state of the structure. The same field (E_{ox} = 1 MV/cm) applied after the UV irradiation led to an insignificant positive charging of the sample. Simultaneous exposure to the UV radiation and application of the field (E_{ox} = 1 MV/cm) resulted in the appearance of a considerable positive charge.

The electric field with E_{ox} = 5 MV/cm applied to the SIMOX structures (both before and after UV irradiation) also gave rise to a large positive charge with a centroid at $X = 65 \pm 10$ nm (Fig. 2). The formation of a positive charge at the increased electric field strength was not completed during the field application. The UV irradiation of the samples upon the electric field treatment led to negative charging. The absolute value and centroid position of this negative charge were virtually the same as those for the positively charged oxide (Fig. 2). The subsequent low-temperature annealing did not alter the charge state of the oxide layer in the SIMOX structures neither before nor after the field application or UV irradiation.

We believe that the appearance of a positive charge in the oxide layer of SIMOX structures exposed to the electric field is related to the transformation of the initial electrically inactive centers (formed during the buried SiO_2 layer growth) into electrically active centers acquiring a positive charge. The positive charging of the SiO_2 layer under the joint action of UV radiation and a weak electric field (E_{ox} = 1 MV/cm) is probably also related to the same transformation of electrically inactive into active centers during the buried SiO_2 layer growth, which may be caused by the combined action of two factors as well. Studying this process is the task of our subsequent investigation.

Taking into account that the centroid position of the positive charge appearing as a result of the field application coincides with that of the positive charge formed with the initial SIMOX structure and that the UV irradiation and low-temperature annealing produced identical effects upon the charged state, we may conclude that this charging is related to defects of the same nature. At present, neither the nature of the positively charged centers appearing in SiO_2 during the SIMOX structure formation nor the nature of centers transformed from the electrically inactive to active state as a result of the field application can be explained.

We may only suggest that these defects are probably of the three-coordinated silicon atom type, modified by impurity atoms. The UV irradiation could convert these defects from positively charged to neutral state by trapping electrons optically excited from Si to the conduction band of SiO_2 (this is evidenced by the fact that this recharging took place only in the absence of an applied electric field, which hindered the electron injection from Si into SiO_2). During the SIMOX structure formation, such defects would probably appear at the boundaries of the microcrystalline silicon inclusions (appearing in the buried oxide layer at the SiO_2–Si interface), the presence of which was reported by several researchers [2–4].

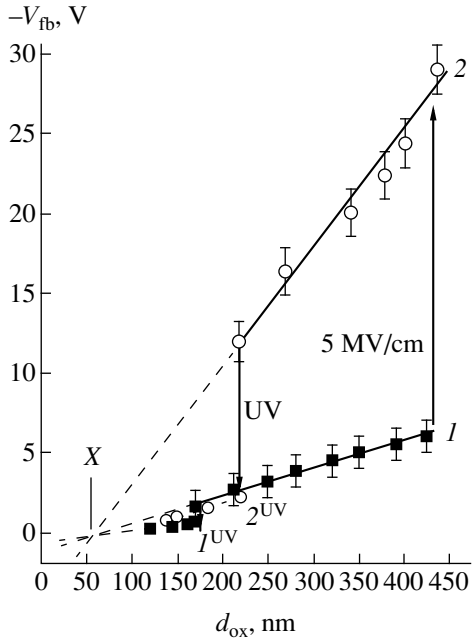

Fig. 2. Plots of the flat-band potential V_{fb} versus oxide layer thickness d_{ox} for SIMOX structures: (*1*) initial; (*2*) field-treated at E_{ox} = 5 MV/cm; (1^{UV}, 2^{UV}) UV-irradiated.

REFERENCES

1. A. P. Baraban, V. V. Bulavinov, and P. P. Konorov, *Electronics of SiO_2 Layers on Silicon* (Leningr. Gos. Univ., Leningrad, 1988).
2. V. V. Afanas'ev, A. Stesmans, and A. G. Revesz, J. Appl. Phys. **82** (5), 2184 (1997).
3. R. E. Stahlbush, G. J. Campisi, *et al.*, IEEE Trans. Nucl. Sci. **NS-39**, 2086 (1992).
4. J. Stoemenos, A. Garcia, *et al.*, J. Electrochem. Soc. **142** (4), 1248 (1995).

Translated by P. Pozdeev

Technical Physics Letters, Vol. 27, No. 5, 2001, pp. 424–426. Translated from Pis'ma v Zhurnal Tekhnicheskoĭ Fiziki, Vol. 27, No. 10, 2001, pp. 62–66.

Oxide–*p*-InSe Heterojunctions on (110)-Oriented InSe Crystal Substrates

V. N. Katerinchuk, Z. D. Kovalyuk, T. V. Betsa, V. M. Kaminskiĭ, and V. V. Netyaga

Institute for Problems in Materials Science, National Academy of Sciences of Ukraine, Chernovtsy, Ukraine

Received July 28, 2000; in final form, January 9, 2001

Abstract—The photoelectric properties of the oxide–*p*-InSe heterojunction formed on the InSe crystal plane parallel to the crystallographic **C** axis were studied. The samples were prepared by thermal oxidation of a single crystal InSe substrate. The spectra of photosensitivity revealed no influence of the surface recombination effects on the heterojunction properties. The capacitance–voltage characteristics showed that the *p–n* junction is sharp and the corresponding energy barrier is 0.17 eV. The charge transfer through the barrier is described within the framework of the diode theory, with a diode coefficient of the current–voltage characteristic being close to unity.

The wide use of polarized and laser beams in various devices stimulated the search for new highly effective analyzers of polarized radiation. A convenient base for such analyzers is offered by anisotropic crystals [1]. These include semiconductors with a layered crystal structure of the $A^{III}B^{VI}$ type, in particular, InSe. Owing to the existence of chemical bonds of the two types (predominantly covalent and the van der Waals type), InSe crystals possess a clearly pronounced layered structure and exhibit significantly anisotropic properties.

We have succeeded for the first time in obtaining an oxide–*p*-InSe heterojunction on a InSe crystal plane parallel to the crystallographic **C** axis; this plane is known to possess a pronounced photopleochroism. Below we report on the photoelectric properties of these heterojunctions.

The samples were prepared using γ-InSe ($R\bar{3}m$) single crystal ingots grown using the Bridgman method. In order to obtain photosensitive samples, the InSe crystals were doped with cadmium; the Cd-doped InSe crystals had a hole type conductivity. The samples were cut from InSe plates cleaved from the ingots in order to be oriented in the principal crystallographic directions [100] and [110] determined by X-ray diffraction. The photoelectric measurements were performed for the (110) crystallographic plane of InSe. The samples with the (110)-oriented surface were subject only to chemical treatments. The final InSe sample surface orientation deviated from (110) by no more than 3.5°. The oxide–*p*-InSe heterojunction on the InSe crystal plane was obtained as described elsewhere [2]. The contacts were prepared using pure indium melt, which adheres well to the sample surface. Low-temperature measurements were carried out in a cryostat maintaining a preset temperature to within ±0.1 K.

The degree of perfection of the (110) crystal surface (parallel to the **C** axis) was confirmed by the results of measurements of the photosensitivity spectra of the oxide–*p*-InSe heterojunctions formed on the InSe(110) surface prepared as described above and on the naturally cleaved (001) crystal surface (perpendicular to the **C** axis). The photosensitivity spectra were excited by a nonpolarized light. The spectra from two crystal surfaces are compared in Fig. 1. As is seen, both spectra exhibit no decrease in the quantum photoefficiency in the short-wavelength region that is usually related to

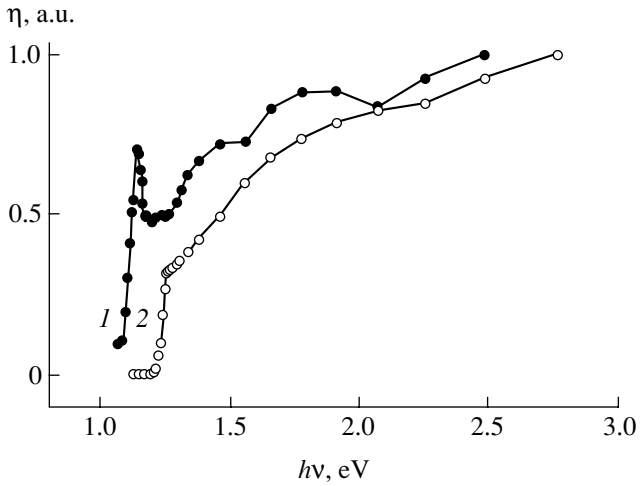

Fig. 1. The spectrum of quantum efficiency of the photocurrent measured at T = 295 K for oxide–*p*-InSe heterojunctions with different orientations: (*1*) **E** ∥ **C**; (*2*) **E** ⊥ **C** (**E** is the electric field vector in the incident light wave; **C** is the crystallographic axis).

1063-7850/01/2705-0424$21.00 © 2001 MAIK "Nauka/Interperiodica"

the surface recombination phenomena [3]. A positive role of the surface oxide layer is to displace the *p–n* junction into the depth of the crystal, where the junction behavior is determined only by the bulk crystal properties.

Since the current in the oxide–*p*-InSe heterojunction flows in the plane parallel to the crystal layers, we studied the mechanism of the charge carrier transfer in a heterojunction oriented relative to the **C** axis as indicated above. As is known, the majority carrier mobility in the InSe crystal layer may reach up to ~1000 $cm^2/(V\ s)$, while that in the perpendicular direction is lower by almost two orders of magnitude [4]. In addition, we measured the capacitance–voltage characteristics of the samples in order to establish the *p–n* junction type and determine the barrier height.

Figure 2 shows the capacitance–voltage characteristics plotted in the C^{-2} versus U coordinates. The linear shape of these plots is indicative of the sharp character of the *p–n* junction. An interesting feature of the capacitance–voltage characteristics obtained is that the cutoff voltage depends on the probing signal frequency. This is explained by the influence of a serial resistance of the heterojunction, including a neutral bulk InSe region and the contact zones [5, 6]. For a correct determination of the barrier potential, the cutoff voltages measured at various frequencies were approximated by interpolating the $U_0(\omega)$ versus ω^2 curve to zero frequency (see the inset to Fig. 2). For the heterojunctions studied, the barrier height was 0.17 V. The same value was obtained for the maximum open-circuit voltage measured upon illuminating the heterojunction. This value of the barrier potential can be used in constructing the energy band diagram of the heterojunction. Note also that this barrier potential is markedly lower than the analogous value measured for the oxide–*p*-InSe heterojunction in the plane perpendicular to the **C** axis (in the latter case, the diffusion potential is 0.5 V [7]).

Figure 3 presents the current–voltage (*I–U*) characteristics of the oxide–*p*-InSe heterojunction measured at various temperatures. As is seen, the slope of the *I–U* curves in their upper part is temperature dependent, while the exponential dependence of current on the applied voltage is described by approximately the same diode coefficient $n \cong 1$. Figure 3 shows that the *I–U* measurements can be performed at a voltage as low as ~0.1 V (corresponding to a small forward bias). A comparison of the experimental data to the theoretical characteristics calculated for the ideal diodes using the diffusion and diode *p–n* junction models showed that the measured *I–U* curves are indicative of the diode mechanism of the current passage through the *p–n* junction, rather than of the diffusion model characterized by the considerably greater forward bias values of the ideal diode curves.

The diode mechanism of conductivity in the oxide–*p*-InSe heterojunction is additionally confirmed by the

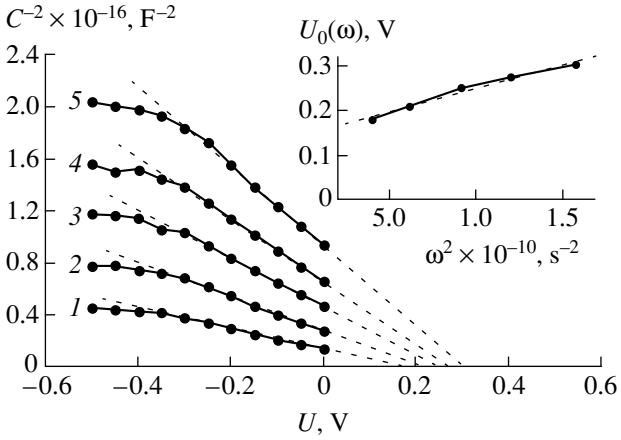

Fig. 2. Capacitance–voltage characteristics of the oxide–*p*-InSe heterojunction (with the *p–n* junction parallel to **C**) measured at various frequencies (kHz): (*1*) 10; (*2*) 12.6; (*3*) 15.2; (*4*) 17.4; (*5*) 20. The inset shows the plot of cutoff voltage versus frequency. T = 295 K.

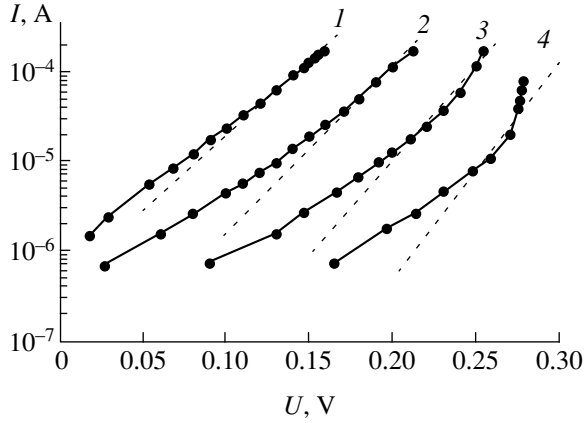

Fig. 3. Current–voltage characteristics of the oxide–*p*-InSe heterojunction (with the *p–n* junction parallel to **C**) measured at various temperatures (K): (*1*) 300; (*2*) 270; (*3*) 240; (*4*) 210. The dashed lines show the ideal diode characteristics.

results of a comparison between the diffusion lengths of charge carriers in the two crystallographic directions. The diffusion length of nonequilibrium carriers determined by the optical probe method for *p*-InSe is $L_{\perp \mathbf{C}} \sim 180$ μm. In the oxide–*p*-InSe heterojunction perpendicular to **C**, the current flows across the crystal layers by the diffusion mechanism [7] and the diffusion length is 3–5 μm [8].

Thus, we have demonstrated that the mechanism of the current passage in the oxide–*p*-InSe heterojunctions depends on the crystallographic orientation of the plane in which the *p–n* junction is formed: the mechanism changes from diode in the plane parallel to the **C** axis to diffusion in the plane perpendicular to this direction. The experimental data show that it is possible to obtain high-quality heterojunctions based on anisotropic InSe

crystals, which is important for the development of photodetectors of both natural and polarized radiations.

REFERENCES

1. N. M. Mekhtiev, Yu. V. Rud', and E. Yu. Salaev, Fiz. Tekh. Poluprovodn. (Leningrad) **12**, 1566 (1978) [Sov. Phys. Semicond. **12**, 924 (1978)].
2. V. N. Katerinchuk and M. Z. Kovalyuk, Pis'ma Zh. Tekh. Fiz. **18** (12), 70 (1992) [Sov. Tech. Phys. Lett. **18**, 394 (1992)].
3. S. Sze, *Physics of Semiconductor Devices* (Wiley, New York, 1981; Mir, Moscow, 1984), Vol. 2, Chap. 14.
4. S. Shigetomi, T. Ikari, Y. Koga, and S. Shigetomi, Jpn. J. Appl. Phys. **20**, L343 (1981).
5. A. M. Goodman, J. Appl. Phys. **34**, 329 (1963).
6. Yu. A. Gol'dberg, O. V. Ivanova, T. V. L'vova, and B. V. Tsarenkov, Fiz. Tekh. Poluprovodn. (Leningrad) **18**, 1472 (1984) [Sov. Phys. Semicond. **18**, 919 (1984)].
7. V. N. Katerinchuk, Z. D. Kavalyuk, and A. V. Zaslonkin, Pis'ma Zh. Tekh. Fiz. **25** (13), 34 (1999) [Tech. Phys. Lett. **25**, 520 (1999)].
8. S. Shigetomi, T. Ikari, Y. Koga, and S. Shigetomi, Jpn. J. Appl. Phys. **27**, 1271 (1988).

Translated by P. Pozdeev

Technical Physics Letters, Vol. 27, No. 5, 2001, pp. 427–430. Translated from Pis'ma v Zhurnal Tekhnicheskoĭ Fiziki, Vol. 27, No. 10, 2001, pp. 67–73.

Cluster Ions in the Field Evaporation Spectra of Lanthanum Hexaboride Measured at Room and Elevated Temperatures

V. N. Gurin, M. M. Korsukova, M. V. Loginov, and V. N. Shrednik

Ioffe Physicotechnical Institute, Russian Academy of Sciences, St. Petersburg, 194021 Russia

Received January 18, 2001

Abstract—The field evaporation of LaB_6 single crystal was studied by the atom probe method at room temperature and at elevated (1145–1260 K) sample point temperatures. The field evaporation spectra of LaB_6 showed a surprisingly large variety of cluster ions: ion species of the LaB_n^{+m} type (n = 1–9; m = 1–4) and $La_2B_n^{+m}$ type (n = 1–15; m = 2, 3) were observed at room temperature, and doubly charged ions of the LaB_n^{+2} type (n = 1–5) were observed in the high-temperature spectra. The physical aspects of this phenomenon are discussed. © *2001 MAIK "Nauka/Interperiodica".*

The experimental data on the field evaporation of lanthanum hexaboride (LaB_6) considered below were obtained with the aid of a time-of-flight atom probe mass spectrometer [1]. In the standard analytical applications, the atom probe measurements are usually performed at very low (cryogenic) temperatures of the object studied. Under these conditions, a polyatomic conductor, alloy, or compound exhibit field evaporation in the atomic form, which allows the local surface composition of an area selected on the sample surface to be readily determined. However, this analytical task is not always the main point in the investigation, especially when the material composition is well known a priori, as in our case. The perfect filament (whisker) LaB_6 crystals were grown from solution in melted aluminum [2]. The stoichiometry and homogeneity of the bulk composition were confirmed by the results of chemical analyses and X-ray diffraction measurements [2].

In the case of multicomponent compounds, the field evaporation behavior of samples is of interest from several (besides analytical) standpoints. The higher the sample temperature, the greater the probability that the material would evaporate in the form of clusters rather than individual atoms. This poses the interesting tasks of determining the composition of cluster ions, their relative content in the evaporated flow, and the nature and stability of these particles. One of these tasks was solved in previous investigations [3, 4], where the content of various charged clusters in the field evaporation flow of LaB_6 was compared with their theoretically calculated relative stabilities. It was demonstrated that less stable or even metastable clusters are found with greater probability in the flow of evaporated ions. In that paper, we considered clusters of the LaB_n^{+m} type (where n = 0–6 and m = 1–4), which are most frequently encountered in the field evaporation of LaB_6 at room temperature. Subsequent experimental investigations in this direction showed that more complicated particles may be present in the field-evaporated ion flow.

An increase in the sample temperature during the field evaporation of multicomponent conductors may be related to another problem, possessing a somewhat more applied character. This problem is related to the task of creating point ion sources, which are promising tools for the development of modern nanotechnologies [5, 6]. An increase in the object temperature allows the evaporation to be performed at a lower field strength (and a lower working voltage). In connection with this, it would be of interest to study the composition of the evaporated material, since this does not always coincide with the bulk composition of the object (i.e., the point). For example, the high-temperature field evaporation of some alloys is accompanied by the surface segregation and preferential evaporation of a component possessing higher surface activity [7, 8]. An important circumstance is that the field evaporation at room temperature considerably simplifies the application technologies involving point ion sources.

In this study, the field evaporation of LaB_6 from the sample point was carried out and the evaporated particles were analyzed at room temperature and at elevated temperatures (T = 1145–1260 K) of the sample. The LaB_6 filaments with a length of 4–7 mm and a thickness of 0.2–0.4 mm were prepared by electrochemical etching in concentrated H_2SO_4 and mounted on the atom probe system anode by gluing with Aquadag or with a conducting epoxy resin. The experiments were per-

1063-7850/01/2705-0427$21.00 © 2001 MAIK "Nauka/Interperiodica"

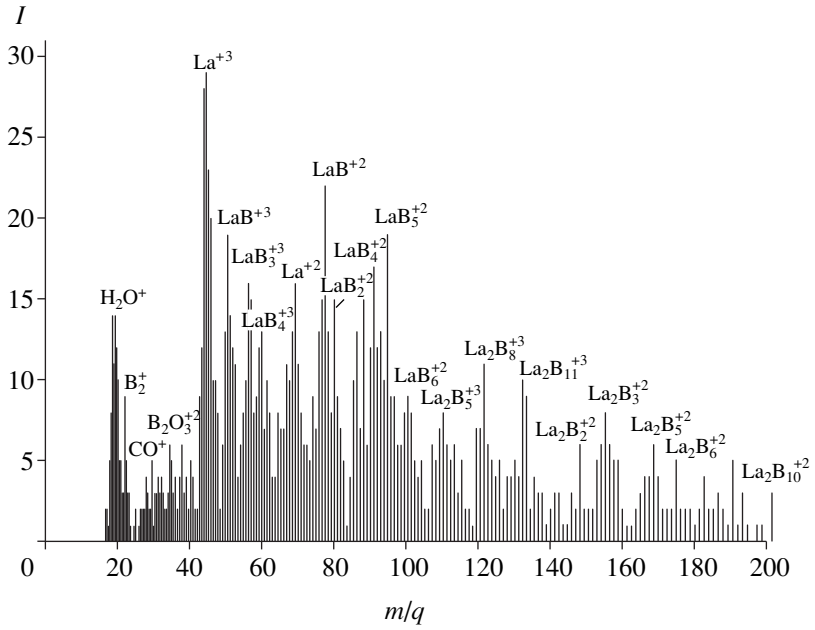

Fig. 1. Room-temperature field evaporation spectrum of LaB_6 measured at a constant base voltage of V_b = 12.5 kV and a pulsed voltage amplitude of V_p = 5.6 kV. Number of informative pulses, h = 919; total number of pulses, N = 8000 (m/q is the ion mass to charge ratio; I is the number of detected ions).

formed with an atom probe mass spectrometer of moderate resolution ($M/\Delta M \geq 30$) described elsewhere [9]. The spectrometer detector system was modified so as to provide for a more than 30-fold increase in the ion collection rate.

Figure 1 shows a typical mass spectrum of LaB_6 measured in the stage of developed field evaporation. In addition to the peaks of boron, lanthanum, and the natural impurities and contaminants (H_2O^+, CO^+), the spectrum reveals a large variety of doubly and triply charged cluster ions of the LaB_n^{+m} type (n = 1–6, m = 2, 3). Moreover, an analysis of several tens of such spectra revealed, besides the above typical species, some other systematically found particles. These include LaB_7^{+2}, LaB_8^{+2}, and LaB_9^{+2}, the peaks of which are well distinguished and not overlapped with the peaks of other species. The corresponding triply charged ions LaB_7^{+3} (with the mass to charge ration m/q = 72), LaB_8^{+3} (76), and LaB_9^{+3} (79.3) are apparently present in the spectra as well, but their peaks fall in the vicinity of the high-intensity peaks of La^{+2} (m/q = 69.5), LaB^{+2} (75), and LaB_2^{+2} (80.5), which frequently mask the former signals.

We also proved the presence of doubly charged ions of the $La_2B_n^{+2}$ type with odd n = 1, 3, 5, …, from which we infer that the neighboring peaks of singly charged ions of the LaB_n^{+} type with n = 1 and above are more likely to represent dimer particles such as $La_2B_2^{+2}$, $La_2B_4^{+2}$, and $La_2B_6^{+2}$. In addition, peaks of the $La_2B_n^{+m}$ type are frequently encountered as triply charged ions (see Fig. 1, $La_2B_5^{+3}$, $La_2B_8^{+3}$, $La_2B_{11}^{+3}$, etc.). These ions can be considered as reliably established because their calculated and measured m/q values frequently coincide to within ±1 amu on the background of m/q = 100–200 (as is the case for the latter three ions for which the measured m/q values are 110, 121, 132 and the calculated values are 111, 122, 133, respectively).

Finally, an analysis of the mass spectra gave us grounds to suggest that the field-evaporated ion flow from LaB_6 contains a small amount of still heavier polymeric cluster ions such as $(LaB_n)_3^{+m}$. In the field evaporation spectra of CeB_6 (a compound analogous to LaB_6), such ion species form peaks of significant intensity [10]. Thus, a sharply nonequilibrium process of disintegration of the LaB_6 crystal lattice by field evaporation at room temperature gives rise to a surprisingly large variety of cluster ions, which are stable during a time at least equal to the flight time in the instrument (on the order of 1 μs). Although the mechanism of formation of these ions is not completely clear (and has to be elucidated), the existence of these chemically nonequilibrium species can be considered as proved.

As for the problem of the segregation of some component on the LaB_6 surface and the presence of the corresponding ions in the flow of field-evaporated particles, this is most likely for lanthanum whose peaks (La^{+3}, La^{+2}) in the field evaporation spectra are most

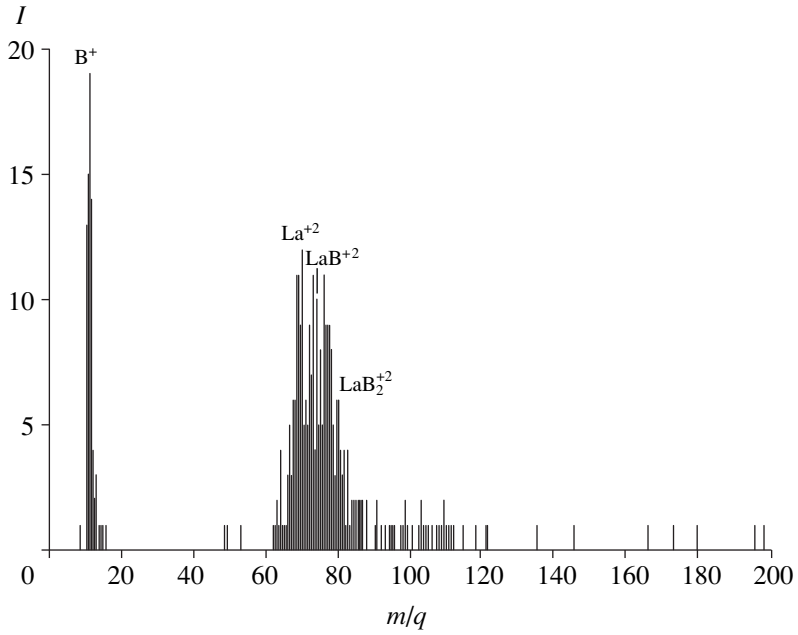

Fig. 2. Field evaporation spectrum of LaB_6 measured at T = 1235 K (V_b = 0; V_p = 6.2 kV; h/N = 310/10000).

intense and numerous. Also well distinguished are the peaks of lanthanum-rich cluster ions LaB^{+3} and LaB^{+2}. The enrichment of the evaporated ion flow with lanthanum (relative to the bulk LaB_6 crystal composition) is related to the process of pulling the lanthanum atoms (freely migrating over the crystal surface) into the strong field region. This phenomenon is considered in more detail in [11].

The experiments with the field evaporation of LaB_6 at elevated temperatures (T = 1140–1260 K) were performed using a zero base voltage (V_b = 0) and a pulsed probing voltage with a pulse width of 10^{-8} s and an amplitude of V_p = 4.8–6.2 kV. At high temperatures, the evaporation at a nonzero V_b may distort the spectrum by introducing spurious signals. The spectra measured in the $(0 + V_p)$ regime leave no doubts concerning the analytical reliability of the data, since no single component can be selectively lost (as for $V_b \neq 0$). In our high-temperature field evaporation experiments, the evaporating field and voltage were significantly reduced (by a factor of 3–5) as compared to those used in the room-temperature measurements. Accordingly, the quality of the spectra (resolution) also decreases because the field evaporation takes place not only at the peak of a voltage pulse, but on approaching this value as well.

Figure 2 shows an example of the field evaporation pattern observed at T = 1235 K and $V_b + V_p = 0 +$ 6.2 kV. The spectrum exhibits a narrow peak of B^+ (or B_2^{+2}) and a group of doubly charged ions from La^{+2} to LaB_2^{+2}. On the whole, all ten spectra measured in this series showed broadened, poorly resolved peaks of doubly charged ions from La^{+2} to LaB_4^{+2}. The maxima of these peaks corresponded to La^{+2}, LaB^{+2}, or LaB_2^{+2}. Excess boron was eliminated in the form of atomic or cluster ions (B^+, B_2^{+2}, etc.). The differential curves of ion accumulation (measured separately for boron and cluster ions) sometimes showed evidence for a parallel evaporation, and in other cases, for a boron accumulation followed by sharp (high-rate) evaporation. The absence of triply charged ions in these experiments is a quite natural result, since the evaporation took place at a considerably weaker electric field strength as compared to that used in the room-temperature measurements. At high temperatures, the LaB_6 lattice also disintegrates in a highly nonequilibrium manner: LaB_6 molecules prevail in the flow of evaporated particles and decay according to the scheme $LaB_6 = LaB_n + B_{6-n}$. The high-temperature field evaporation spectra showed no evidence of dimerization (the more so, of polymerization) of the LaB_n clusters.

In concluding, it should be noted that the field evaporation spectra of some compounds measured at cryogenic temperatures also contain both atomic and cluster ions. For example, this phenomenon was repeatedly observed for cuprate–oxide high-temperature superconductors. The field evaporation spectra of these compounds measured at liquid nitrogen temperature displayed peaks due to various oxides of copper and other metals [12, 13]. For the high-temperature superconductors, representing complex multielement compounds possessing a complicated unit cell, this pattern of disintegration is quite reasonable. However, recently we studied the field evaporation of carburized tungsten

(with a surface carbide film possessing a simple WC composition) and observed WC_3^{+2}, W_2C^{+3}, and even dimer $(W_2C)_2^{+3}$ ions in the surface carbide spectra measured both at room temperature and upon cooling the sample point with liquid nitrogen. Thus, even simple binary compounds may exhibit the formation of complex clusters at room and lower temperatures. These facts indicate that interesting results can be also expected for incompletely studied field evaporation processes in refractory compounds at various temperatures.

Acknowledgments. This study was performed within the framework of the "Surface Atomic Structures" Program supported by the Ministry of Science and Technology of the Russian Federation (project no. 4.12.99).

REFERENCES

1. M. K. Miller and G. D. W. Smith, *Atom Probe Microanalysis: Principles and Applications to Material Problems* (Materials Research Society, Pittsburgh, 1989; Mir, Moscow, 1999).
2. M. M. Korsukova and V. N. Gurin, Usp. Khim. **56**, 3 (1987).
3. I. Bustani, R. Byunker, G. Khirsh, *et al.*, Pis'ma Zh. Tekh. Fiz. **25** (23), 43 (1999) [Tech. Phys. Lett. **25**, 944 (1999)].
4. I. Boustani, R. Buenker, V. N. Shrednik, *et al.*, J. Chem. Phys. (2001) (in press).
5. V. N. Shrednik, Poverkhnost, No. 2, 102 (1998).
6. M. V. Loginov and V. N. Shrednik, *Proceedings of the All-Union Conference "Microprobe-98"* (Inst. Fiz. Mikrostruktur Ross. Akad. Nauk, Nizhni Novgorod, 1998), p. 119.
7. M. V. Loginov and V. N. Shrednik, Zh. Tekh. Fiz. **68** (3), 69 (1998) [Tech. Phys. **43**, 327 (1998)].
8. E. L. Kontorovich, M. V. Loginov, and V. N. Shrednik, J. Vac. Sci. Technol. B **15** (2), 495 (1997).
9. M. V. Loginov, O. G. Savel'ev, and V. N. Shrednik, Zh. Tekh. Fiz. **64** (8), 123 (1994) [Tech. Phys. **39**, 811 (1994)].
10. V. N. Gurin, M. M. Korsukova, M. V. Loginov, and V. N. Shrednik, Pis'ma Zh. Tekh. Fiz. **27** (10), 74 (2001) [Tech. Phys. Lett. **27**, 431 (2001)].
11. V. N. Gurin, M. M. Korsukova, M. V. Loginov, and V. N. Shrednik, Zh. Tekh. Fiz. **71** (2001) (in press) [Tech. Phys. **46** (2001) (in press)].
12. M. V. Loginov, O. G. Savel'ev, and V. N. Shrednik, Zh. Tekh. Fiz. **64** (9), 144 (1994) [Tech. Phys. **39**, 938 (1994)].
13. V. N. Shrednik, Prog. Surf. Sci. **42** (1–4), 131 (1993).

Translated by P. Pozdeev

Technical Physics Letters, Vol. 27, No. 5, 2001, pp. 431–433. Translated from Pis'ma v Zhurnal Tekhnicheskoĭ Fiziki, Vol. 27, No. 10, 2001, pp. 74–78.

Field Evaporation of Cerium Hexaboride

V. N. Gurin, M. M. Korsukova, M. V. Loginov, and V. N. Shrednik

Ioffe Physicotechnical Institute, Russian Academy of Sciences, St. Petersburg, 194021 Russia

Received January 18, 2001

Abstract—The field evaporation of CeB_6 single crystal was studied by the atom probe method. The field-evaporated ion flow contains Ce^{+4} ions and polymeric clusters of the $(CeB_n)_k^+$ type (n = 1–6; k = 2, 3). This pattern is significantly different from that observed for a typical field evaporation spectrum of LaB_6, a compound analogous to CeB_6. The difference is explained by the higher strength of the crystal lattice of CeB_6 and by the tetravalent character of cerium. © *2001 MAIK "Nauka/Interperiodica".*

Single crystals of cerium hexaboride CeB_6, as well as those of lanthanum hexaboride LaB_6, are interesting objects for investigation—both from the practical standpoint of creating effective electron and ion emitters and from the standpoint of fundamental investigations of interatomic bonds. Field evaporation is a phenomenon responsible for the ion formation in a strong electric field involving, in particular, the breakage of certain bonds in the surface layer of evaporated materials. The field evaporation of multicomponent conductors leads to the formation of complex molecular (radical, cluster) ions, the nature of which is also determined by the relative strength of various interatomic bonds. Therefore, our study of the field evaporation of hexaborides including the atom probe analysis of the evaporation products is of importance for both solid state physics and emission electronics.

The previous study [1] of the room-temperature field evaporation of LaB_6 revealed a large number of charged clusters of the LaB_n^{+m} type (n = 0–6, m = 1–4) in the evaporated ion flow. The field evaporation spectra measured using the atom probe method [2] characterized the distribution of various clusters in the evaporated products, the crystal surface composition, and the impurities determined under various experimental conditions (electric field strength, temperature, etc.). Below we report for the first time on the atomic probe study of the field evaporation of cerium hexaboride, which is the closest analog of lanthanum hexaboride.

The filament crystals of CeB_6 used for the preparation of point emitters were grown from a solution in melted aluminum [3]. A sample crystal was fastened to a tantalum arc (that could be heated by passing current) with the aid of Aquadag, then etched so as to form a sharp point in concentrated H_2SO_4, and mounted in a time-of-flight atomic probe mass spectrometer described in detail elsewhere [4]. The spectrometer detector system was modified so as to provide for a more than 30-fold increase in the ion collection rate, which reduced the time of obtaining statistically reliable spectra. The field evaporation experiments were conducted at room temperature.

We recorded more than ten informative field evaporation spectra of CeB_6 crystals, one of which is presented in the figure. This measurement was preceded by taking three spectra, two of which were recorded under the same applied voltage (constant base voltage, V_b = 11 kV; pulsed voltage amplitude, V_p = 5.6 kV) and one, at a higher constant voltage V_b = 12 kV and the same pulsed component. As a result, the point surface corresponding to the spectrum presented in the figure was cleaned from impurities; the measurement at V_b = 12 kV somewhat blunted the point tip, thus ensuring that the field evaporation at V_b = 11 kV on the pedestal is negligibly small as compared to that at the pulse peak. The final spectrum contained a small amount of noise signals and correctly represented the evaporated ion flow composition. Irrespective of this pretreatment, the ratio of the pulsed component to total voltage amplitude $V_p/(V_b + V_p) = 5.6/16.6 = 0.34$ is indicative of a correct spectrum.

Below we compare the results obtained for CeB_6 to the data for LaB_6, the field evaporation of which was previously studied in much detail. It should be noted that, prior to these experiments, no considerable differences between the room-temperature field evaporation spectra of CeB_6 and LaB_6 were expected because of the chemical similarity of these two crystalline compounds. However, already the first measurements revealed a significant difference in the field evaporation behavior of cerium and lanthanum hexaborides. There are two principal distinctions: (i) the main peak of the rare-earth metal, which is especially pronounced when the surface is enriched with this component, is La^{+3} for LaB_6 and always Ce^{+4} for CeB_6; (ii) in the spectrum of LaB_6, the LaB_n^{+m} clusters were predominantly monomers (dimer species being few and seldom); in the

1063-7850/01/2705-0431$21.00

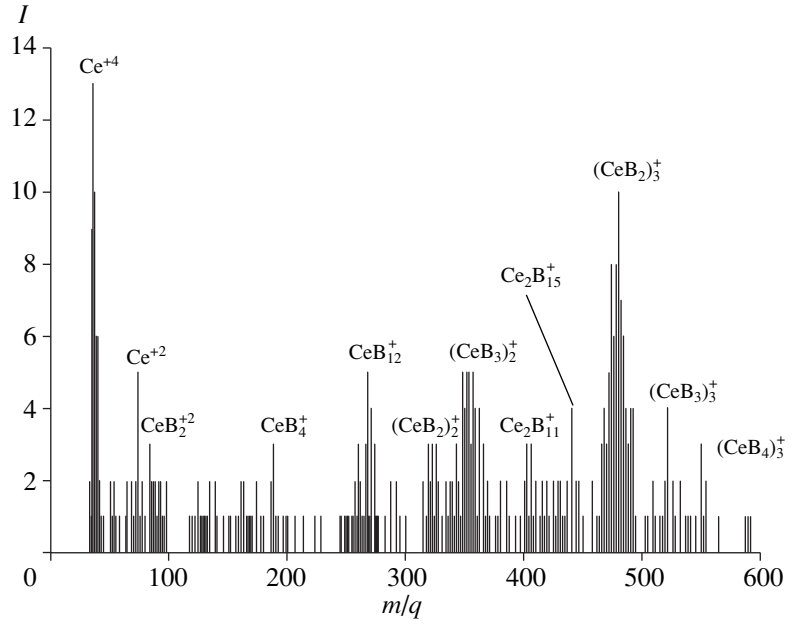

Room-temperature field evaporation spectrum of a CeB_6 single crystal measured in a time-of-flight atom probe mass spectrometer at a constant base voltage of V_b = 11 kV and a pulsed voltage amplitude of V_p = 5.6 kV. Number of informative pulses, h = 200; total number of pulses, N = 2035; residual pressure in the atom probe chamber, 10^{-10} Torr (m/q is the ion mass to charge ratio; I is the number of detected ions).

spectrum of CeB_6, the most intense peaks corresponded to dimer (and polymerized to a greater extent–trimer and so on) cluster ions, rather than relatively light monomer ions (although these were also present). Both these features are well pronounced in the spectrum presented in the figure, showing a high peak of Ce^{+4} and relatively large peaks of $(CeB_2)_3^+$ and $(CeB_3)_2^+$.

An analysis of this and the other spectra, measured either in the same regime ($V_b + V_p$ = 11 + 5.6 kV) or at V_p = 6.2 kV and V_b varied from 10.4 to 14 kV, led us to the following conclusions. (i) In the region of small masses (low mass to charge ratio m/q), most frequently formed ions are Ce^{+4} (observed almost in all spectra); somewhat less frequently detected are CeB^{+4} and B_3^+ (or B_6^{+2}); and still less frequently observed are various triply and doubly charged ions of the CeB_n^{+m} type. (ii) In the region of dimers, the most frequently observed ions are $(CeB_3)_2^+$ and $(CeB_4)_2^+$ and somewhat less frequently detected are $(CeB)_2^+$ and $(CeB_2)_2^+$. (iii) In the region of trimers, the most frequently found ions are $(CeB_2)_3^+$ and somewhat less frequently observed are $(CeB)_3^+$.

The polymeric ions are not always formed with an exactly preset number of boron atoms. Rather frequently (especially in the case of intense field evaporation), a peak in the region of $(CeB_2)_3^+$ (that is, $Ce_3B_6^+$) appears as sufficiently broad and covers the neighboring regions with deficient and/or excess boron (i.e., $Ce_3B_5^+$ and $C_3B_7^+$). The same is valid for dimer peaks. Finally, there are grounds to suggest that the spectrum represents doubly charged dimer ions rather than singly charged monomer particles, for example, $(CeB_4)_2^{+2}$ instead of CeB_4^+ (mass spectra recorded with usual resolution cannot distinguish these species). The peaks may also contain clusters corresponding to a greater degree of polymerization, with deficient or excess boron atoms (the m/q values differing by ±5.5, which corresponds to half of the atomic weight of boron).

We believe that the observed distinctions between the room-temperature field evaporation spectra of LaB_6 and CeB_6 are probably related to features of the crystal lattices of these substances and the electron properties of the two metal atoms. The compounds of lanthanum are usually characterized by the metal valence +3, while cerium is observed in both +4 and +3 valence states [5]. Therefore, free cerium atoms leaving the surface under the action of a strong electric field usually loses four electrons. The crystal lattices of LaB_6 and CeB_6, while being structurally identical, differ by the unit cell parameters (4.1569 Å for LaB_6 versus 4.1396 Å for CeB_6 [6]) and by the interoctahedral B–B bond length (1.659 Å versus 1.650 Å). A difference in the second decimal digit between the equilibrium bond

length implies a considerable difference between the cohesion forces: the lattice of CeB_6 (especially the boron framework) is stronger than the lattice of LaB_6. This is apparently manifested by the greater probability of forming polymeric ions during the field evaporation of CeB_6. This general explanation is rather clear. At the same time, it is still incompletely clear what mechanism is responsible for the formation of polymeric cluster ions with the monomer representing a fragment of the unit cell; such fragments are nevertheless capable of combining with the formation of, for example, frequently encountered ions such as $(CeB_2)_3^+$ or (which is much more surprising) $(CeB_2)_6^{+2}$. This point is worthy of being studied in more detail in subsequent experiments.

In conclusion, it is necessary to point out the following circumstance. The field evaporation mass spectra of CeB_6 typically contain peaks corresponding to pure cerium ions or clusters of the CeB_2 of CeB_3 types, rather than to CeB_6. This fact indicates that cerium is present in excess in the field evaporated ion flow (against the CeB_6 stoichiometry). This excess is not be always compensated by ions forming the peak of B_3^+ (even assuming this to represent B_6^{+2} or B_9^{+3}). The excess of cerium, as well as the excess of lanthanum in the spectra of LaB_6 [1], is apparently explained by the presence of excess cerium atoms on the CeB_6 point surface. Freely migrating at room temperature, these cerium atoms are pulled by the strong electric field toward the point tip. This circumstance can be used for creating an effective point source of cerium ions or, at least, a source enriched with cerium atoms.

Acknowledgments. This study was performed within the framework of the "Surface Atomic Structures" Program supported by the Ministry of Science and Technology of the Russian Federation (project no. 4.12.99).

REFERENCES

1. I. Bustani, R. Byunker, G. Khirsh, *et al.*, Pis'ma Zh. Tekh. Fiz. **25** (23), 43 (1999) [Tech. Phys. Lett. **25**, 944 (1999)].
2. M. K. Miller and G. D. W. Smith, *Atom Probe Microanalysis: Principles and Applications to Material Problems* (Materials Research Society, Pittsburgh, 1989; Mir, Moscow, 1999).
3. V. N. Gurin and M. M. Korsukova, Prog. Cryst. Growth Charact. **6**, 59 (1983).
4. M. V. Loginov, O. G. Savel'ev, and V. N. Shrednik, Zh. Tekh. Fiz. **64** (8), 123 (1994) [Tech. Phys. **39**, 811 (1994)].
5. B. V. Nekrasov, *Foundations of General Chemistry* (Khimiya, Moscow, 1967), Vol. 2.
6. M. Korsukova, Jpn. J. Appl. Phys. Ser. 10, 15 (1994).

Translated by P. Pozdeev

Technical Physics Letters, Vol. 27, No. 5, 2001, pp. 434–436. Translated from Pis'ma v Zhurnal Tekhnicheskoĭ Fiziki, Vol. 27, No. 10, 2001, pp. 79–85.

The Effect of Passive Q-switching Observed in an Erbium-Doped Fiber Laser at a Low Pumping Power

A. A. Fotiadi, R. V. Kiyan, and O. V. Shakin

Ioffe Physicotechnical Institute, Russian Academy of Sciences, St. Petersburg, 194021 Russia

Received December 19, 2000

Abstract—The effect of passive Q-switching was observed in an erbium fiber laser at a pumping power below 100 mW. The phenomenon is explained by a cascade process of the Rayleigh light scattering and the induced Mandelshtam–Brillouin scattering in a fiber resonator of the laser. In the Q-switched mode, the laser produced giant output pulses with a duration below 15 ns, a peak power up to 200 W, and a repetition period of 300–500 μs. The proposed Q-switching mechanism is inferred from the characteristic features of the laser pulse oscillograms measured at a ~1 ns resolution. Previously, this effect was observed only in high-power fiber lasers at a pumping power of ~2 W. © *2001 MAIK "Nauka/Interperiodica".*

Introduction. In recent years, considerable progress has been achieved in the development of lasers based on optical fibers doped with rare-earth elements. Most widely employed are fiber lasers using ytterbium- and erbium-doped fibers, emitting in the 1.0–1.2 and 1.52–1.58 μm wavelength intervals [1, 2]. A possible direction for further development of the fiber lasers consists in creating new fiber optic configurations employing both the traditional inverse population scheme and some other mechanisms of light energy conversion, in particular, the phenomena of linear and nonlinear light scattering in the fiber [3, 4].

The mechanism of passive Q-switching based on Rayleigh scattering (RS) and induced Mandelshtam–Brillouin scattering (IMBS) in fiber lasers was originally proposed [5] in connection with the study of dynamics of a high-power Yb-doped fiber laser [6]. At a pumping power of ~2 W, the Yb-doped fiber laser produced giant pulses with a peak power of up to 10 kW and a pulse duration below 5 ns. The essence of the RS–IMBS mechanism is that the Rayleigh light scattering gives rise to a distributed feedback in the laser resonator, thus leading to a decrease in the fiber laser bandwidth and providing conditions for the IMBS cascade development in the fiber resonator. The avalanche IMBS dynamics accounts for the giant laser pulse production [7, 8].

In our experiments, the passive Q-switching mode in the Er-doped fiber laser was achieved at a pumping power 50 times lower than that used in [6]. For an optimum laser geometry and a ~90 mW pumping from a semiconductor laser diode, the Er laser generated a series of pulses with a duration below 15 ns and a peak power of up to 200 W. A detailed study of the laser radiation structure using a high-speed digital oscillograph ensuring a ~1 ns resolution revealed several important features in the fine structure of laser pulses, which clearly indicated a mechanism responsible for their production. In particular, it was established that a giant laser pulse is always preceded by a precursor pulse with a peak power below 5 W and a duration of 50–200 ns. The precursor has a characteristic extended leading front and is separated from the giant pulse by a time interval equal to or shorter than the time of light travel in the linear resonator. The higher the Q-switching efficiency, the smaller the ratio of these times. These observations are in compete agreement with the RS– IMBS scattering model [7, 8].

Experimental. In our experiments, the known fiber laser configuration [6] was implemented using an Er-doped fiber pumped at a wavelength of 0.980 μm with a single-mode laser diode. The maximum output power of the pumping laser did not exceed 100 mW.

Figure 1 shows a schematic diagram of the fiber laser. The laser comprises two coupled fiber resonators, ring-shaped and linear, coupled by a 10/90 fiber X-coupler *1*. The ring resonator *2* represented a 2-m-long

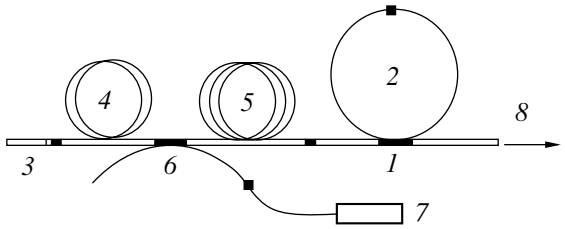

Fig. 1. A schematic diagram of the Er-doped fiber laser configuration: (*1*) 10/90 fiber coupler; (*2*) 2-m-long ring-shaped resonator; (*3*) Bragg fiber grating with a 90-% reflectance at 1.532 μm; (*4*) 7-m-long Er-doped fiber amplifier; (*5*) single-mode fiber (with a length of ~8 or 44 m for the short- and long-resonator configurations); (*6*) WDM fiber coupler; (*7*) single-mode 0.98-μm pumping laser diode; (*8*) laser output.

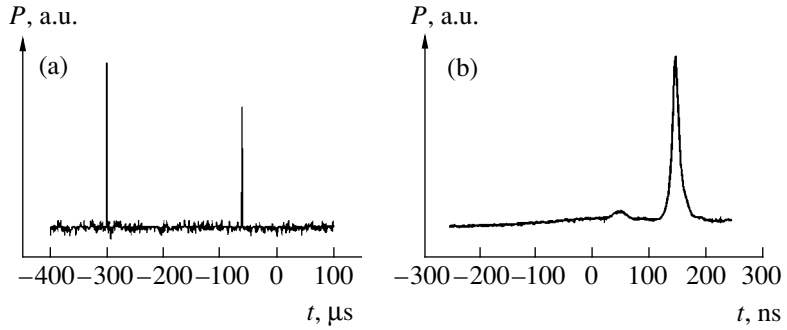

Fig. 2. Characteristic oscillograms of the output signal measured on the (a) microsecond and (b) nanosecond scale for a fiber laser with short linear resonator pumped at 80 mW.

piece of a standard single-mode fiber. The linear resonator comprised a Bragg fiber grating *3* with a 90% reflectance at 1.532 μm, a 7-m-long Er-doped fiber amplifier *4*, and a piece of a standard single-mode fiber *5*. A WDM coupler *6*, connected to the linear resonator between the Er-doped fiber *4* and fiber *5*, pumped the laser with radiation of a laser diode *7*.

A signal at the laser output *8* was registered using a Ge photodiode. The photodiode response was digitized and recorded in a storage oscillograph for subsequent processing. The detection scheme provided a time resolution of ~1 ns. The laser dynamics was studied for two configurations differing by the length (8 or 44 m) of a single-mode fiber *5* in the linear resonator.

Results. The experiments revealed two qualitatively different operation regimes in the laser scheme depicted in Fig. 1. In the first case, a feedback in the linear resonator was provided by a 2–4% reflection from the free fiber end at the laser output. At a pumping power of 30–100 mW, the output laser signal represented a noise-modulated continuous signal with an average power of ~10–30 mW. No regular intensity variations above the noise level were observed in the output signal of the laser operating in this mode. The laser emission line was centered at 1.532 μm.

Qualitatively different behavior was observed when the free-end reflection was suppressed and the feedback was provided by the natural Rayleigh light scattering in the ring resonator. When the pumping power was increased to ~90 mW, the laser spontaneously passed into a regime of generating a continuous sequence of giant pulses spaced by ~300–500 μs. The output pulse amplitude fluctuations reached ~50%.

The pulsed lasing could be observed at a lower pumping power as well. A typical oscillogram of laser pulses is presented in Fig. 2. A correct cleavage of the fiber edge at an angle minimizing the reflection at the laser output allowed the pumping threshold, corresponding to the spontaneous generation of giant pulses, to be reduced down to ~70 mW. A weak acoustic action upon the laser resonator ensured the giant pulse generation at a pumping power as low as ~30 mW.

It should be noted that the method of giant pulse excitation did not affect the characteristic features of the output pulses, which were determined only by the laser configuration and the pumping power level. At a pumping power of ~90 mW in the configuration with a short linear resonator, the output peak power reached ~10 W at a pulse duration of ~40–50 ns (the latter parameter was much more stable than all other pulse characteristics). At the same pumping power, the configuration with a long linear resonator provided for a more effective Q-switching. In this case, the output pulses were stronger and shorter: the peak power reached 100–200 W at a pulse duration reduced to 10–20 ns.

A characteristic feature of the laser dynamics determined by the RS–IMBS mechanism [5–8] is the presence of a precursor signal, representing a weak pulse preceding the giant output pulse. The precursors observed in the output laser radiation are easily distinguishable in the oscillogram shown in Fig. 2b. The precursor peak power never exceeded 5 W at a characteristic duration of 50– 200 ns.

The fine temporal structure of laser oscillations preceding the giant pulse production was studied for both laser resonator configurations. Figure 3a shows an oscillogram of the output radiation pulses observed in the laser with a short linear resonator. This pattern illustrates the dynamics of the giant pulse formation, in which several stages can be clearly distinguished. The initial slow growth with a characteristic time of ~70 ns is changed by the generation of a small precursor pulse (point *1*), followed by a drop separating the precursor from the giant pulse (point *2*). It must be noted that these features are present in all oscillograms measured for this laser configuration. The characteristic signal growth time on the left of point *1* might differ in various oscillograms but was always shorter than ~80 ns. The time interval between the precursor *1* and giant pulse *2* onset points was ~80 ns, which corresponds to double the time of light wave travel in the linear resonator.

A similar time pattern of the output signal was observed for the laser configuration with a long linear resonator. A typical oscillogram of this signal is presented in Fig. 3b. On the whole, this pattern repeats the

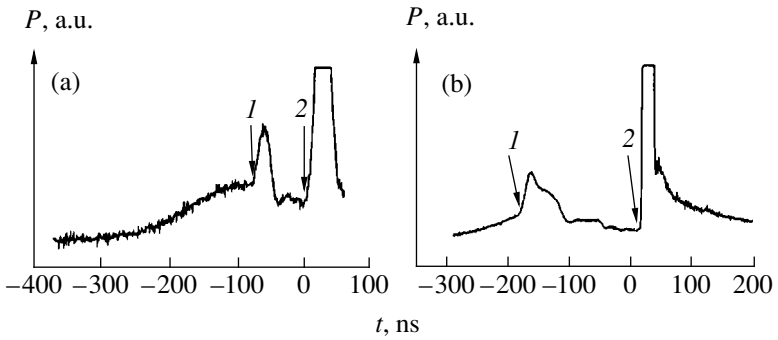

Fig. 3. Characteristic oscillograms showing fine structure of the output signal measured for a fiber laser with (a) short and (b) long linear resonator pumped at 80 mW. Points *1* and *2* indicate the onset of precursor and giant laser pulses.

characteristic features observed for the above base configuration, showing a slow portion, precursor, and giant pulse. However, the precursor and giant pulse onset points (*1* and *2*, respectively) are separated by a time interval which fluctuated within ~200–400 ns, being always shorter than double the time of light wave travel in the linear resonator (~440 ns). In the typical oscillogram presented in Fig. 3b, this interval equals ~200 ns. In addition, we noted that the time interval between the precursor and giant pulses decreased with increasing efficiency of the Q-switching.

On the whole, a comparison of these data to the results obtained for the fiber lasers operating at a large pumping power [5, 6] showed that the output signal dynamics is much simpler in the case of a low pumping power. Here, the pulse formation process is slower and exhibits clearly separated stages readily classified within the framework of the RS–IMBS model [7, 8]. We observed no indications of any other nonlinear optical effects (besides IMBS) influencing the process dynamics.

Conclusion. Thus, we have successfully realized experimentally the mechanism of passive Q-switching based on the joint process of Rayleigh light scattering and induced Mandelshtam–Brillouin scattering in an Er-doped fiber laser operating under abnormally low diode pumping power conditions. Pumped at 90 mW, the fiber laser generated a sequence of pulses with a duration below 15 ns and a peak power reaching up to 200 W. The experimental data revealed certain features in the fine structure of the output laser pulses, which clearly indicated a mechanism responsible for their production. The observed effects can be used for the creation of novel laser light sources.

A detailed comparison of the results of experimental measurements and the calculations performed within the framework of the RS–IMBS model will be carried out in the following publications.

Acknowledgments. This study was supported by the Russian Foundation for Basic Research, project no. 00-02-16903.

REFERENCES

1. *Rare Earth Doped Fiber Lasers and Amplifiers*, Ed. by M. J. F. Digonnet (Marsel Dekker, New York, 1993).
2. E. Desurvire, *Erbium-Doped Fiber Amplifiers* (Wiley, New York, 1994).
3. G. Agrawal, *Nonlinear Fiber Optics* (Academic, San Diego, 1995; Mir, Moscow, 1996).
4. E. A. Kuzin, M. P. Petrov, and A. A. Fotiadi, in *Optical Phase Conjugation*, Ed. by M. Gower and D. Proch (Springer-Verlag, Berlin, 1994), pp. 74–96.
5. S. V. Chernikov and A. A. Fotiadi, in *Digest of Technical Papers of the Conference on Lasers and Electro-Optics, 1997* (Optical Society of America, Washington, DC, 1997), p. 477.
6. S. V. Chernikov, Y. Zhu, J. R. Taylor, and V. P. Gapontsev, Opt. Lett. **22**, 298 (1997).
7. A. A. Fotiadi, R. V. Kiyan, and S. V. Chernikov, Proc. SPIE **3685**, 52 (1999).
8. A. A. Fotiadi and R. V. Kiyan, *Ioffe Institute Prize Winners: Abstracts of the Papers Awarded in 1997* (Ioffe Physico-Technical Institute, St. Petersburg, 1998), pp. 43–48.

Translated by P. Pozdeev

Technical Physics Letters, Vol. 27, No. 5, 2001, pp. 437–440. Translated from Pis'ma v Zhurnal Tekhnicheskoĭ Fiziki, Vol. 27, No. 10, 2001, pp. 86–94.

The Effect of Temperature on the Electron Work Function of Adsorbed Europium Films on Tungsten and Silicon Surfaces

M. V. Kuz'min and M. A. Mittsev

Ioffe Physicotechnical Institute, Russian Academy of Sciences, St. Petersburg, 194021 Russia

Received November 9, 2000

Abstract—The temperature dependence of the electron work function φ was studied for the clean surfaces of tungsten (textured ribbons with predominant (100) surface orientation) and silicon ((111)-oriented single crystals), as well as for the same substrates covered with adsorbed europium films. It was found that the φ value may exhibit significant reversible variations reflecting temperature-dependent atomic and electronic processes occurring on the substrate surface. © *2001 MAIK "Nauka/Interperiodica".*

Introduction. As is known, one of the most widely used methods of obtaining heteroepitaxial films consists in depositing a foreign substance onto a substrate surface, which is heated to a certain temperature either during or after deposition. Therefore, a question arises as to how the properties (including the electronic and dynamic characteristics) of the films at high temperatures of the synthesis vary in comparison with the same properties at room (or even lower) temperatures at which the heterostructures are employed. One may suggest that this question refers primarily to the properties of metal–semiconductor and/or semiconductor–semiconductor boundaries formed in the structures studied. This suggestion is based on the fact that the formation of such interfaces is frequently accompanied by reconstruction of the substrate surface, which may significantly depend on the temperature.

As yet, no systematic investigations of the effect of temperature on the electron state of adsorbed films has been reported. The few available publications [1–5] do not form a consistent pattern. Therefore, the task of this investigation was to answer the above question for some particular systems of the adsorbed film–substrate type, that is, the systems formed in the early stages of interface development. For this study, we selected two systems of this type. The first is a single crystal silicon (exposing (111) face with a 7×7 structure) with adsorbed europium film. According to the data reported previously [6], the process of deposition and ordering (at elevated temperatures) of the adsorbed europium layer is accompanied by rearrangement of the silicon surface, whereby the 7×7 structure is reconstructed so that the adsorbed metal atoms and silicon (one or a few surface layers) are arranged in a certain consistent manner (self-organizing system). These results give grounds to expect that the state of this self-organizing system must be temperature-dependent.

The second model system is the surface of tungsten (textured ribbons with (100) face predominantly emerging at the surface), also with an adsorbed europium film. It was expected that the tungsten surface is much less subject to the adsorption-induced surface reconstruction than the silicon surface. Therefore, the effect of temperature on the state of this system was also expected to be less pronounced than that of silicon.

Experimental. The investigation was performed using the methods of low-energy electron diffraction (LEED), Auger electron spectroscopy (AES), thermodesorption spectroscopy (TDS), and the electron work function measurement using the Anderson technique. The latter technique consists of the contact potential difference (CPD) determination by measuring a shift of the current–voltage characteristic of an electron gun. In this combination of methods, one of the most important roles belonged to the CPD measurements. This method provides for a high-precision (to within 0.01 eV) determination of the electron work function—a quantity that is extremely sensitive to the electron state of atoms occurring on the solid surface.

The degree of surface coverage by the adsorbate was determined as $\theta = N(\mathrm{Eu})/N$, where N(Eu) is the concentration of adsorbed Eu atoms and N is the surface density of substrate atoms. For the W(100) crystal face, the latter value is 1×10^{15} cm^{-2} and for the Si(111) surface, $N = 7.84 \times 10^{14}$ cm^{-2}. Europium atoms were adsorbed on the substrates heated to temperatures at which the adsorbed films are known to exhibit complete ordering. For tungsten, these are temperatures in the region of 1000–1200 K, and for silicon, in the vicinity of 1000 K.

The experimental procedure was as follows. After deposition of the europium film, the substrate was cooled to room temperature and then heated in a stepwise manner, with the $\Delta\varphi = \varphi(T) - \varphi(300\ \mathrm{K})$ difference determined on each step, where $\varphi(T)$ and $\varphi(300\ \mathrm{K})$ are

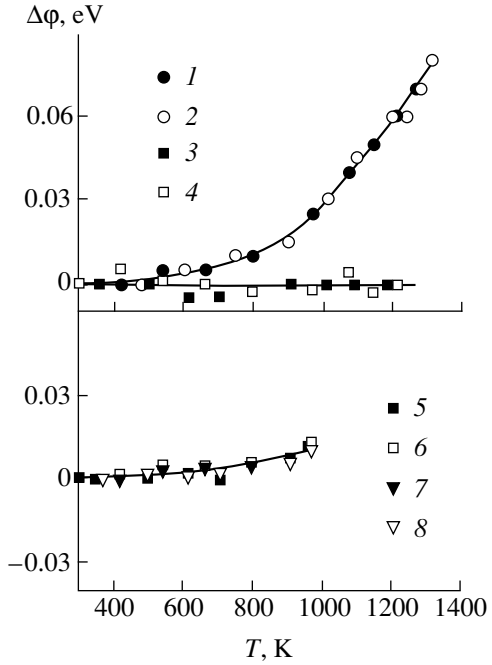

Fig. 1. Temperature variation of the Δφ value in thin-film Eu–W structures at various Eu adsorption coverages on W (see the text for explanation) θ = 0 (*1*, *2*), 0.10 (*3*, *4*), 0.25 (*5*, *6*), 0.34 (*7*, *8*). Black and open symbols represent the results of CPD measurements in the sample heating and cooling mode, respectively.

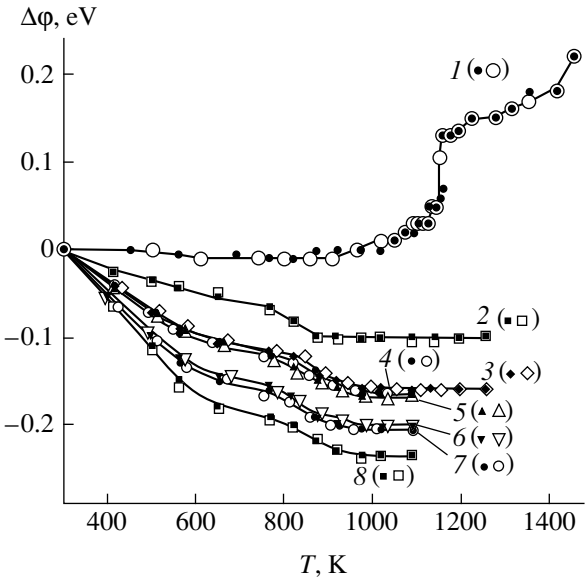

Fig. 2. Temperature variation of the Δφ value in thin-film Eu–Si(111) structures at various Eu adsorption coverages on Si (see the text for explanation) θ = 0 (*1*), 0.10 (*2*), 0.16 (*3*), 0.20 (*4*), 0.32 (*5*), 0.43 (*6*), 0.47 (*7*), 0.60 (*8*). Black and open symbols represent the results of CPD measurements in the sample heating and cooling mode, respectively.

the electron work function values at the current step temperature *T* and the at the room temperature (300 K). Then the temperature was gradually (also by steps) decreased and the Δφ values were again determined at certain *T* values in the cooling mode. Several heating–cooling cycles were performed for each particular adsorption system.

Results and discussion. Figures 1 and 2 show the experimental data obtained at various adsorption coverages, including θ = 0 (adsorbate-free substrates). A characteristic feature of these results is the qualitative change on the passage from θ = 0 to θ > 0. For this reason, we will separately consider the temperature variation of the electron work function in the two cases.

The adsorbate-free tungsten surface (θ = 0) is characterized by a monotonic increase in the electron work function with the temperature. At present, there is no commonly accepted explanation of this fact. More interesting results were obtained for silicon, in which the φ value slightly decreases when the sample is heated from 300 to 800 K. This behavior fully agrees with the data reported in [7]. However, the measurements in [7] were restricted to the 300–800 K interval, while we performed the experiments in a broad temperature range from 300 to 1460 K. It was found that heating the sample to $T > 1000$ K leads to a reversible significant increase in the electron work function, exhibiting a jumplike character. A considerable part of this increase occurs in the interval from 1050 to 1150 K. As is known (see, e.g., [8]), this temperature interval corresponds to a phase transition from 7×7 to a high-temperature 1×1 surface reconstruction. This coincidence is evidence that a change in the surface structure of silicon is accompanied by variation of the electron state of the surface Si atoms.

The results obtained for the two adsorption systems (θ > 0) also significantly differ. For the Eu–W system, the electron work function in the interval 300 K ≤ T ≤ 1210 K is either independent of the temperature or varies very slightly. This behavior contradicts theoretical conclusions derived in [9] from the study of the temperature dependence of the dipole moments of adsorbed atoms, according to which the dipole moments must increase with the temperature. Apparently, when the surface dipoles are oriented with their positive ends toward vacuum (as in the Eu–W system [10]), this trend would lead to a decrease in the electron work function with increasing temperature. The discrepancy between our experiment and the theory is probably related to a simplifying assumption made in the theoretical work cited, according to which a position of the valence level of an adatom is independent of the adsorption bond length.

For the Eu–Si(111) system, an increase in the temperature is accompanied by a significant reversible decrease in the electron work function. The magnitude of the drop in φ increases with the surface coverage, but the character of the $\Delta\varphi = f(T)$ curves is virtually the same for all θ. This indicates that the drop in φ for all coverages is caused by the same processes. In order to understand the nature of these processes, we must possess information concerning the structure and elemen-

tal composition of the adsorbed layers. Unfortunately, at present this information is very restricted. The structural measurements performed by LEED yield data only about the symmetry of the adsorbed layer geometry. To our knowledge, investigations using scanning tunneling microscopy were not performed for the Eu–Si(111) system.

We have attempted to partly fill the gap in experimental data using the AES and CPD measurements. The AES spectra showed that the peak of silicon significantly decreased upon the adsorption of europium at 300 K, which indicated that silicon atoms under these conditions are screened by the adsorbate. However heating the substrate to high temperatures (900–1000 K) led to a significant increase in intensity of the silicon signal (albeit not to a level characteristic of the clean substrate surface), while the europium signal intensity remained unchanged. This behavior shows that heating resulted in the formation of a monolayer film composed of Eu and Si atoms.

A similar conclusion was derived from the results of CPD measurements. It was found that deposition of Eu atoms on the silicon surface at 300 K leads to a considerable decrease in the electron work function: for $\theta = 0.5$, the drop in φ amounts to 1.6 eV. These data indicate that the adsorbed Eu atoms bear a positive charge and their adsorption bonds with the surface are characterized by a large dipole moment. However, the room-temperature φ value increased upon heating a substrate with the adsorbed Eu film to 900–1000 K. For $\theta = 0.5$, the φ value increased by 0.86 eV to reach 3.9 eV.

Such a large electron work function is not typical of surfaces covered by the films of electropositive adsorbates such as rare-earth elements. Nor can we explain the observed large φ value assuming the formation of a structure comprising the uppermost layer of Si atoms with a layer of rare-earth atoms beneath: the work function of such system would markedly exceed 3.9 eV. Indeed, Si atoms (as more electronegative than Eu atoms) in this system would be negatively charged and the metal atoms would be positive. This electric double layer would certainly provide for a much higher electron work function than that observed in our case. Analogous conclusions can be derived for the other surface coverages at which no silicide is formed ($\theta \le 0.6$).

A general conclusion that can be made based on the AES and CPD data is that heating leads to the mixing of Eu and Si atoms. At room temperature, this mixing results in the formation of a monoatomic surface layer composed of Eu and Si atoms. The effect of this heterogeneous layer on the electron work function may be temperature-dependent. This dependence is related to a temperature-induced variation in the amplitudes of oscillations in the directions perpendicular and parallel to the substrate surface. These oscillation components differently influence the work function. Let us consider this factor in more detail.

According to [9], the mean square amplitude of the oscillations in the direction normal to the surface at high temperatures ($T > \theta_D$, where θ_D is the Debye temperature) in the harmonic approximation can be expressed as

$$u_\perp^2 = \frac{3}{4}\frac{k_B T}{k}, \tag{1}$$

where k_B is the Boltzmann constant, $k = E/a^2$ is the force constant of the adatom–substrate bond, E is the energy necessary to remove an adatom from the surface to vacuum, and a is the adsorption bond length. The E value for adsorbed Eu atoms was determined previously [6], while the value for Si adatoms is unknown. However, this quantity must exceed the value for Eu, which follows from the fact that Si atoms are not evaporated from the surface at a temperature sufficient to desorb Eu atoms. The adsorption bond lengths for both Eu and Si atoms are equal because these adatoms occur in the same plane. Therefore, we may suggest that the amplitude $u_\perp^2$ for Si is smaller than that for Eu adatoms. The difference in the normal amplitudes, insignificant at low temperatures, will increase on heating.

Since the oscillating atoms mostly occur at the turn points [11], where their velocities are zero, the above difference in the normal amplitudes results in that the surface of the adsorbate–substrate system consists of two sublayers. The upper sublayer is composed of positively charged Eu atoms and the lower, of the negatively charged Si atoms. These sublayers form an electric double layer favoring a decrease in the electron work function. Apparently, this decrease will be more pronounced for higher coverage θ and greater separation l between the sublayers. Using Eq. (1), the l value can be approximately expressed as

$$\begin{aligned} l &= u_\perp(\mathrm{Eu}) - u_\perp(\mathrm{Si}) \\ &= \frac{(3k_B T)^{1/2}}{2}[k^{-1/2}(\mathrm{Eu}) - k^{-1/2}(\mathrm{Si})]. \end{aligned} \tag{2}$$

This formula indicates that the potential drop across the electric double layer (provided constant charges on the adatoms) must increase, and the electron work function accordingly must decrease, in proportion to $T^{1/2}$. Thus, the above considerations lead us to the conclusion that a growth in the amplitude of oscillations normal to the surface decreases the electron work function.

A different effect is produced by the oscillation component parallel to the substrate surface. Apparently, these oscillations produce disorientation of the Eu^+–Si^- dipoles forming the electric double layer and, hence, favor a decrease in the normal oscillation component determining the electron work function. However, at low temperatures (i.e., when Eu and Si atoms occur in the same plane), the amplitude $u_\parallel$ may be several times lower than $u_\perp$ because the former motions are limited by the presence of nearest neighbors in the

adlayer [12]. Therefore, a change in the work function at low temperatures is primarily determined by variations in the normal amplitude $u_\perp$. However, as the adsorbed film exhibits separation into two sublayers and the distances between nearest neighbors in each sublayer increase, the amplitude $u_\parallel$ in both sublayers grows more rapidly than does the normal component. With this growth, a decrease in the electron work function will be hindered by the increasing disorientation of dipoles. It is not excluded that, at a certain temperature, the φ value would cease to drop.

Conclusion. A comparison of the conclusions following from the above model considerations and the experimental results for the Eu–Si(111) system shows that the proposed model provides a qualitative explanation of the general trends in the effect of temperature on the electron work function at various surface coverages θ. In particular, the model suggests that the general shape of the $\Delta\varphi = f(T)$ curves must be the same, that the growth of θ must lead to an increase in the extent of φ variation with the temperature, and that the φ may cease to change at a sufficiently high temperature. As seen from the data presented in Fig. 2, all the conclusions qualitatively agree with the results of our experiments.

In order to provide for the quantitative agreement of theory and experiment, we have to know the exact relationships between the atomic oscillation amplitude $u_\parallel$ and the distance between nearest neighbors in the adlayer. At present, this information is practically not available. An attempt at the quantitative interpretation would probably also require taking into account anharmonicity of the adatom oscillations, especially at elevated temperatures. On the whole, the experimental data and model considerations presented above show that the investigation of the temperature dependence of the electron work function of adsorbed layers provides valuable information about the electronic and dynamic properties of these systems.

Acknowledgments. This work was performed within the framework of the State Program "Surface Atomic Structures" Supervised by the Ministry of Science and Technology of the Russian Federation (project no. 2.5.99).

REFERENCES

1. D. A. Gorodetskiĭ and Yu. P. Mel'nik, Izv. Akad. Nauk SSSR, Ser. Fiz. **35** (5), 1064 (1971).
2. H. M. Kramer and E. Bauer, Surf. Sci. **92** (1), 53 (1980).
3. J. Kolaczkiewicz and E. Bauer, Surf. Sci. **160** (1), 1 (1985).
4. O. L. Golubev, T. I. Sudakova, and V. N. Shrednik, Zh. Tekh. Fiz. **70** (12), 67 (2000) [Tech. Phys. **45**, 1575 (2000)].
5. E. L. Kontorovich, T. I. Sudakova, and V. N. Shrednik, Pis'ma Zh. Tekh. Fiz. **25** (10), 69 (1999) [Tech. Phys. Lett. **25**, 410 (1999)].
6. T. V. Krachino, M. V. Kuz'min, M. V. Loginov, and M. A. Mittsev, Fiz. Tverd. Tela (St. Petersburg) **42** (3), 553 (2000) [Phys. Solid State **42**, 566 (2000)].
7. R. Backmann, Phys. Kondens. Mater. **8**, 31 (1968).
8. W. Mönch, in *Springer-Verlag Series in Surface Science*, Vol. 22: *Semiconductor Surfaces and Interfaces* (Springer-Verlag, Berlin, 1993).
9. S. Yu. Davydov, Surf. Sci. **364**, 477 (1996).
10. M. V. Loginov and M. A. Mittsev, Fiz. Tverd. Tela (Leningrad) **22** (6), 1701 (1980) [Sov. Phys. Solid State **22**, 992 (1980)].
11. L. I. Schiff, *Quantum Mechanics* (McGraw-Hill, New York, 1968; Inostrannaya Literatura, Moscow, 1959).
12. D. Woodruff and T. Delihar, *Modern Techniques of Surface Science* (Cambridge Univ. Press, Cambridge, 1986; Mir, Moscow, 1989).

Translated by P. Pozdeev